Annual Report 2008

Chair of Experimental Physics
Prof. Dr. Winfried Petry

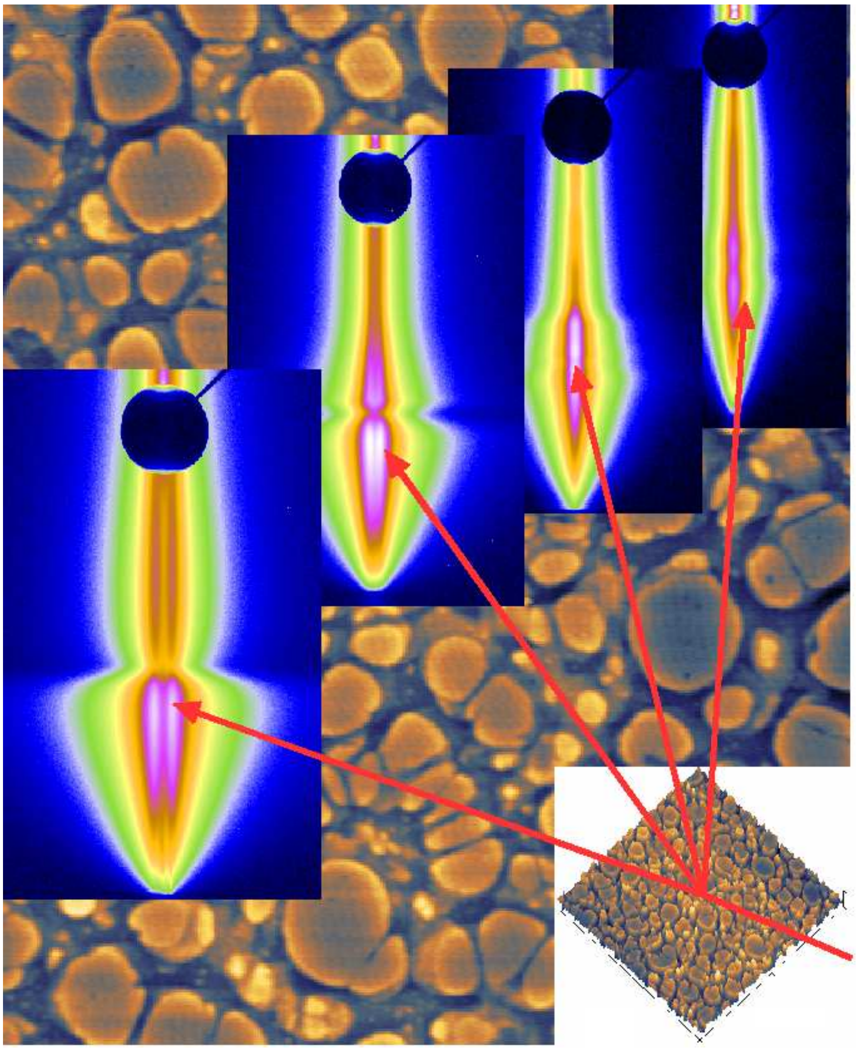

Physik-Department E13

Technische Universität München

Prof. Dr. Winfried Petry
Chair of experimental physics IV
Physik-Department E13

Deputy chairman for Prof. Petry:
Prof. Dr. Peter Müller-Buschbaum

Physik-Department E13
Technische Universität München
James-Franck-Straße 1
85747 Garching

Sekretariat: Petra Douglas

Tel.: 089 289 12452
Fax: 089 289 12473

Email: peter.mueller-buschbaum@ph.tum.de
Petra.Douglas@ph.tum.de
http://www.e13.ph.tum.de

Editor: Dr. Johannes Wiedersich

Title picture:
2D GIUSAXS scattering patterns of different polymer blends based on MEH-PPV and PVK. The polymers are dissolved in toluene at different concentrations and the blended solutions are spincoated on silicon substrates. They are of great interest for organic electronic applications like light emitting diodes (OLED) or solar cells. The underlying topography atomic force microscope (AFM) image shows a phase separation of the polymers on the microscale. It is shown that the typical structure size of the film is very well tuneable via the polymer concentration in their solution. The polymer concentration for the 2D detector images increases from the lower left corner to the upper right corner. For the sample with the lowest concentration a well defined split of the Yoneda peak can be detected. For higher concentrations it vanishes. The shape of the scattering image with its attracting *corset* right above the Yoneda peak is a result of the correlated roughness of the thin films.

Preface

It is a great pleasure to present the 2008 annual report of the chair E13 at the Physics Department of TU München. Our research activities cover a broad range from soft matter physics to developments in methods and instrumentation. We examine the physical fundamentals of material properties using scattering methods (neutrons-, x-ray and light scattering). The general goal of our research is to explain the functional characteristics of soft condensed matter from the knowledge of the microscopic dynamics and structure.

In 2008, the chair activities covered the areas of water-based polymer systems, thin polymer films, polymer films for application in photovoltaics, polymer-hybrid systems, biopolymers, dynamics in soft matter and methodological and instrumental developments. The refurbishment of the E13 light scattering laboratory focussing on Brillouin spectroscopy was successfully finished. As a consequence, powerful experimental techniques were available in the E13 laboratories and complemented the lively activities at large scale facilities, comprising synchrotron radiation and neutron scattering experiments. Moreover, the developments in methods and instrumentation extended to the large scale facilities: Both, the instrument TOF-TOF at the research reactor FRM-II was operated and upgraded and micro-beam grazing incidence small angle x-ray scattering was installed and developed at the MINAXS instrument at PETRA III in Hamburg.

Extending the research activities in the field of photovoltaics was accompanied by the development of new testing devices of photoactive thin films, which can be used at large scale facilities. The upgrade of the chemistry laboratory for the special handing of photoactive polymers supported these activities. As a consequence, polymer-polymer and polymer-inorganic material systems were in the scientific focus.

In 2008, the chair E13 comprised 13 fellows, 18 PhD students, 6 diploma students, 2 master students, 8 student assistants and 9 administrative and technical staff members. We regret the retirement of Dr. Uwe van Bürck and PD Dr. Wolfgang Doster and wish them all the best for the future. A new head of the corresponding biopolymer laboratory will be searched in 2009.

In general, all E13 members were very active at conferences and workshops, participating with talks and posters. The workshop on 'Biomolecular Dynamics and Protein-Water Interactions' in Feldafing near Munich was organized by PD Dr. Doster and successfully brought many well known scientist in this field together. Regarding teaching activities of E13, we covered a large part of the export lectures: physics for students of mechanical engineering (Müller-Buschbaum), for teachers at colleges BT / ET / MT / EI (Papadakis) and for teachers at colleges AW / EH / PF (Doster). Moreover Prof. Schirmacher gave the lecture Theoretische Physik 3 (Quantenmechanik).

This annual report comprises a selection of the different research topics and projects carried out in the individual groups of E13. It highlights the engaged and successful research activities and collaborations with other groups and large scale facilities. I wish all E13 members a fruitful continuation and a successful year 2009.

Peter Müller-Buschbaum April 2009

Contents

1 Water-based polymer systems

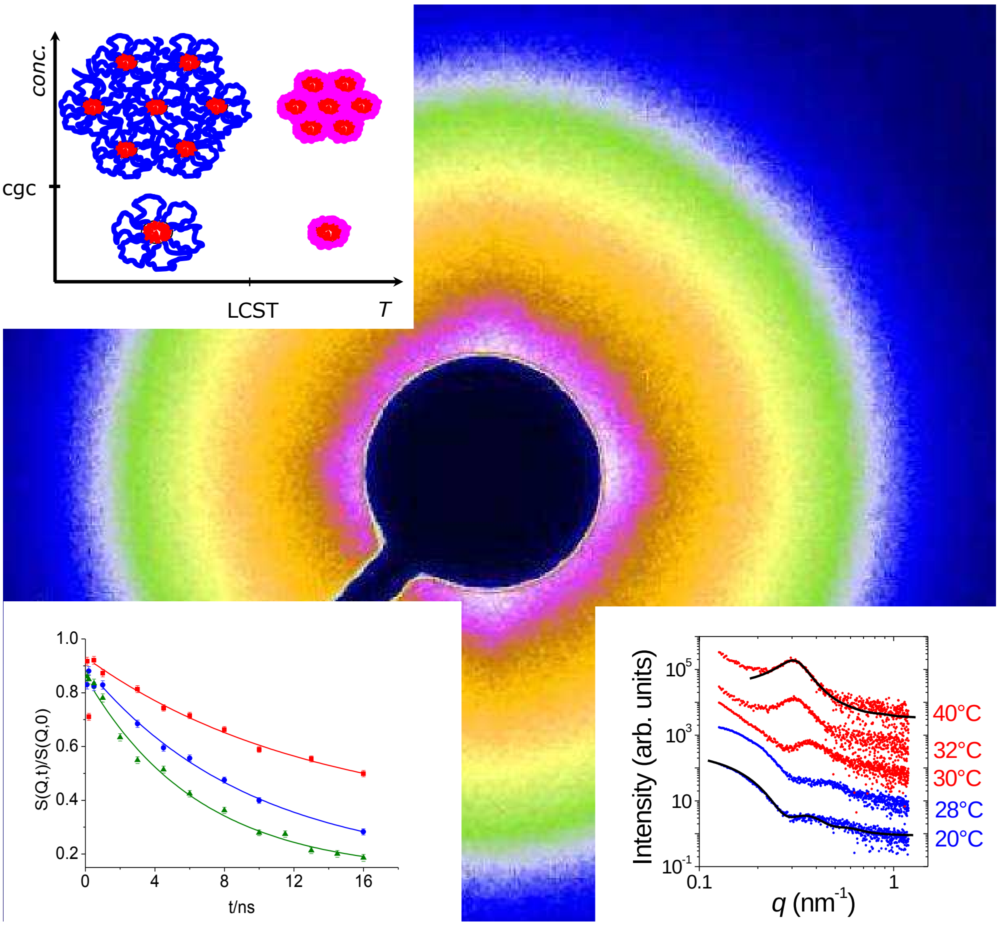

1.1 Aggregation behavior of thermo-responsive poly(2-oxazoline)s

S. Salzinger, S. Huber[1], R. Jordan[1], C.M. Papadakis

[1] Department Chemie, TU München

Thermo-responsive polymers change their chain conformation in water strongly upon a small change of temperature: Below the lower critical solution temperature (LCST), they are swollen and water-soluble, whereas above, they are collapsed and hence water-insoluble. Therefore, they are of interest for polymeric drug delivery [1]. Poly(2-oxazoline)s are of special interest since they are non-toxic. Moreover, they constitute a very flexible system due to the possibility of attaching different side groups to the backbone, which determines, for instance, their water solubility or which may be functionalized [2].

We have focused on characterizing the aggregation behavior at the LCST temperature. Poly(n-propyl-2-oxazoline)s (PnPrOx) as well as (more hydrophilic) poly(iso-propyl-2-oxazoline)s (PiPrOx) homopolymers having different degrees of polymerization, a diblock copolymer, P(nPrOx-*b*-iPrOx), and gradient copolymers from iPrOx and (very hydrophobic) 2-n-nonyl-2-oxazoline (NonOx) were studied. Using turbidimetry, the LCSTs were determined as a function of concentration. The hydrodynamic radii of the unimers, i.e. single dissolved polymers, and of the aggregates formed upon collapse were characterized using temperature-resolved fluorescence correlation spectroscopy (FCS). As tracers, we used the identical polymers which were fluorescence-labeled at the terminus with tetramethylrhodaminisothiocyanate (TRITC). They were added in small amounts to aqueous solutions of the non-labeled polymers.

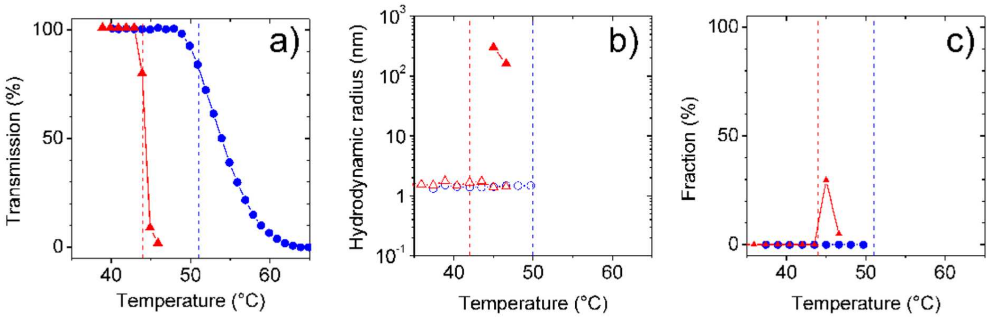

Figure 1.1:
Results from aqueous solutions of PiPrOx$_{50}$ at 0.5 mg/ml (circles) and 5 mg/ml (triangles). (a) Light transmission from turbidimetry and (b,c) results from FCS: (b) hydrodynamic radii of unimers (open symbols) and aggregates (closed symbols) and (c) fraction of the polymers present as aggregates.

The light transmission of the homopolymer solutions decreases strongly at the LCST (fig. 1.1a) and drops to zero. The lower the concentration, the higher is the LCST and the broader is the decay. FCS shows that the unimer size is of the order of 1-2 nm (fig. 1.1b). At the LCST, additional aggregates of hydrodynamic radius above 100 nm form for sufficiently high concentration (5 mg/ml). They are at the origin of the decrease of the light transmission and become more significant as temperature is increased (fig. 1.1c). in FCS, temperatures above 50°C were not accessible.

For the gradient copolymer, the light transmission also decreases at the LCST (fig. 1.2a), which is shifted to far higher temperature, i.e. the 2 NonOx groups have a strong effect on the water solubility. The aggregation behavior displays two steps: First, smaller aggregates (hydrodynamic radius $<$ 30 nm) form, which grow to above 100 nm and become more frequent only at

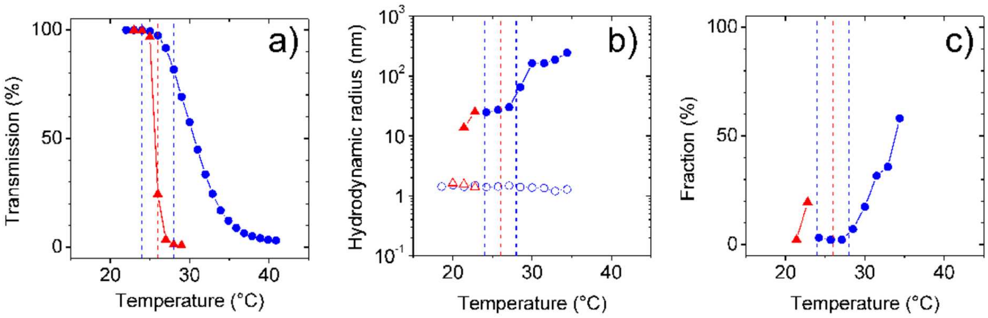

Figure 1.2:
Results from aqueous solutions of P(iPrOx$_{48}$-*g*-NonOx$_2$) at 0.5 mg/ml (circles) and 5 mg/ml (triangles). (a) Light transmission from turbidimetry and (b,c) results from FCS: (b) hydrodynamic radii of unimers (open symbols) and aggregates (closed symbols) and (c) fraction of the polymers present as aggregates.

higher temperatures (fig. 1.2b,c). Only when these large aggregates form, the light transmission drops significantly.

In experiments on several polymers, we found that the LCST depends strongly on the nature of the side group: For the homopolymers, the LCSTs of PnPrOx homopolymers are consistently lower than those of PiPrOx homopolymers. As expected, the LCST decreases with increasing degree of polymerization and with increasing concentration. These results confirm that aggregation of the homopolymers at the LCST is at the origin of the turbidity. For the gradient copolymers P(iPrOx-*g*-NonOx), the LCSTs are significantly lower than for PiPrOx homopolymers of the same overall lengths, which may be ascribed to the hydrophobic NonOx groups. However, the dependence on the NonOx content is only weak. The diblock copolymer has an LCST similar to the one of the PnPrOx, i.e. its properties depend mainly on the more hydrophobic block. In all cases, the aggregate formation is reversible, i.e. the aggregates dissolve again upon cooling below the collapse temperature.

We conclude that the LCST in the POx system as well as its sharpness can be controlled by the nature of the sidegroup, the polymer architecture and the concentration in aqueous solution. The formation of aggregates is at the origin of the drop in light transmission used for determining the LCST. Complex aggregation behavior is witnessed in gradient copolymers of a thermoresponsive and a hydrophobic monomer.

The project is funded by DFG (Pa771/6).

[1] S. Chen, J. Singh, Int. J. Pharm. **352**, 58 (2008).

[2] S. Huber, R. Jordan, Colloid Polym. Sci. **286**, 395 (2008). M.T. Zarka et al., Chemistry - A European Journal **9**, 3228 (2003). C. Taubmann, R. Jordan et al., Macromol. Biosci. **5**, 603 (2005). T.B. Bonné, K. Lüdtke, R. Jordan, P. Štěpánek, C.M. Papadakis, Colloid Polym, Sci. **282**, 833 (2004).

1.2 Spinodal decomposition of thermo-responsive hydrogel PNIPAM

A. Meier-Koll, A. Golosova, P. Busch[1], V. Pipich[1], J. Wiedersich, C.M. Papadakis, P. Müller-Buschbaum

[1] JCNS, Garching, Germany

Hydrogels are considered as three dimensional polymer networks which incorporate water molecules into the network. Typical hydrogels are chemically or physically cross-linked systems to obtain the gel state and ensure mechanical stability of the system. Depending on the water content and external parameters such as pressure or temperature the structure of the polymer network is changed. In addition, thermo-responsive hydrogels show a volume phase transition at a lower critical solution temperature (LCST). Below LCST the polymer is soaked up with water and therefore is swollen. At LCST the polymer becomes hydrophobic and releases bound water. Above LCST it collapses and shrinks to significantly smaller volumes. Poly(N-isopropylacrylamid) (PNIPAM) is one of the most prominent thermo-responsive hydrogels with a LCST of about 33° C [1].

In contrast to such network systems, the pure thermo-responsive polymer PNIPAM receives less attention. Contrary to the behavior of most compounds in aqueous solutions, thermally responsive polymers become less soluble (more hydrophobic) in water at elevated temperatures.

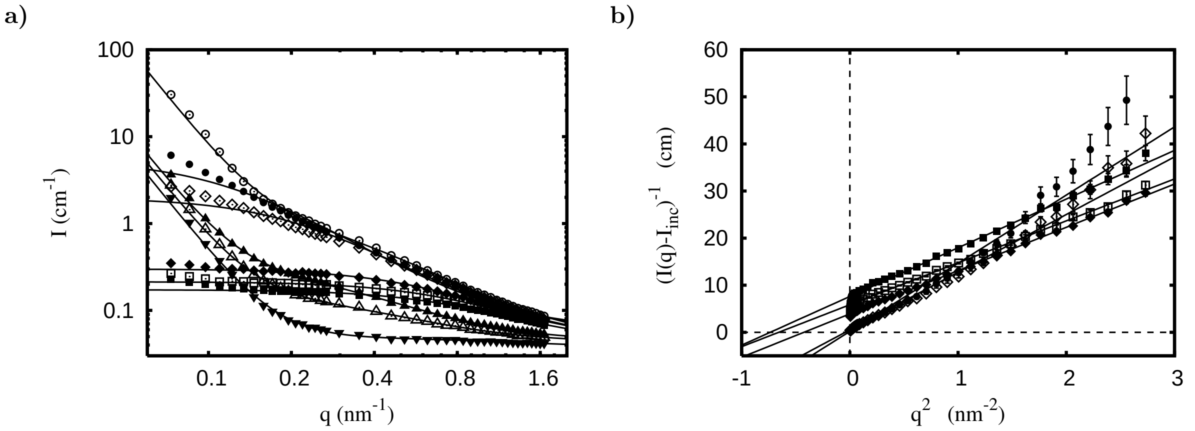

Figure 1.3:
a) SANS curves in double logarithmic presentation for different temperatures: 15.6°C (filled square), 20.3°C (open square), 25.0°C (filled diamond) 32.5°C (open diamond) 32.9°C (filled circle) 33.4°C (open circle) 35.3°C (filled triangle up) 36.2°C (open triangle up) 43.7°C (filled triangle down). Continuous curves are fits to the data. b) Orstein-Zernicke plot of the data for temperatures below and near the phase transition temperature: 15.6°C (filled square), 20.3°C (open square), 25.0°C (filled diamond) 32.5°C (open diamond) 32.9°C (filled circle) 33.4°C (open circle). For clarity only each second point is shown.

In the present investigation we focus on the temperature resolved structure formation in PNIPAM solutions. The aqueous solution is studied below the phase transition and the temporal evolution of the structures is probed after deep temperature quenches into the two phase region of the homopolymeric hydrogel [2]. The work is based on small angle neutron scattering (SANS) experiments. The hydrogel was prepared with 13 wt% of commercial PNIPAM in $D_2$0. Samples were kept for several days prior the experiment at room temperature in order to allow for equilibration. SANS measurements were performed at the KWS2 instrument of the Julich Center of Neutron Science at FRM II (Garching). The instrument was operated with neutrons of 7 Å wavelength and detector-sample-distances of 2 and 8 m to cover the scattering vector range from 0.7 to 1.7 nm^{-1}. The data were recorded with a Li6-glass detector (area of 128×128 pixels

and 60×60 cm^2 in size). Data were corrected for background counts, container contribution, spherical artifacts, normalized to PMMA standard and finally radial averaged.
Fig.1.3a shows representative SANS curves for various temperatures below and above LCST. Far below the phase transition (15.6 to 25.0 °C) the shape of the scattering curves is characterized by density fluctuations of polymer strands. In this temperature regime the intensity increases slightly with increasing temperature. More details reveal the Orstein-Zernicke (OZ) plot in fig.1.3b. With increasing temperature the x-axis offset of the line fits decreases indicating a critical phenomenon while approaching LCST. From Orstein-Zernicke fits the spinodal temperature $T_S = 33.1 \pm 0.1°C$ is obtained. Near the phase transition point (32.5 to 33.5 °C) the intensity increases and is finally dominated by a strong forward scattering indicating the formation of interfaces between large and unresolved domains. The consecutive decrease of the forward scattering is attributed to a kinetic coarsening of the domains (35.3 to 43.7 °C).

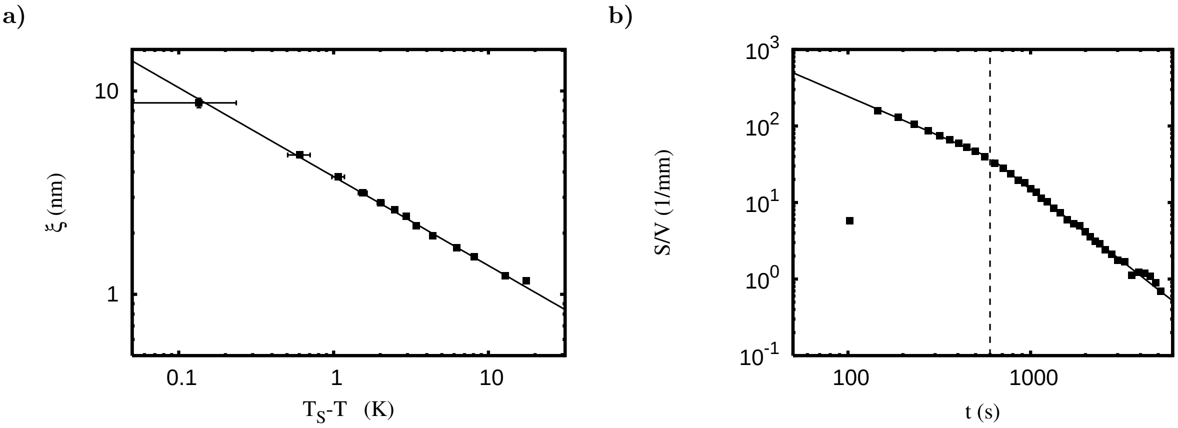

Figure 1.4:
a) OZ correlation length ξ versus temperature difference between spinodal temperature T_S and sample temperature T. b) Temporal evolution of the specific surface S/V after a temperature quench from $20°C$ to $50°C$. For clarity, the dashed line marks the transition from an intermediate to the late stage regime.

The temperature dependence of the OZ correlation length ξ below the spinodal temperature T_S shows a power law behavior with an exponent of 0.44 (see fig.1.4a). After crossing the spinodal point the system forms interfaces between the domains which coarsen in the consecutive time [2].
The time dependence of the structural evolution is probed with temperature jumps. As an example, fig. 1.4b shows the evolution of the specific area per volume after a temperature quench form $20°C$ to $50°C$. So the system is quenched deeply into the two-phase regime. With exception of the first data point (100 sec), which belongs two the early stage of the decomposition, one observes two stages of coarsening which can be described by power laws of different exponents. The intermediate stage (until 600 sec) is characterized by an exponent of 1.03 whereas the late stage is characterized by an exponent of 1.87 [2]. Thus two consecutive processes are acting during decomposition.

[1] H.G. Schild, Prog. Polym. Sci. **17** 163 (1992)

[2] A. Meier-Koll, A. Golosova, P. Busch[1], V. Pipich[1], J. Wiedersich, C.M. Papadakis, P. Müller-Buschbaum; to be published

1.3 Mechanical properties the thermo-responsive polymer PNIPAM studied with Brillouin light scattering

A. Meier-Koll, J. Wiedersich, P. Müller-Buschbaum

Poly(N-isopropylacrylamid) (PNIPAM) is a thermo-responsive polymer which has a volume phase transition at the lower critical solution temperature (LCST) near 33 °C. Below LCST the polymer incorporates water molecules into its network and releases them when the temperature increases above LCST. At temperatures higher than LCST the polymer network is collapsed and shrunken to a smaller volume as compared to the swollen state. Due to this behavior thermo-responsive polymers cross-linked into hydrogels attract interest as functional materials in actuators and drug delivery systems [1, 2]. However, beyond this scope the study of the mechanical properties are still limited [3].

In the present investigation we study the viscoelastic behavior of aqueous PNIPAM solutions and gels at different polymer concentrations and temperatures below and above LCST with means of Brillouin light scattering technique. Samples were prepared by solving the appropriate amount of polymer with deionized water in quartz glass vials. Directly after preparation the vials were sealed. At least one half day prior to the experiment, the samples were transferred into a thermostatically controlled environment which was set to the initial temperature of the light scattering experiment. Brillouin light scattering was performed with a six-pass tandem Fabry-Perot interferometer (Sandercock). As light source we used a neodym:vanadate laser which was operating at a wavelength of 532.2 nm and delivered 50 mW at sample position. The polarized component of the scattered light was observed in back-scattering geometry. From the Brillouin spectra frequency shifts f and linewidths Γ (HWHM) are extracted by fitting sums of Lorentzians.

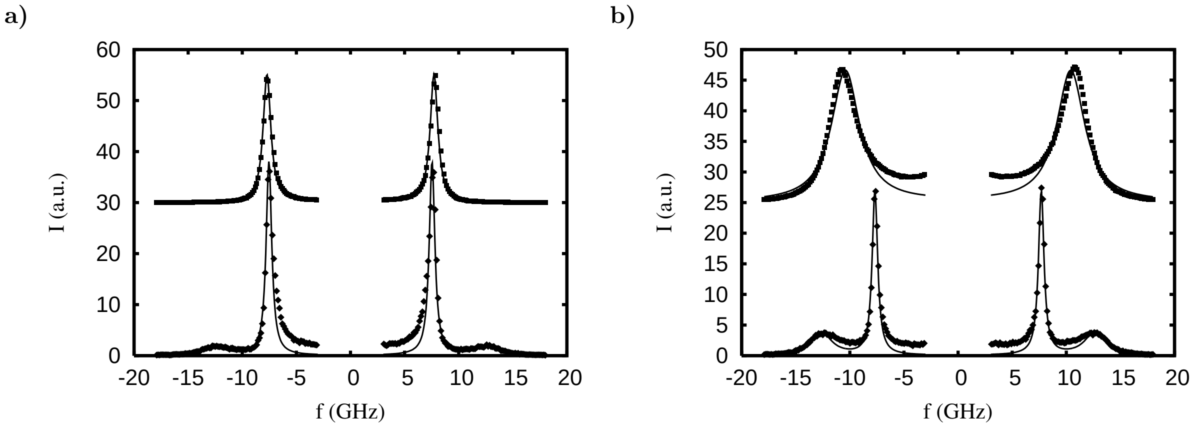

Figure 1.5:
Brillouin spectra for PNIPAM solutions below 20°C (top) and above LCST 38°C (bottom). For clarity only every fifth data point is shown and the elastic line is cut-out. Solid lines are Lorentzians fits to the data. Comparison between the a) low concentrated polymer solution (10 wt% PNIPAM in water) and the b) high concentrated gel (50 wt% PNIPAM in water).

Fig.1.5 shows examples of Brillouin spectra for low and high concentration of the polymer solutions above and below the phase transition temperature. The low concentration pictures the dilute system (PNIPAM solution) and the high concentration the gel phase. In case of dilute polymer solutions the Brillouin spectra exhibit one strong, sharp line near 8 GHz for temperatures below and above LCST. In addition, above LCST a small broad hump near 12 GHz appears in the Brillouin spectra. This situation changes dramatically in case of high concentrations of the polymer solutions. Below LCST the spectra show a broad Brillouin line near 11 GHz, but above LCST this line is shifted towards a smaller frequency. Its position and linewidth are now similar to samples with low concentrations. Equal to the dilute system, in the Brillouin spectra of the gel samples a broad line appears above LCST. Due to the higher polymer concentration for gel samples the intensity is slightly higher than for dilute solutions.

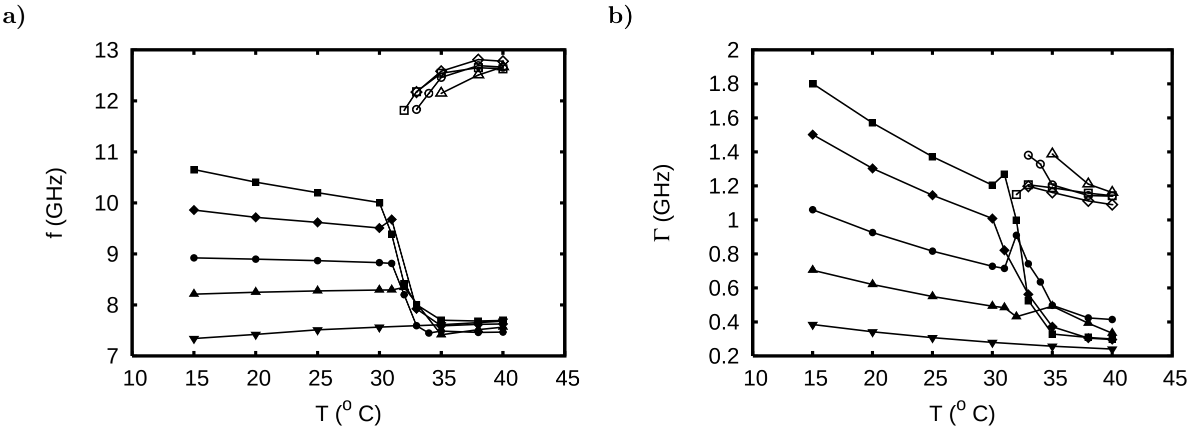

Figure 1.6:
a) Brillouin line shifts of different PNIPAM concentrations in water depending on temperature. Mass fractions of PNIPAM are as follows: 50 wt% (squares), 42 wt% (diamonds), 30 wt% (circles), 15 wt% (up turned triangles), pure water (down turned triangles). Filled symbols represent Brillouin lines of the solution (below LCST) and the water rich phase (above LCST). Open symbols represent Brillouin lines from the polymer rich phase. b) Brillouin linewidths of different PNIPAM concentrations in water depending on temperature. Symbols are the same as in a). Lines are guide for the eyes.

The extracted Brillouin shifts are shown in fig. 1.6a. The behavior below and above LCST is marked different. Below LCST and at low polymer concentrations (below 30 wt% PNIPAM) the frequency shifts increase with increasing temperature. This characteristic is similar to the behavior of pure water without added polymer. In contrary, at higher concentrations the frequency shifts decrease with increasing temperature below LCST. Such a type of behavior is also found in other systems such as glasses. At LCST the frequency diagram changes drastically. It bifurcates in two branches: a water rich phase near 7.5 GHz and a polymer rich phase between 12 and 13 GHz. Both branches are independent of the total polymer concentration. This observation indicates that domains larger than the laser wavelength are formed and that the elastic properties in these domains are always identical irrespective of the initial concentration. Thus both demixed phases are mechanically identical and of the same composition independent of the initial concentration. As a consequence, the initial concentration can only alter the size of the domains.

Fig. 1.6b shows the temperature dependence of the probed linewidths. Below LCST the linewidths decrease linearly with increasing temperature independent of polymer concentration. Again the linewidths bifurcate at the phase transition temperature in two branches. Small linewidths originate form water rich domains whereas polymer rich domains show broad linewidths. The sudden increase of the linewidths at LCST are artifacts of the Brillouin measurement due to a turbidity of the samples.

[1] S. Shinohara, N. Tajima, K. Yanagisawa; J. Intell. Matter. **25**, 481, (1987)

[2] K.V.R Rao, K.P. Devi; Int. J. Pharm. **48**, 1 ,(1988)

[3] S. Hirotsu ea.; J. Phys. Soc. Jap.,**64(4)**, 2298,(1995)

1.4 Structure and dynamics of thermo-responsive polymeric hydrogels

J. Adelsberger, A. Jain, A. Kulkarni, A. Bivigou Koumba[1], A. Laschewsky[1], P. Müller-Buschbaum, C. M. Papadakis

[1] Institut für Chemie, Universität Potsdam

Thermo-sensitive polymers have received increasing attention as they respond in a controlled and reversible way with a strong volume change to a small change of temperature across the lower critical solution temperature (LCST). They are of great interest for medical applications as well as for controllable nanoporous membranes [1]. A widely used LCST polymer is poly(N-isopropyl acrylamide) (PNIPAM) which has an LCST at 32 °C.

We investigate triblock copolymers which have two hydrophobic polystyrene (PS) endblocks and one hydrophilic PNIPAM middleblock. In aqueous solution, they form flower-like core-shell micelles or, above the critical gel concentration micellar hydrogels. If they are heated up to the lower critical solution temperature (LCST) the PNIPAM block becomes hydrophobic and releases water from the micellar shell, which collapses.

In order to determine the structure of the polymeric hydrogels, we use small-angle neutron scattering (SANS) and dynamic light scattering (DLS) [2,3]. For the investigation of the PNIPAM chain dynamics in the swollen and collapsed state, the neutron spin echo spectroscopy (NSE) has proved as a powerful method [4].

For SANS and NSE experiments, solutions of the polymer with 387 PNIPAM monomers and 10 PS monomers at each end ($M = 46000$ g/mol) were prepared in D_2O. Only the micellar shells were visible in this experiment, because D_2O had the same scattering length density as the deuterated PS blocks.

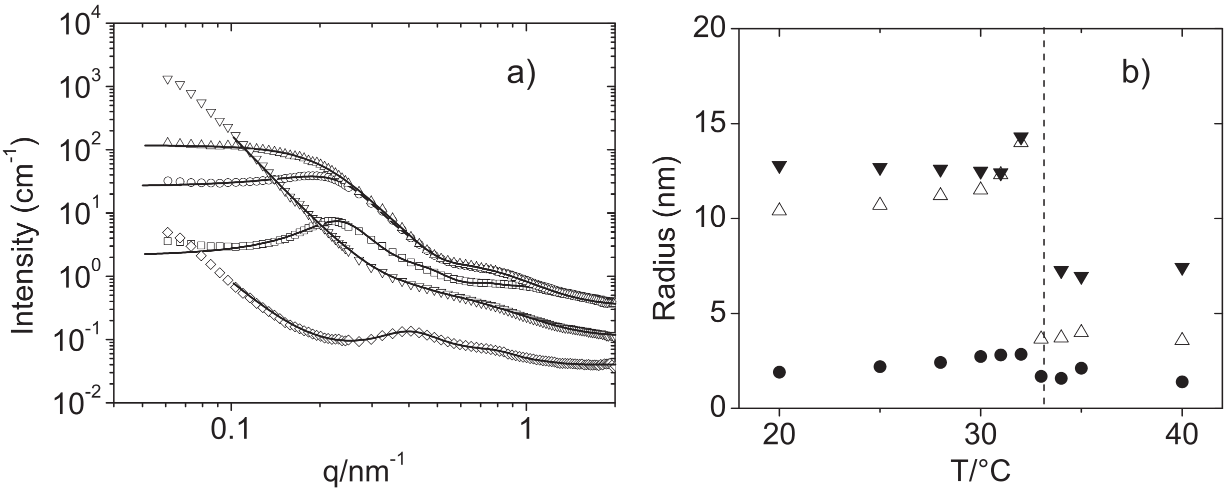

Figure 1.7:
Temperature resolved SANS curves from a solution with 170 mg/ml at 20 °C (squares) , 31 °C (circles), 32 °C (triangles up), 33 °C (triangles down), 40 °C (diamonds) together with the fitting curves. (b) Resulting core radius (filled diamonds), shell radius (open triangles) and effective radius (filled triangles) above and below LCST (dashed line).

Using SANS, we could characterize the micelles in detail (figure 1.7 a). As expected, the radius of the PS core does not change at the LCST, whereas the micellar shell collapses strongly at the LCST (see figure 1.7 b). The correlation peak is shifted to higher q-values above the LCST, as the micelles become smaller and pack closely together due to their increased hydrophobicity. Moreover, the collapsed micelles form large clusters, as evident from strong forward scattering which follows approximately a Porod law, thus the clusters are compact objects (see figure 1.7 a).

The temperature-resolved DLS experiments were performed at lower concentration (0.1 mg/ml) with an non-deuterated copolymer of similar composition and molar mass ($M = 50000$ g/mol). A standard setup for DLS was used with a laser wavelength λ= 532 nm and a detection angle of 90 °C. As the sample is heated from 25 to 31 °C, the hydrodynamic radius R_h decreases from 27 nm to 23 nm in good agreement with previous DLS measurements [2]. The collapse of micellar shells cannot be observed at the LCST, but aggregates with R_h=26 nm form. Above 36 °C even bigger clusters (R_h=68 nm) are formed. Upon further heating, the radii of both types of clusters decrease again (see figure 1.8 a).

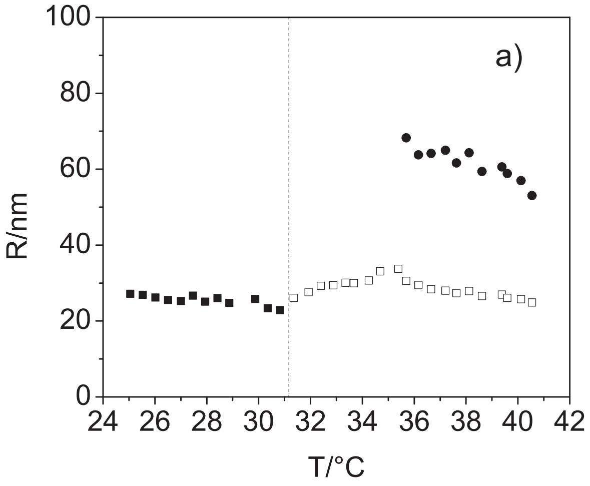

Figure 1.8:
a) DLS results of a solution of 0.1 mg/ml; filled squares indicate swollen micelles below the LCST (dashed line), open squares small aggregates of collapsed micelles and filled circles big aggregates of collapsed micelles above the LCST (dashed line) b) Temperature dependence of the averaged diffusion coefficient $\overline{D}$

Using NSE, we measured the intermediate scattering function $S(Q,t)$ of an 170 mg/ml solution of the deuterated triblock copolymer in D_2O.

It decays exponentionally like $S(Q,t) = S(Q,0) \cdot exp[-\Gamma t]$ with $\Gamma = \overline{D} q^2$ where $\overline{D}$ is the diffusion coefficient averaged over all modes of PNIPAM chain motion. The decay constant Γ, which results from a fit to the intermediate scattering function depends on q^2. $\overline{D}$ does not depend on temperature between 25 °C and 32.5 °C (see figure 1.8 b), i. e. the LCST has not been reached yet. This may be due to the limited Fourier times (up to 30 ns).

The combination of SANS, DLS and NSE thus leads to a detailed understanding of the collapse of the micelles, the behavior of the micellar gel and the dynamics of the thermo-responsive block.

The project is funded by DFG within the priority program "Intelligent hydrogels".

[1] A. Nykänen, M. Nuopponen, A. Laukkanen, S.-P. Hirvonen, M. Rytelä, O. Turunen, H. Tenhu, R. Mezzenga, O. Ikkala, J. Ruokolainen, Macromolecules **40**, 5827 (2007)

[2] K. Troll, A. Kulkarni, W. Wang, C. Darko, A. M. Bivigou Koumba, A. Laschewsky, P. Müller-Buschbaum, C. M. Papadakis, Colloid Polymer Science **286**, 1079 (2008)

[3] A. Jain, A. Kulkarni, A. M. Bivigou Loumba, W. Wang, P. Busch, A. Laschewsky, P. Müller-Buschbaum, C. M. Papadakis, Macromolecular Symposia, submitted Aug. 2008

[4] T. Hellweg, K. Kratz, S. Pouget, W. Eimer, Colloids and Surfaces A **202**, 223 (2002)

1.5 Water storage in hydrogel thin films maintaining the total film thickness as probed with in situ neutron reflectivity

W. Wang, E. Metwalli, J. Perlich, K. Troll, C. M. Papadakis, R. Cubitt[1], P. Müller-Buschbaum

[1] ILL, Grenoble, France

In the last three decades, intelligent hydrogels, which can change physical or chemical properties in response to environmental stimuli, like temperature, pH, light, chemical stimuli, and others, have attracted increased interest. Most of these responding systems are based on changes of the polymer chain conformation, which can cause problems in applications related to the swelling induced strain. Within the present investigation we focus on a polymer material in thin film geometry which allows for water incorporation and at the same time can keep the film volume fixed. Poly(*N*-isopropylacrylamide)(PNIPAM), one of the well-explored intelligent hydrogels [1-2], has been chosen as our candidate for water incorporation because it has a high affinity to water below its lower critical solution temperature (LCST) of approximately 32 ^{o}C. Thus it works well for water storage at room temperature. In the present investigation focused on water storage thin film materials, we select the model system of polystyrene-*block*-poly(*N*-isopropylacrylamide), denoted P(S-*b*-NIPAM) with a PNIPAM volume fraction of 27.6 % because a PNIPAM volume fraction of 30 % was reported to be the critical value for a "swelling" and "nonswelling" behavior in solutions. Thin films are prepared on silicon substrates which are precleaned with a base cleaning protocol. We demonstrate the water storage capacity when in contact with saturated water vapor. The investigation is based on in situ neutron reflectivity experiments in combination with the usage of deuterated water (D_2O) vapor to generate contrast with the copolymer film. Static measurements of the initially dry films and kinetics of the water storage were measured.

The initial dry P(S-*b*-NIPAM) films with a thickness of 47.4± 0.1 nm were prepared by spin-coating from a 1,4-dioxane solution at room temperature on precleaned Si wafer. The neutron scattering experiments were carried out at the D17 reflectometer of ILL, Grenoble, in time-of-flight (TOF) mode. The dry P(S-*b*-NIPAM) film was mounted in a special vapor chamber in air, thermostated to 23 ^{o}C and investigated. To start the storage D_2O was filled in the reservoir of the vapor chamber and thus the evacuated vapor chamber was saturated with a D_2O vapor atmosphere. The addition of D_2O marks the starting point of the kinetic water-absorbing investigation (time=0).

The density profile along the surface normal of the dry glassy hydrogel films is probed with neutron reflectivity. A bilayer profile is present. The bottom layer (d1) in direct contact with the substrate, has a thickness of only 1.9 nm and consists of pure PNIPAM. In contrast, the top layer (d2) has a thickness of 45.5 nm, and consists of the diblock copolymer P(S-*b*-NIPAM). Enrichment of NIPAM segments at the substrate interface is expected, because the applied base surface treatment results in a hydrophilic oxide. This hydrophilic oxide has a very strong attraction to the NIPAM segments.

In the kinetic experiment the dry glassy hydrogel film is exposed to water vapor and in situ neutron reflectivity measurements monitor the changes of the film due to storage of water. In figure 1.9(a), a series of selected 2-D detector patterns is presented. The boxes in figure 1.9(a)(I) mark selected integrated regions in the intensity: the specular reflectivity region (M) and the off-specular reflectivity regions (Yoneda peak of deuterated material Y1 and of protonated material Y2). Figure 1.9(b) shows the time evolution of specular reflectivity (M), and off-specular reflectivities (Y1 and Y2) for water storage for a total storage time up to 1.5×10^4 s. Due to the incorporation of D_2O during exposure to water vapor, the SLD of the protonated film increases. As a consequence, the reflected intensity increases and the position of the total reflecting edge

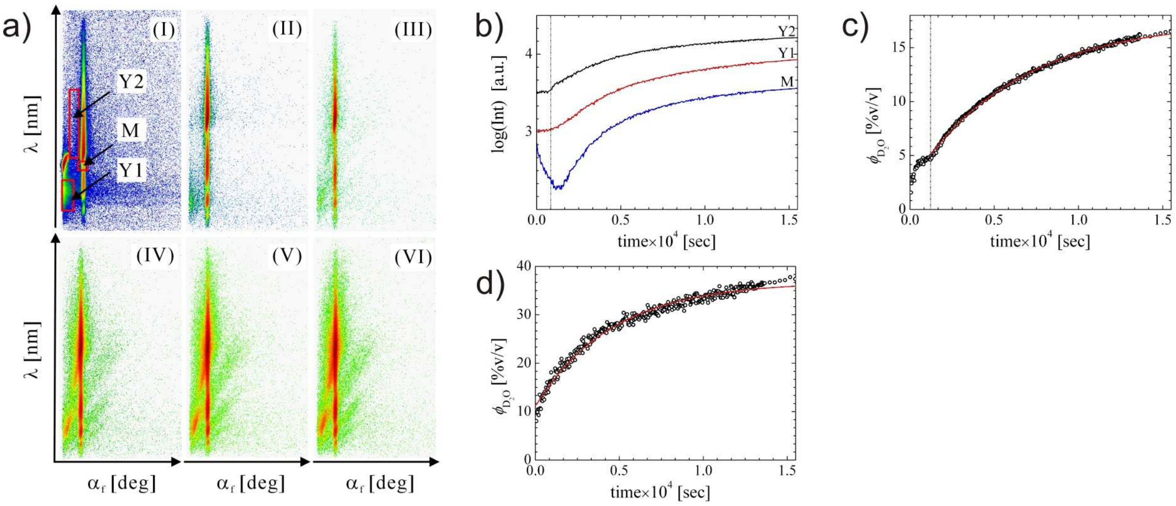

Figure 1.9:
(a) Measured 2-D detector pattern of scattered intensities displayed as a function of wavelength λ and exit angle α_f:(I) statics investigation of the film before water storage (counting time 1 h) (II-VI) kinetics investigation of the film during water storage at 30, 3000, 6000, 9000, and 12000 s after the sample was exposed to saturated D_2O vapor (counting time 30 s). (b) Integrated areas Y1, Y2, and M as marked with the boxes in (a) (I) shown on a logarithmic intensity axis as a function of time. The curves are shifted along the y-axis for presentation. (c) Water storage as probed for the top layer consisting of the copolymer and (d) bottom layer of pure PNIPAM due to interaction with the substrate. The experimental data (circles) are shown together with a model describing water diffusion. The dashed line separates stage I and II.

shifts toward smaller λ value in figure 1.9(a)(II). Moreover, the off-specular scattered intensities increase with exposure time due to the build-up of a lateral structure inside the glassy hydrogel film because D_2O selectively diffuses into parts of the polymer film (see figure 1.9(a)(IV-VI)). After the water vapor is extracted, both the specular and the off-specular scattered intensities decrease immediately to the initial state before the water storage. Equilibrium is reached after 2.5 h. A more detailed analysis of the time evolution of water storage in the glassy hydrogel film is achieved by fitting of the individual neutron reflectivity curves (see figure 1.9 (c) and (d)). From these fits the total P(S-*b*-NIPAM) film thickness and solvent penetration (v/v%) are determined. Two regimes of water storage can be distinguished: an initial regime (stage I) describing mass uptake is followed by the main water storage regime (stage II). This storage behavior in the second regime can be considered to be a pure diffusion process in agreement with a model explaining gel swelling kinetics [3].
All over the glassy hydrogel film swells only by 1.2 nm. This extremely small total increase after water storage is the striking point for applications requiring an unchanged film thickness. It shows that the large PS volume fraction seriously reduces the swelling capability of the P(S-*b*-NIPAM) film.

[1] W. Wang, K. Troll, G. Kaune, E. Metwalli, M. Ruderer, K. Skrabania, A. Laschewsky, S.V. Roth, C.M. Papadakis, P. Müller-Buschbaum, Macromolecules **41**, 3209-3218 (2008)

[2] K. Troll, A. Kulkarni, W. Wang, C. Darko, A.M.B. Koumba, A. Laschewsky, P. Müller-Buschbaum, C.M. Papadakis, Colloid Polym. Sci. **286**,1079-1092 (2008)

[3] Y. Li, T. Tanaka, J. Chem. Phys. **92**, 1365 (1990)

1.6 Thin poly(monomethoxy diethyleneglycol acrylate) films on solid supports

Q. Zhong, W. Wang, A. M. Bivigou-Koumba[1], A. Laschewsky[1], P. Müller-Buschbaum

[1] Universität Potsdam, Golm, Germany

Environmentally-sensitive polymers, which exhibit interesting property changes have attracted more and more attention. In response to various external stimuli such as temperature, PH, liquid composition and electric stimulation, characteristic properties change. This causes strong interest due to a variety of applications, such as drug delivery systems [1], substrates for cell cultures [2] and valves for control of liquid flow [3]. So far research is focussed on a few selected systems such as poly(N-isopropylacrylamide) (PNIPAM). PNIPAM received special interest due to having the lower critical solubility temperature (LCST) at 32 ° C, which is close to human body temperature. However for technical applications a LCST closed to the room temperature will limit its use. For example, in tropical countries, which have mean temperature well above 32 ° C, PNIPAM will not be useable without installation of cooling systems.

The novel thermo-responsive homopolymer poly(monomethoxy diethyleneglycol acrylate) (PMDEGA) exhibits a larger LCST as compared to PNIPAM and thus might be an interesting alternative to the use of PNIPAM.

Besides applications which require bulk material, the field of applications based on thin films, such as sensors, is rapidly emerging. In contrary to PNIPAM the system PMDEGA is less investigated and no examples of thin films on solid supports are published. Consequently, within the present work, the preparation of homogeneous thin films of PMDEGA is focussed. As common for polymer films, with the use of different concentrations in the spin-coating process, thin PMDEGA films are prepared on silicon substrates.

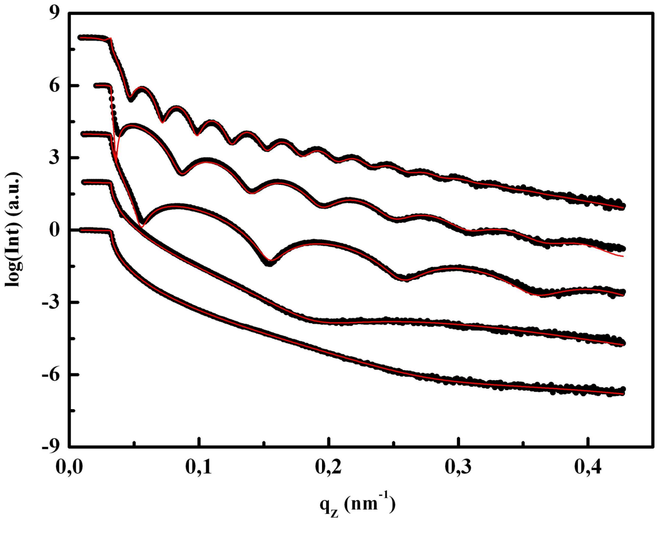

Figure 1.10:
X-Ray reflectivity data (dots) and model fits (slod lines) of PMDEGA films on Si supports prepared by spin-coating. From the bottom to the top the concentration of the PMDEGA solution increases. The curves are shifted along the intensity axis for clarity of the presentation.

The preparation process is as following: The silicon substrates are placed in dichloromethane, heated to 46 ° C for 30 minutes. After that, they are cleaned with Millipore water to remove the dichloromethane. Then the substrates are placed in an oxidation bath with 350 mL H_2O, 30 mL H_2O_2 and 30 mL $NH_3{\cdot}H_2O$ at 65 ° C. After the placing the substrates in the solution, the temperature is kept at 76 ° C for 2 hours. Finally the substrates are again cleaned with Millipore water to remove any possible traces immediately before spin-coating. During the spin-coating, the speed is kept at 2000 rpm/min and the time lasts 30 seconds.

In order to get the relationship between the PMDEGA concentration and the film thickness, 7 samples with concentrations varying from 0.5 mg/mL to 30 mg/mL are prepared. Water is used as solvent and directly after spin-coating the PMDEGA films are probed with X-ray reflectivity to measure the thickness. At PMDEGA concentrations larger than 20 mg/mL, the solute cannot be totally solved in the water. Thus the PMDEGA films obtained with concentrations of 20 mg/mL and 30 mg/mL are inhomogeneous as probed with optical microscopy. As a consequence, the X-ray reflectivity data show no fringes.

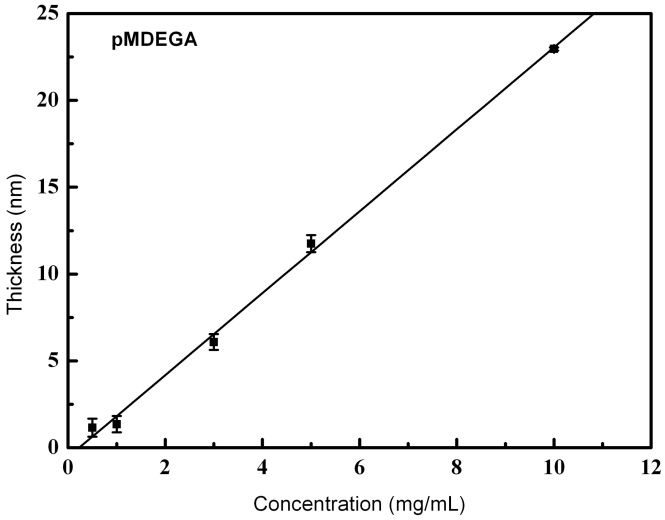

Figure 1.11:
The linear fit curve of the concentration versus the film thickness. It can be seen that there is a linear increase of film thickness when the concentration increase.

In contrast, the X-ray reflectivity data from the 5 samples with PMDEGA concentration smaller than 20 mg/ml exhibit well established fringes (see Fig. 1.10). In Fig. 1.10 the black dots show the measured data, while the solid lines are the fits done with the program Parratt 32. Central result from the fits is the film thickness of PMDEGA films. In Fig. 1.11 this film thickness is plotted as a function of the PMDEGA concentration of the solution. It is easily seen that when the concentration of the polymer solution increases, the film thickness will increase linearly. Thus PMDEGA behaves in the investigated concentration regime up to 20 mg/ml equal to a common homopolymer and obeys the spin-coating equation [4]. Therefore it is easy to control the film thickness by varying the concentration of the polymer solution for future investigations.

[1] L. Dong, A. S. Hoffmann, J. Controlled Release. **15**, 141 (1991)

[2] T. Okano, A. Kikuchi, Y. Sakurai, Y. Takei, N. Ogata, J. Controlled Release. **36**, 125 (1995)

[3] H. Iwata, M. Oodate, Y. Uyama, H. Amemiya, Y. Ikada, J. Membr. Sci **55**, 119 (1991)

[4] D. W. Schubert, Pol. Bull. **38**, 117 (1997)

2 Thin polymer films

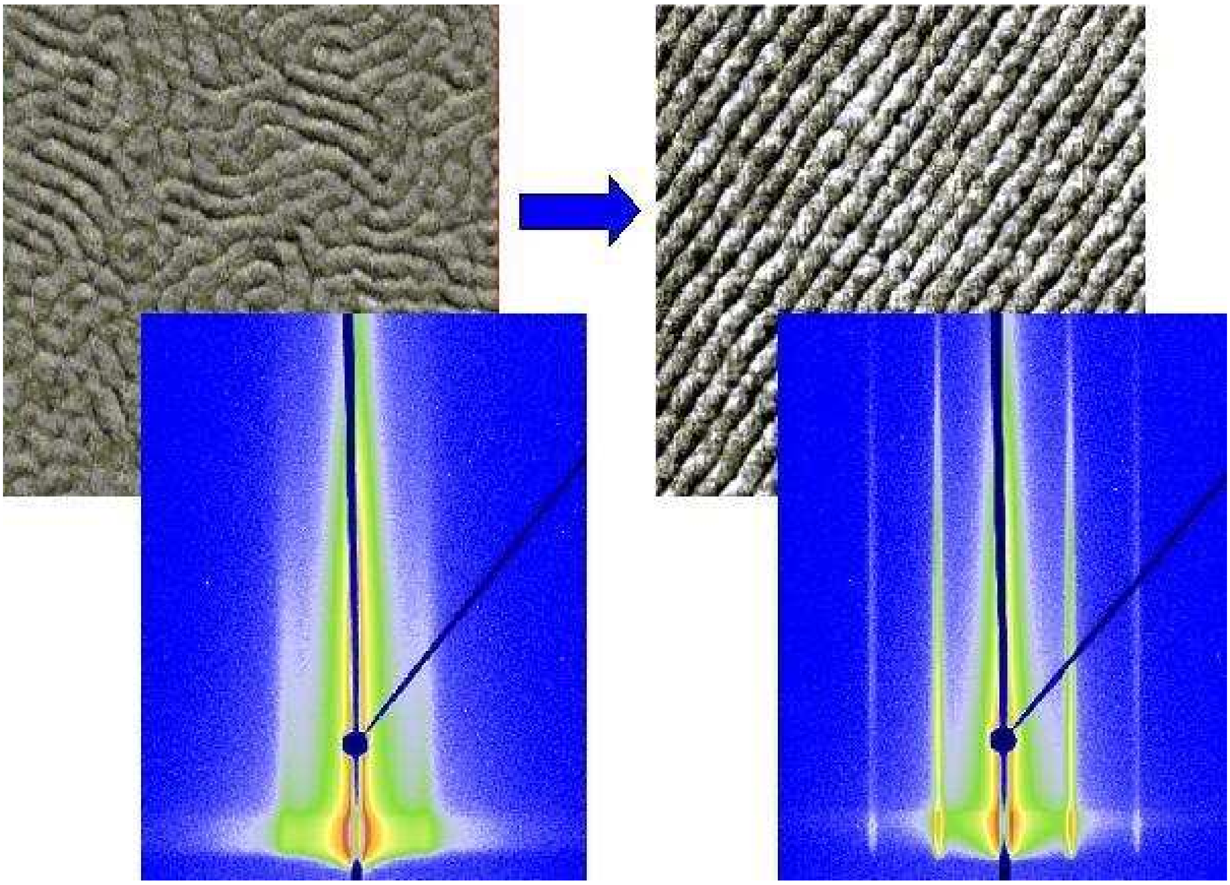

2.1 Solvent content in thin spin-coated polystyrene homopolymer films

J. Perlich, V. Körstgens, E. Metwalli, L. Schulz[1], R. Georgii[2], P. Müller-Buschbaum

[1] Université Fribourg, Fribourg, Switzerland
[2] FRM-II, Garching, Germany

The detection of remaining solvent in thin polymer films is of importance due to its effect on chain mobility and film homogeneity. Moreover it is crucial information for all swelling experiments in order to define the initial "dry" state of the polymer film. Using neutron reflectometry (NR) the remaining solvent content in thin freshly spin-coated polymer films is probed in a non-destructive and non-invasive way [1, 2]. We focus on the well established model system of polystyrene (PS) spin-coated out of toluene onto Si substrates. Key parameters such as the molecular weight of the polymer, the film thickness of the polymer films, different annealing conditions and a long-term aging are addressed.

The investigation relies on the fact that the investigated component of the model system, namely the solvent toluene, can be substituted by the deuterated solvent toluene-d8, without any change to the physical properties of the thin films. Hence, regardless of the protonation or deuteration, both thin films will behave identical. Deuteration of the investigated solvent component results only in a distinct differentiation in the scattering length density (SLD) from all other involved materials, such as polystyrene (PS) and the Si substrate. Therefore, the high contrast of PS and deuterated toluene in SLD is utilized to make the amount of residual solvent inside the thin film detectable. The analysis of the NR data in the narrow range around the critical edge is based on a single layer model, represented by the thin PS film, on a silicon substrate. In order to match the simulated curve with the measured curve of the thin PS film only the SLD of the PS is adjusted, whereas the magnitude of the adjustment represents a measure for the ratio of PS homopolymer to toluene-d8 solvent. The obtained SLD for the best model fit is used to determine the volume fraction of remaining solvent.

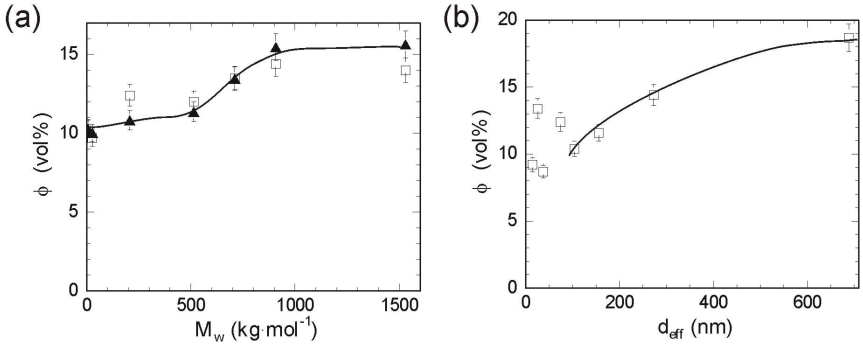

Figure 2.1:
(a) Extracted total retained solvent content ϕ (open squares) shown as a function of the PS molecular weight. The corresponding normalized solvent content ϕ_{norm} of the thin film is plotted as solid triangles. (b) Extracted total retained solvent content shown ϕ as a function of the effective film thickness d_{eff}. The solid lines are a guide to the eye. Taken from [1].

The extracted remaining solvent content ϕ of the thin spin-coated PS films prepared out of PS with different molecular weight is presented in Figure 2.1a. In order to correct for small thickness deviations of the individual samples with respect to the desired mean thickness, a so-called normalized solvent content ϕ_{norm} referring to one reference thickness is also plotted. In general, the solvent content increases with increasing molecular weight from 9 to 15 vol%. Above molecular weights of 1000 kg/mol ϕ (or ϕ_{norm}) remains constant within the error [1]. One reason for the molecular weight dependent increase in the remaining solvent might be the free volume of the PS films, in which the solvent can be retained. Typically, two different sources contribute to the free volume of a polymer film: an intra-molecular contribution and an inter-molecular contribution. For the reason that the increase of molecular weight is probed at roughly constant film thickness both contributions increases, because of the increased degree of polymerization as well as radius of gyration. Hence, for thin films with fixed thickness but with increasing molecular weight the free volume might increase, which acts as free space for the solvent.

Figure 2.1b shows the remaining solvent content ϕ as a function of the effective film thickness d_{eff} for thin films out of PS with M_w = 207 kg/mol. The values of ϕ increase with increasing film thickness. With further increasing film thickness an approach of a limiting value displaying the PS bulk characteristics is likely. However, from the complex interplay between interaction driven solvent enrichment at the substrate interface and the possibility to trap solvent due to limited diffusion, the complex behavior for small film thickness as seen in Figure 2.1b might be explained [1].

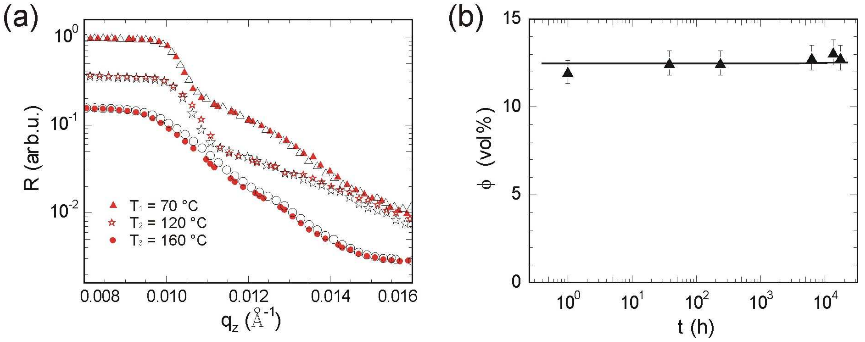

Figure 2.2:
(a) High-resolution NR data in the region of total external reflection of thin films as prepared (open symbols) and after annealing (closed symbols) for 8 h at different temperatures. For clarity, the curves are shifted along the reflectivity axis. (b) Long-term behavior of the total retained solvent content ϕ as a function of the time t since preparation. Taken from [1].

Concerning a systematic reduction of the solvent content, polymer films are cured at selected temperatures. For many applications long-term behavior comprising the aging caused by a change in the remaining solvent is important. To address these points, a series of PS films with fixed film thickness and molecular weight is investigated. As post-production treatment three different annealing temperatures are chosen: 70, 120 and 160 °C. The respective high-resolution scans of the "as prepared" and annealed samples are plotted in Figure 2.2a. The selected conditions were not suitable to remove all remaining solvent. Only a reduction of solvent in the film can be achieved. It is expected, that an increase in annealing time would yield a further reduction. However, we have shown that actually a "dry" film is not a dry film at all, as assumed in many investigations for as-prepared as well as annealed films [1].

Finally, in addition to annealing conditions, the long-term behavior has been investigated over two years. No changes in the effective film thickness have been detected and thus the normalized solvent content shows the identical behavior as presented in Figure 2.2b. In the full period of two years the solvent content in the PS film remains constant at about 12.6 vol%. Therefore, no aging, in terms of changing the retained solvent, is verifiable and no mechanical alteration of the thin PS film is expected, supported by the optical investigation which also show no changes [1].

[1] J. Perlich, V. Körstgens, E. Metwalli, L. Schulz, R. Georgii, P. Müller-Buschbaum, Macromolecules **42(1)**, 337 (2009)

[2] R. Georgii, P. Böni, M. Janoschek, C. Schanzer, S. Valloppilly, Physica B **397**, 150 (2007)

2.2 First results on Brillouin scattering from thin transparent polymer films

J. Wiedersich, A. Diethert, P. Müller-Buschbaum, W. Petry

Polymer films are extensively used for technical applications, the most prominent example being protective and functional coatings on solid surfaces. The knowledge of their elastic properties is of paramount importance for a broad range of applications. It is obvious that for thick films the stiffness of the material will approach the value for bulk material. As the thickness of those films is reduced, it has to be expected that drastic changes to the elastic properties occur – especially for a film thickness on the order of the size of a polymer molecule, ie. in the range below of several tens of nano meters. For a long time it has therefore been a goal to measure the elastic properties of thin films and nano structured surfaces.

Recently, predictions of a dramatic decrease of the Young's modulus have been confirmed on films of a thickness of less than about 40 nm, employing a mechanical, so called buckling method [1]. However, these measurements are limited to films that are either peeled off the surface or that are coated on very soft substrates.

In contrast to this, Brillouin light scattering (BLS) is a contact free method that permits to determine the elastic properties of both transparent and opaque materials directly. For opaque materials, the method is limited to the surface layer. Several research groups have used BLS to probe the elastic properties of both anorganic and polymer films. Because of the small scattering volume of (ultra) thin films, these studies have been limited to rather thick films or to films on opaque substrates (where the BLS signal is enhanced). Quite recently the group in Mainz substantially extended the applicability of BLS and for the first time succeeded in measuring the Brillouin signal from thin transparent films on transparent substrates [2]. Down to the thinnest films accessible to BLS (≈ 40 nm) *no* deviations of the elastic constants with respect to the bulk values were observed.

In conventional backscattering geometry, the frequency of the Brillouin line depends both on the sound velocity v_s and the refractive index n of the sample. In order to unambiguously determine the sound velocity, which is directly related to the elastic modulus, we therefore choose the so-called platelet geometry. In this special 'transmission' configuration, the frequency of the Brillouin line does not depend on n, but is directly given by $\nu_\mathrm{B} = \frac{2\pi}{\lambda} v_\mathrm{s}$ (cf. fig. 2.3). Unfortunately, though, this leads to a smaller scattering volume than for back scattering. Further more the scattering volume is also reduced with decreasing film thickness. The graph on the left of figure 2.3 also shows that the scattering from the glass substrate is much stronger than the signal from the shown 350 nm film. Another feature of this platelet scattering geometry shown on the left of figure 2.3 is the fact that the scattering vector $\mathbf{q}$ is parallel to the surface of the substrate.

As the spectra of figure 2.3 with our first results on thin films demonstrate, these limitations have been – at least partially – compensated by significant improvements to the alignment procedure and by employing a stronger laser. For the homogenious bulk polymer shown in the top graph on the right, the sound velocity and the scattering geometry determine the frequency at which the Stokes and anti Stokes Brillouin lines are observed (transversal phonons are not observed within the VV scattering geometry). As the sample thickness is reduced, the breaking of the isotropic symmetry is manifested by a splitting of the Brillouin lines: there appear several film guided modes with sound velocities both higher and lower than the bulk value. The frequencies of the modes increase as the films become thinner. At the lowest nominal thickness of 65 nm, the sound velocities of all film modes are higher as the sound velocity of the bulk.

The evaluation of the data is rather complex, compared to the evaluation of Brillouin lines in bulk materials. While the Brillouin frequency in conventional spectroscopy on isotropic bulk materials just depends on q, n and the elastic properties of the material, in the case of thin films, the number of lines and their respective positions also depends on the film thickness. A detailed

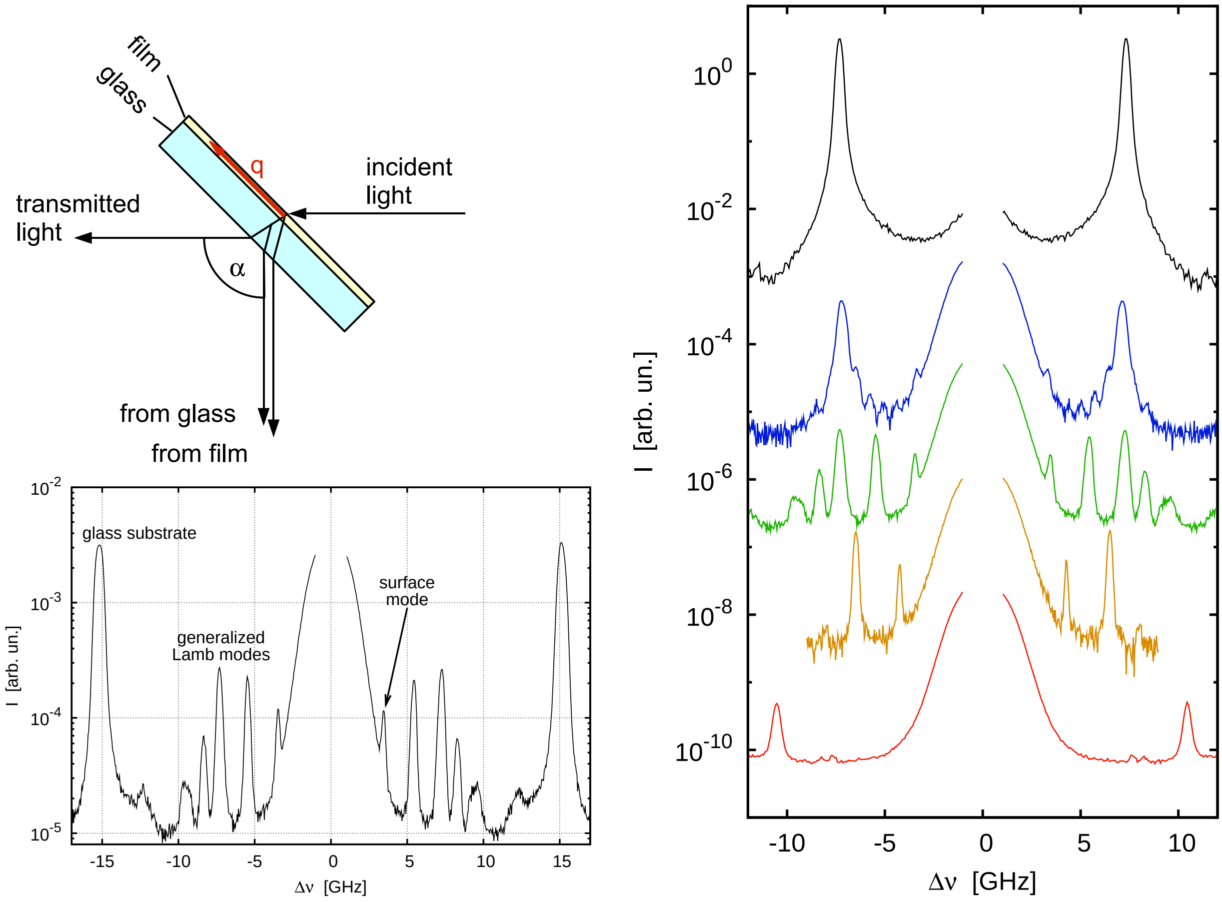

Figure 2.3:
The top left figure schematically shows the scattering geometry of the platelet geometry. The bottom left figure shows an example of film guided modes of a thin PMMA film including the Brillouin line of the substrate at high frequencies. The figure to the right shows different Brillouin spectra of different PMMA films recorded at 90° scattering. From top to bottom the nominal thicknesses are: bulk, 2000 nm, 675 nm, 350 nm, 65 nm.

analysis is presently in progress.
The progress in instrumentation allows us to measure Brillouin lines of thin and ultrathin films with excellent signal to noise ratio. The scheduled upgrade to higher precision optical components will better accommodate for the tighter alignment requirements of ultra thin films. We are looking foreward to beeing able to resolve Brillouin lines of even thinner films, for which strong deviations from the bulk elastic constants have been predicted.

[1] Christopher M. Stafford, Bryan D. Vogt, Christopher Harrison, Duangrut Julthongpiput, and Rui Huang. *Macromolecules*, 39:5095–5099, 2006.

[2] W. Cheng, R. Sainidou, P. Burgardt, N. Stefanou, A. Kiyanova, M. Efremov, G. Fytas, and P. F. Nealey. *Macromolecules*, 40(20):7283–7290, 2007.

2.3 Viscosity and density of polymer melts at the interface of solids

E.T. Hoppe, A. Münzer, C.M. Papadakis

The properties of a polymer melt close to a solid interface may be significantly altered compared to the bulk, e.g. the chain conformations, the density and the chain dynamics.[1-3] This has implications on the stability of coatings, e.g. in medical implants or in chip fabrication, and the stability of blends of polymers with nanoparticles. However, not only the structural changes near a solid interface are of importance, but also the dynamics, i.e. the local mechanical properties.

The goal of the project is to achieve an improved understanding of the interphase of a polymer-solid contact by correlating the mass density, i.e. the polymer structure, with the local viscosity, i.e. the polymer dynamics, near the solid interface.At this, we have chosen polybutadiene (PB) as a model system with a wide range of molar masses.
The interphase viscosity will be determined with fluorescence correlation spectroscopy (FCS) where the interphase near the substrate will be selectively illuminated using total internal reflection (TIR) excitation. The mass density profile of polymers near the substrate will be determined with high-resolution neutron reflectometry (NR). These two experimental techniques have different physical requirements on the substrates. For TIR-FCS, the substrate has to be transparent in a wavelength range from 450 to 650 nm. For NR, on the other hand, the substrate has to be transparent for neutrons, highly homogeneous and flat. The surface energy properties of both substrates should be equal. For these reasons, glass substrates were chosen for TIR-FCS and silicon wafers for NR. In order to obtain stable coatings even with low molar mass PB, the commonly used substrate preparation protocols like acid or basic cleaning must be improved.
Since PB is non-polar the adhesion of the PB coating to the substrate can only occur by dispersive interactions. The often used acid and basic substrate cleaning, however, result in surfaces with large polar interaction components, and thus the PB coatings are not stable on these substrates. We have therefore modified the substrates with a monolayer of methyltriethoxysilane which binds covalently to both glass and silicon and exposes methyl groups to the PB coating. In this way, both the TIR-FCS and the NR substrate have the same interaction components with the PB coating at the interface without altering the optical properties. Using silanes for surface modification offers a number of possibilities to vary the substrate-PB interaction. The contact angles of PB on acidic cleaned and silanized surface, however, do not show a large difference, but a significant difference to the untreated substrate (Fig. 2.4).

Figure 2.4:
Contact angle of PB of 4200g/mol on (a) untreated glass untreated glass ($\approx 41.5\,^\circ$) (b) on glass with acid cleaning ($\approx 28.0^\circ$) (c) on glass silanized with a monolayer of methyltriethoxysilane ($\approx 27.5^\circ$).

The surface tensions and the polarities (i.e. the polar interaction component of the surface tension divided by the surface tension) of the glass and the silicon substrates are shown in Fig. 2.5 Compared to the untreated substrates, both values increases significantly after acidic cleaning. Adding subsequently the monolayer of methyltriethoxysilane results in a slight decrease of both the surface tension and the polarity. Silanization thus renders different

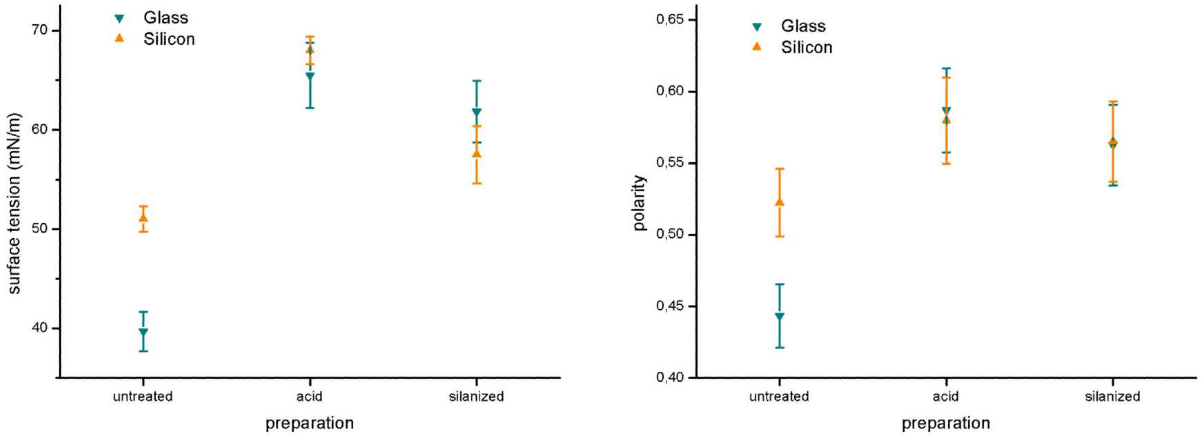

Figure 2.5:
Surface tension (left) and polarity (right) after different preparations of glass (triangle up) and silicon (triangle down). Values derived from contact angle measurements of water, a 50:50 wt./wt. ethyleneglycol/water mixture and diiodomethane using the method of Owens and Wendt.[4]

substrates comparable. The slight decrease in contact angle of PB on the silanized surface could point to a better adhesion. By using different silanes, it will also be possible to vary the interfacial interaction on glass and silicon in a simple way. Moreover, the silane coating may also protect the silicon from oxidation.
In summary, we have prepared substrates for TIR-FCS and NR measurements with comparable surface interaction components by applying a monolayer of covalently bonded silane to the substrates. This step is not expected to affect the measurements.

The project is funded by DFG within the priority program ”Polymer-Solid Contacts: Interfaces and Interphases”.

[1] J.H. van Zanten, W.E.Wallace, W.L.Wu, Phys.Rev.E **53**, 2053 (1996)

[2] R.A.L. Jones, Curr. Opin. Coll. Inter. Sci. **4**, 153 (1999)

[3] C.B.Roth, J.R.Dutcher, J. Electroanalytical Chemistry **584**, 13 (2005)

[4] D.K.Owens, R.C.Wendt, J. Appl. Pol. Sci. **13**, 1741 (1969)

2.4 Improvement of quantum efficiency of photomultiplier tubes by humidity controlled coatings based on porous polymer structures

V. Körstgens, C.-C. Hsu[1], D. Paneque[1,2], J. Wiedersich, P. Müller-Buschbaum

[1] Max-Planck-Institut für Physik, München

[2] Stanford Linear Accelerator Center, USA

Photomultiplier tubes (PMTs) are light sensitive devices with single photon detection capabilities and time resolution of the order of 1 ns. Because of these characteristics PMTs are used as sensors in large air Cherenkov telescopes for ground-based gamma-ray astronomy. Individual PMTs with a hemispherical photocathode and borosilicate window are configured into large area sensors. The light sensitivity of a PMT can be described with the quantum efficiency (QE) parameter. The QE is the probability of emitting a photoelectron per incoming photon. The QE depends on the wavelength of the photon. The QE of the PMTs is of high importance for the application in an air Cherenkov telescope since the higher the QE of the PMTs in the sensor the lower is the energy threshold of the telescope [1]. So far a considerable improvement of QE was found after the application of a coating onto the hemispherical PMTs. The improvement of QE in these studies was given on the one hand by extending the spectral sensitivity in the short-wave UV-range and on the other hand, by increasing the overall QE by applying a matt coating acting as a photon scatterer. 1,4-diphenylbenzene (*p*-terphenyl) turned out to be a suitable wavelength-shifter for bypassing the spectral cut-off of the borosilicate window of the PMT around 310 nm. In order to get a mechanical resistant coating it was necessary to coat the wavelength-shifter within a polymer matrix. We developed a temperature- and humidity-controlled procedure which allows for convenient and reproducible coating of PMTs [2].

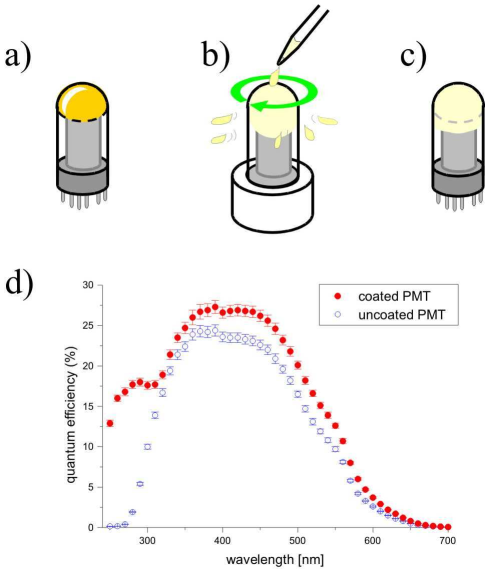

Figure 2.6:
Sketch of the coating procedure a) uncoated PMT, b) PMT fixed in Teflon screw-in holder rotating on spin coater; solution is poured on while PMT is rotating, c) coated PMT removed from holder, and d) QE for an ET9116A PMT before and after being coated as described in the text.

PMTs (Electron tubes 9116A) with hemispherical window are coated with a solution of a binary copolymer consisting of methyl acrylate and ethyl methacrylate with p-terphenyl in dichloromethane. The untreated PMT (fig. 2.6a) is fixed into the custom made screw-in holder of teflon connected to the spin-coater. A few mL of the solution is poured onto the center of the PMT while it is rotating with 500 rpm. The hemispherical part of the PMT is fully covered with solution within a few seconds whereas excess liquid is rotated off (fig. 2.6b). The whole set-up including the spin-coater is placed in a box where humidity is set to 63% r.h. at 23 °C. After the coating procedure the PMTs are removed from the screw-in holder (fig. 2.6c) and the surface structure is investigated with an optical microscope. Micrographs reveal the structure of the turbid layer (fig. 2.7a-c). On the center of the surface of the hemispherical PMT individual crystals can be distinguished (fig. 2.7a). Further magnification shows the porous structure (fig. 2.7b). The porous structure is continuous over the whole surface including the crystal grains. Fig. 2.7c shows an arbitrary chosen single crystal of *p*-terphenyl with a superposed porous structure of the polymer matrix. In this micrograph the porous structure on top of the crystal is visible only since the porous structure of the surrounding of the crystal is out of focus of the microscope. The fact that these structures only evolved at conditions with a certain relative humidity are indication for a breath figure induced structure.

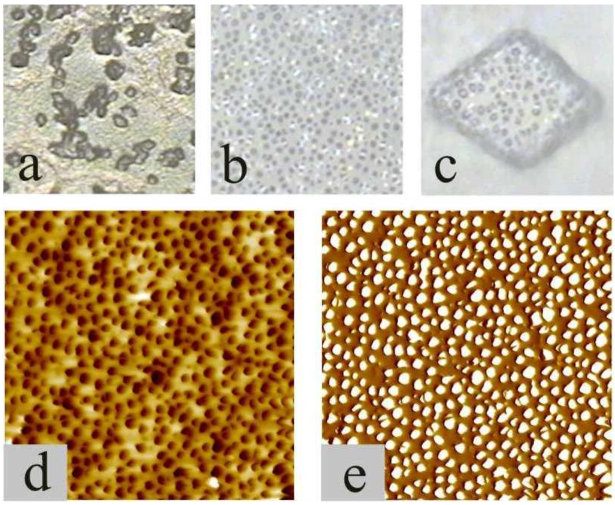

Figure 2.7:
Surface characterization: optical micrographs of turbid coating of PMT. (a) Individual crystals of p-terphenyl as part of the coating, image size 250×250 μm^2, (b) porous structure of polymer matrix, image size 25×25 μm^2, and (c) porous structure is continuous superposing the individual crystals, image size 25×25 μm^2. AFM images of coating of acrylate and *p*-terphenyl on silicon wafer (d) topography, z range 900 nm, and (e) phase image, image size 15×15 μm^2.

The QE of the used PMTs is measured as a function of wavelength before and after coating (fig. 2.6d) [1, 2]. The increase in QE at low wavelengths up to 320 nm clearly can be attributed to the wavelength-shifter. The increase of QE at wavelengths larger than 320 nm cannot be attributed to the wavelength shifter but is caused by the structure of the coating. The structured coating acts as photon scatterer, increasing the path length of the photon in the photocathode material, and hence resulting in higher probabilities of photons exciting an electron at the photocathode. The overall increase in QE as compared to uncoated PMTs is 17% [2].

As the improvement of QE by application of the matt coating is demonstrated, additional topographical information is useful to rule out the effect of the curved surface of the PMT and of the material coated. Therefore a corresponding flat sample is prepared under identical conditions and investigated with atomic force microscopy. Instead of the curved borosilicate glass surface a flat silicon substrate with its native oxide layer is coated. The surface structures are investigated with a surface probe ellipsometric microscope (SPEM, Nanofilm GmbH) equipped with an AFM (ULTRA objective, SIS GmbH) used in non-contact mode. The open pore structure is revealed in topography (fig. 2.7d). From the phase image (fig. 2.7e) an average pore radius of 210±40 nm is determined.

This work presented is one example for the application of structure forming methods based on breathfigures. Porous often highly ordered structures are obtainable from a lot of different polymers and nanoparticles in various solvent systems in a range of pore sizes from 50 nm to 20 μm.

[1] D. Paneque, H. J. Gebauer, E. Lorenz, M. Martinez, K. Mase, R. Mirzoyan, A. Ostankow, T. Schweizer, Nucl. Instrum. Methods. Phys. Res. A **504**, 109 (2003)

[2] V. Körstgens, C.-C. Hsu, D. Paneque, J. Wiedersich, P. Müller-Buschbaum, Appl. Phys. Lett. **93**, 041916 (2008)

2.5 Surface Enrichment Layers In Pressure Sensitive Adhesive Films

A. Diethert, P. Müller-Buschbaum

Pressure sensitive adhesives (PSAs) are used for many different applications, such as for example adhesive foils or binding materials. A prominent class of PSA films is based on statistical copolymers. Typically, two or three different monomers are combined in the statistical copolymer to balance the different requests of the PSA [1-4]. The adhesive properties of the PSA films are mainly determined by surface-near regions. However, detailed information about surface structures of such adhesive films is still missing.

In the presented work we focus on PSA model systems of statistical copolymers consisting of two different types of monomers. In one series of samples the polymer chains are composed of 80% poly(tert-butyl acrylate) (PtBA) and 20% poly(methyl acrylate) (PMA) with different molecular weights. A second series of polymers uses 90% poly(ethyl hexylacrylate) (PEHA) and of 10% of a second monomer which is referred to as the minority component. Different types of monomers are used for the minority component, such as poly(maleic acid anhydride) (PMAA), polystyrene (PS) or poly(methyl methacrylate) (PMMA).

The PSA films were prepared with solution casting on pre-cleaned glass substrates. From a naive point of view, one would have expected homogenous films which are characterized by the average monomer composition. To investigate the surface structure, we probed the density profile perpendicular to the PSA surface using x-ray reflectivity (XRR) for the first series. For the second series we performed grazing incidence small angle x-ray scattering (GISAXS) measurements to prove the existence of lateral structures.

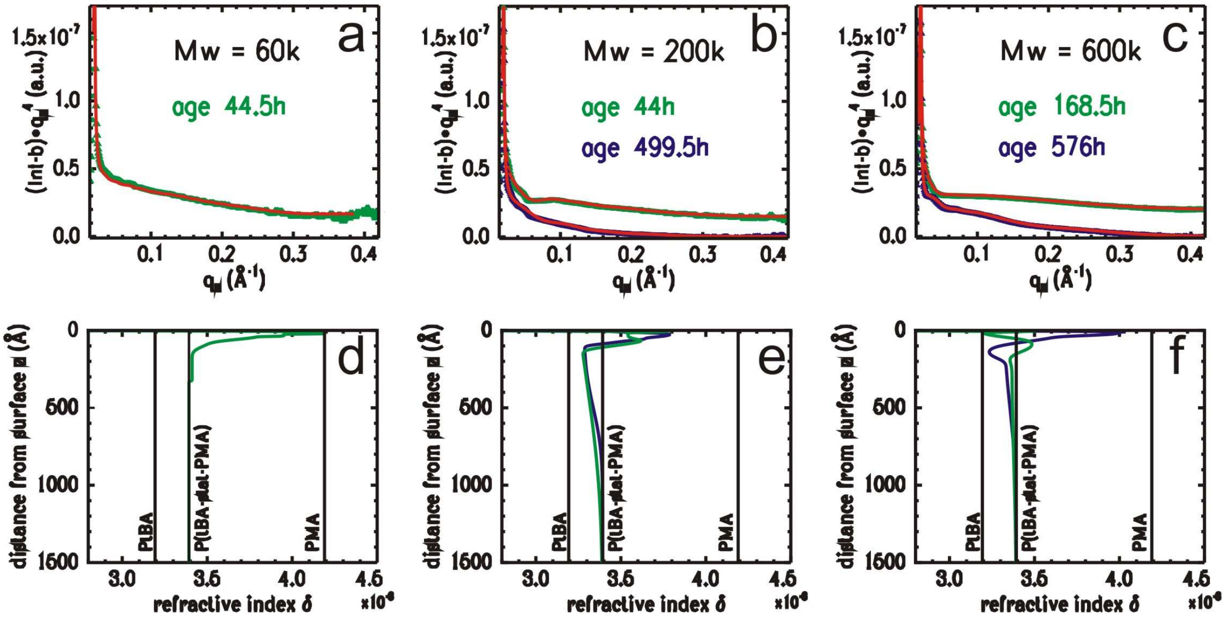

Figure 2.8:
X-ray reflectivity data and fits of the statistical copolymer with 80% tBA and 20% MA and a molecular weight of a) 60k, b) 200k and c) 600k and the resulting refractive index profiles

The XRR measurements were performed with a Siemens D5000 diffractometer using a wavelength of 1.54 Å. For the data analysis we used Parratt32, a simulation tool for neutron and x-ray reflectivity.

The figures 2.8 a, b and c show reflectivity curves in a typical representation, which is beneficial for thin enrichment layers. The curves plotted in green color represent freshly prepared samples (see sample age within the respective figures) and the curves plotted in blue color show data from samples which were stored for more than twenty days under room temperature conditions. The red solid lines are the fits to the data performed with Parratt32. The figures 2.8 d, e and f show the corresponding refractive index profiles where $z = 0$ denotes the sample surface. The black solid lines are positioned at the values of the refractive indices of the corresponding homopolymers related to the involved copolymers. For higher molecular weights (figure 2.8 e and f), freshly prepared samples show no or only a little surface enrichment of the PMA component. During aging, the PMA content near the surface is increased in such a way that the surface is dominated by the PMA component. For the low molecular weight sample (figure 2.8 d) the PMA component is enriched at the surface even for the freshly prepared sample. The reorganization process at low molecular weight is much faster than for high molecular weight samples. In any case this is a surface effect. For a depth $z > 100\,\text{nm}$ the average monomer composition is reached, which is $80 : 20$ for the investigated system.

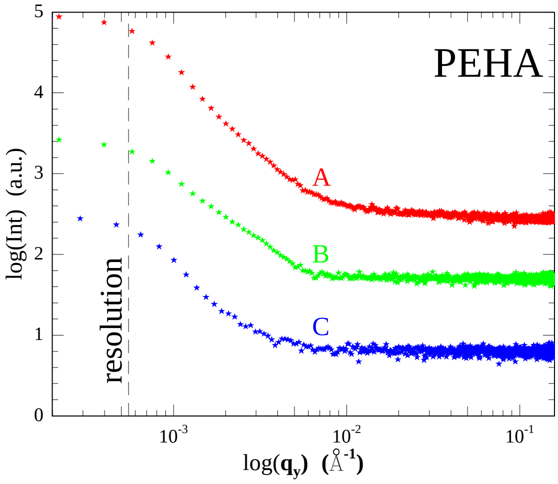

Figure 2.9:
out-of-plane-cuts at the critical angle of the majority component PEHA for the following statistical copolymers: A) P(EHA-stat-MAA), B) P(EHA-stat-S) and C) P(EHA-stat-MMA)

In addition to the layering along the surface normal, which is caused by the enrichment of one monomer component of the statistical copolymer, a lateral structure can be present in the films. To detect such lateral structure grazing incidence small angle X-ray scattering (GISAXS) experiments were performed.

For the second series of samples, GISAXS measurements were performed with synchrotron radiation (wavelength of 1.38 Å and a beamsize of 40 μm x 20 μm) at the beamline BW4 at HASYLAB in Hamburg. The incident angle on the sample surface was selected to 0.506° and the distance between the sample and the detector was 2.004 m. A 2D-MarCCD detector (2048 x 2048 pixels with a pixel size of 79 μm) was used to record the scattered x-rays from the film surface.

The so called out-of-plane cut through the 2D-scattering pattern is selected in order to look for the evidence of lateral structures. It is oriented parallel to the sample surface and perpendicular to the beam direction (along y-axis). Usually the out-of-plane cuts are made at the critical angles of the sample materials.

Figure 2.9 shows the out-of-plane cuts for the three polymers of the second series. The shoulders in these curves clearly indicate the presence of lateral structures. Detailed data analysis is ongoing and will bring more information about size and shape of these structures.

[1] C. Anderson, Ind. Eng. Chem. **61**, 48 (1969)

[2] L. Lacrout, C. Creton, A. Dongchan, K. R. Shull, Macromolecules **34**, 7748 (2001)

[3] Y. Kano, H. Ushiki, S. Akiyama, J. Adhesion **43**, 223 (1993)

[4] A. Aymonier, E. Papon, J.-J. Villenave, Ph. Tordjeman, R. Pirri, P. Gérard, Chem. Mater. **13**, 2562 (2001)

2.6 Morphological transition of block copolymer film at the interfaces: A TOF-GISANS study

E. Metwalli, J.-F. Moulin[1], P. Müller-Buschbaum

[1] GKSS-Forschungszentrum, Geesthacht, Germany

Thin polymer films have recently attracted an immense attention because of their use in many potential applications such as coatings, insulators, and adhesive. Moreover, thin polymer films have been also used to create templates for patterning inorganic materials which are involved in the fabrication of nano-devices. For example, diblock copolymer thin films are successfully used in fabrication of low-cost and easy processable nano-systems with high degree of complexity and functionality [1]. The chemically distinct and immiscible polymer blocks in block copolymers micro-phase separate and self-assembly into ordered patterned on a scale of nanometers. Information on polymer film structures along the film depth from the polymer-surface to the free interface can be probed using grazing incidence small angle neutron scattering (GISANS) at many different incidence angles [2,3]. Compared with the fixed wavelength counterpart method GISANS, the advanced time-of-flight GISANS (TOF-GISANS) technique has the advantage that it is capable to simultaneously measure over a wide range of momentum transfer in a single experiment without the need to alter the incidence angle, collimation or sample-to-detector distance. In other words, TOF-GISANS enables several simultaneous GISANS measurements with different wavelengths (i.e scattering vectors) in a single measurement.

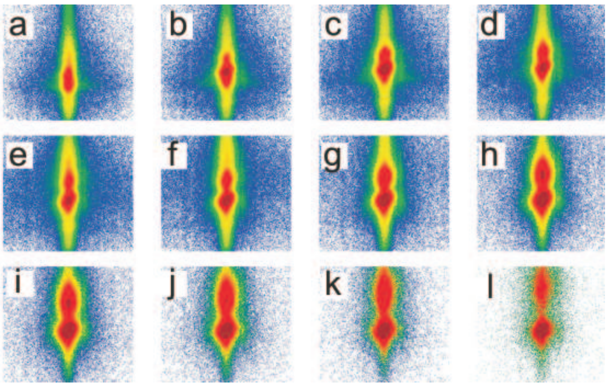

Figure 2.10:
Selection of twelve 2d scattering patterns (only reflected neutrons) as measured simultaneously in the TOF-GISANS experiment. A strong Bragg reflection peak that changes its position at different wavelengths relative to a fix position specular peak in the middle of the 2d image is observed

In the present work, TOF-GISANS was used to investigate the structure of polystyrene (deuterated)-block-polyisoprene, denoted P(dS-*b*-I), diblock copolymer thin films. In the bulk the P(dS-*b*-I) diblock copolymer forms a cylinder structure due to its composition (f_{PdS}=0.3). In the thin film geometry, wetting properties of the polymer blocks to the solid surfaces are examined. Structures parallel and perpendicular to the polymer film deposited on two substrates with different surface energies were tested. To enhance the sensitivity of our measurements at the polymer-solid interface the measurements were performed with the neutron beam impinging on the sample from the silicon side. The measurement from the air side was done for comparison. Both air and silicon side measurements of the polymer film structure are compared and discussed based on the effect of surface chemistry and surface energy on the polymer morphology. Two samples with different surface energy were used. One pre-cleaned piece of silicon was further spin coated using 3-aminopropyltriethoxysilane (APS) aqueous solution (10% v/v)

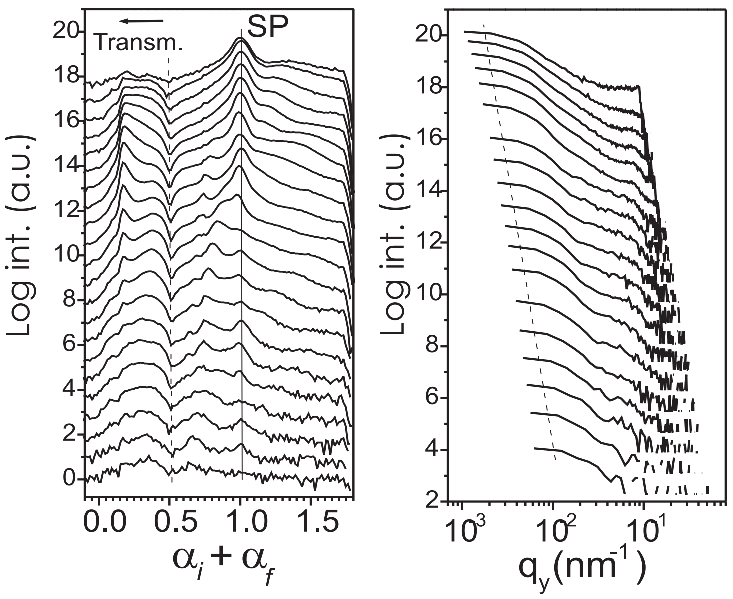

Figure 2.11:
The logarithmic intensity as a function of the detector angle α_i+ α_f (left) and out-of plane scans q_y(right) corresponding to the different TOF channels for the polymer film

followed by rinsing in DI water and finally heat treated at 75 °C for 2 h. The contact angle of the aminosilane coated sample has an average value of 55°. Both the low (as-cleaned) and high (APS coated one) contact angle samples were spin coated using P(dS-*b*-I) solution with toluene as a solvent. The polymer films were heat treated at 120°C for 36 h. The diblock copolymer has a fully deuterated polystyrene block. The polymer film thickness is 250 nm for all prepared samples. The TOF-GISANS measurements were collected where the sample in a horizontal position at an angle of 0.5° with respect to the beam and the sample at a distance of 10 m from the detector. Figure 2.10 shows some selected 2d scattering patterns of the polymer film. An intense specular peak is observed in the middle of the 2d scattering images. The number of total TOF channel (corresponding to different wavelengths) collected at REFSANS was about 26 and due to the limited beam intensity at the very small and large mean wavelengths, the middle 22 channels were used for data analysis (figure 2.11).

On both weak Si/SiO$_x$/APS and strong Si/SiO$_x$ surface fields, TOF-GISANS showed only Bragg reflections from the polymer film. On the APS coated substrate these Bragg reflections indicate a possible perforated lamella (PL) layer morphology parallel to the surface plane with a domain spacing of 29 nm. The PL phase, which is a metastable in the bulk, is stabilized in P(dS-*b*-I) diblock copolymer thin films supported on the aminosilane (APS) treated substrate. The surface reconstruction of the polymer film does not seem to extend overall the whole film thickness due to the competition between the reorientation of the domains under the effect of surface field and the compositionally stable cylinder morphology. The top most layers at the free interface indicated an ill-defined structure compared with that at the polymer-surface interface. Such systematic information on the film structure along the film depth was only possible with the current set up of the TOF-GISANS at REFSANS spectrometer.

[1] S. R. Quake, A. Scherer, Science **290**, 1536 (2000).

[2] P. Müller-Buschbaum, L. Schulz, E. Metwalli, J.-F. Moulin, R. Cubitt, Langmuir, ASAP article, (2009).

[3] P. Müller-Buschbaum, L. Schulz, E. Metwalli, J.-F. Moulin, R. Cubitt, Langmuir **24**, 7639 (2008).

2.7 Lateral structures of buried interfaces in ABA-type tri-block copolymer films

P. Müller-Buschbaum, L. Schulz[1], E. Metwalli, J.-F. Moulin[2], R. Cubitt[3]

[1] Université de Fribourg, Fribourg, Switzerland
[2] GKSS-Forschungszentrum, Geesthacht, Germany
[3] ILL, Grenoble, France

Concerning block copolymers, the A-B di-block constitutes the simplest copolymer architecture. While the morphologies and properties of copolymers with more complex linear architectures have been investigated, we focus here to the A-B-A tri-block design. As with A-B di-block copolymers, A-B-A tri-blocks can microphase-order into the classical morphologies [1]. In contrast to A-B di-block copolymers, the mean-field phase diagrams of A-B-A tri-block copolymers are highly asymmetric as a result of the higher entropic penalty in deforming the central B blocks so as to accommodate the two outer blocks into the A domains. The principal difference between the two architectures, di-block and tri-block, is the double-tethered nature of the B mid-block in the tri-block. Each mid-block adopts either a bridged or looped conformation by depositing its ends (the block junction sites) in adjacent interphases or the same interphase, respectively. According to self-consistent field theory (SCFT) and supported by experiments, the bridging fraction lies between 0.40 and 0.45 for copolymers of modest incompatibility. As compared to bulk morphologies, in thin films the interaction with the confining asymmetric wall (substrate and air interface) can modify the morphologies. Extensively studied for di-block copolymers, the interface energies in combination with the spatial restrictions introduced by the film thickness drive the film morphology. A preferential selectivity of one wall starts to order the copolymer film thereby yielding an alignment of the structures parallel to this interface. In tri-block copolymer films in addition to a comparable behavior of surface induced ordering deviations from the bulk structure were reported.

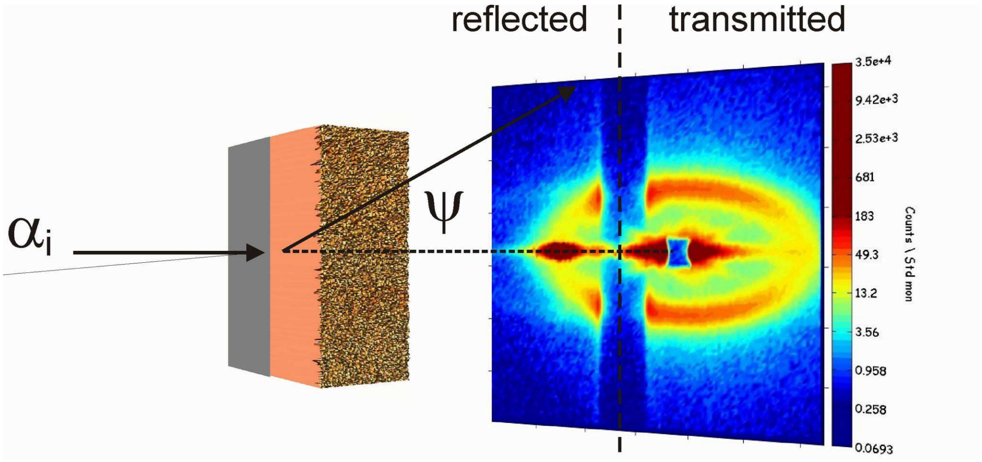

Figure 2.12:
Schematic picture of the experimental set-up used in the GISANS measurements. The neutron beam impinges through the silicon substrate. The incident angle with respect to the sample horizon is denoted α_i, the exit angle α_f and the out-of plane angle ψ. With the two-dimensional detector the reflected and transmitted signal is probed.

Within this investigation we present a novel and alternative approach to probe non-destructively buried interfaces. It is based on grazing incidence small angle neutron scattering (GISANS) [2]. To show the possibilities of this method, we select a model system which consists of a bulky tri-block copolymer film on top of a silicon substrate with a thin oxide layer

(SiOx). An A-B-A tri-block copolymer with two equal end blocks was chosen to obtain a micro-phase separation structure of lamellar type. The substrate surface energy was modified by 4 different treatments [3] covering a hydrophilic and a more hydrophobic surface type. The nano-structure due to micro-phase separation of the tri-block copolymer is measured. We probe the differences between the structure close to the substrate surface and the bulk structure [4]. Following the sample geometry which is successfully used in neutron reflectometry the neutron beam impinges not from the polymer film surface but through the silicon (Si) substrate (see fig. 2.12). Upon variation of the incident angle in the GISANS experiments interface sensitivity was achieved. GISANS measurements were performed at the D22 beamline at the neutron reactor ILL.

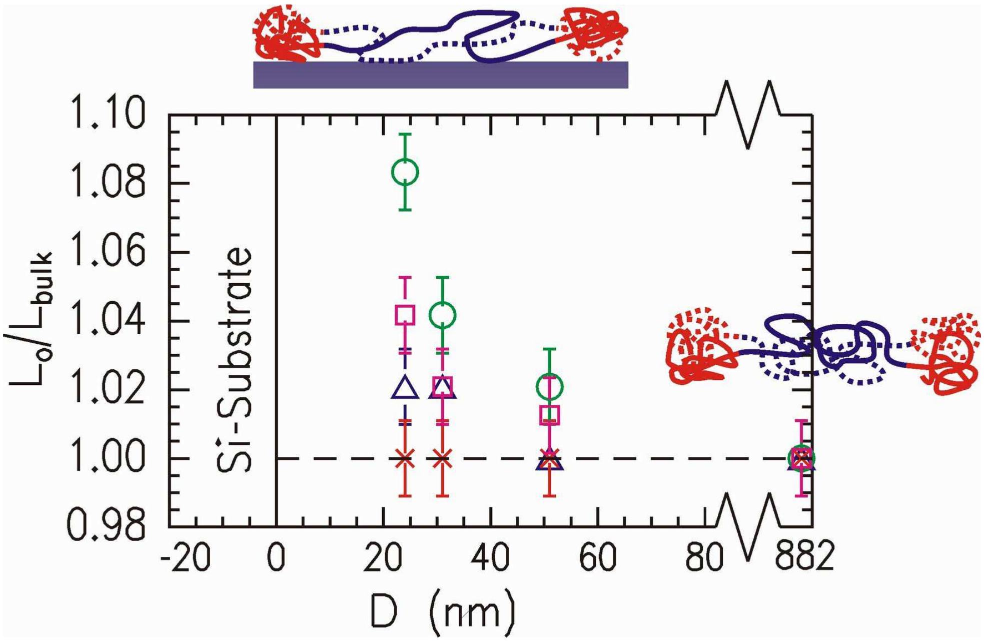

Figure 2.13:
Lamellar spacing L_o normalized by the bulk lamellar spacing L_{bulk} probed as a function of the scattering depth D of the signal, i.e. the depth over which the signal is probed with the evanescent wave, for the sample after acid-clean (triangles), base-clean (crosses), with deposited PDMS grains (squares) and the PS-brush surface (spheres). The dashed line shows the bulk lamellar spacing. The SiOx substrate is indicated.

For the investigated P(pMS-b-Sd8-b-pMS) films irrespective of the applied substrate surface treatment a perpendicular alignment of the lamellar at the interface was observed. So bending of the mid-block is avoided in any cases. In detail, bulk conformational properties of polymer chains are modified in contact with the interface due to competition between the loss of entropy at the interface and the gain of internal energy (see fig. 2.13) [4].

[1] Lin, J. S. Langmuir 1999, 15, 7947.

[2] Müller-Buschbaum, P.; Gutmann, J. S.; Stamm, M.; Phys. Chem. Chem. Phys. 1999, 1, 3857.

[3] Müller-Buschbaum, P. Euro. Phys. J. E 2003, 12, 443.

[4] Müller-Buschbaum, P.; Schulz, L.; Metwalli, E.; Moulin, J.-F.; Cubitt, R.; Langmuir 2008, 24, 7639.

2.8 The effect of heat treatment on the structure of block copolymer thin films

C. M. Papadakis, Z. Di, C. Darko, D. Posselt[1], D.-M. Smilgies[2], M.A. Singh[3]

[1] IMFUFA, Department of Science, Systems and Models, Roskilde University, Denmark
[2] Cornell High-Energy Synchrotron Source (CHESS), Cornell University, USA
[3] Department of Physics, Queen's University, Kingston, Ontario, Canada

Thin block copolymer films may show lateral structures on a sub-micrometer length scale, which are of interest for, among others, the nanopatterning of substrates. Thermal annealing has been reported to alter the surface structure of such films. Local undulations of interfaces, changes of the repeat distance, elastic deformation of the domains and other processes have been reported to occur at the surface of the polymer film [1].

We have focused on the influence of the annealing temperature on the structure of thin lamellar film with initially perpendicular lamellae. Poly(styrene-*b*-butadiene) (S-*b*-B) diblock copolymers were investigated, and the annealing temperatures were chosen below and above the glass transition temperature, T_g, of PS (100°C). We expected that annealing above T_g allows for long-range diffusion of the copolymers and thus more significant alterations of the lamellar structure than below. Grazing-incidence small-angle X-ray scattering (GISAXS) carried out at CHESS beamline D1 allowed us to investigate changes in the lateral correlation of the lamellae as well as to detect the influence of annealing on the surface roughness. A custom-made in-situ heating cell was used [2]. Atomic force microscopy (AFM) and X-ray reflectometry (XR) allowed us to monitor the film surfaces and the film thickness and roughness.

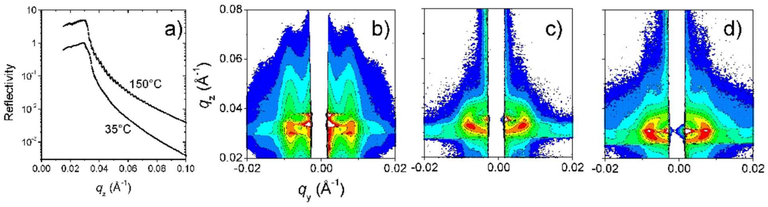

Figure 2.14:
In-situ XR (a) and in-situ GISAXS maps (b-d) from a thin lamellar P(S-*b*-B) film at 35°C (b), 150°C (c) and 45°C (d) Logarithmic intensity scales.

The XR curve of a film of thickness 305 nm shows no Kiessig fringes right after spin-coating (Fig. 2.14a), i.e. the thickness is inhomogeneous. At 150°C, a large number of Kiessig fringes appeared, i.e. the film surface becomes more flat upon thermal annealing. The GISAXS map at 35°C (Fig. 2.14b) shows straight diffuse Bragg rods (DBRs), revealing the perpendicular orientation of the lamellae [3]. Upon heating the sample to 150°C for 50 min, the straight DBRs transformed into a ring centered around the specularly reflected beam (Fig. 2.14c), i.e. the lamellae are tilted with a certain distribution of tilt angles. Upon cooling down the sample to 45 °C (Fig. 2.14d), the ring is preserved, and the straight DBRs partially reappear, i.e. a part of the lamellae regain their original perpendicular orientation.

A similar film (thickness 340 nm) was annealed at 60°C, i.e. below T_g of the PS block. The surface structure was nearly unaltered before and after the annealing and subsequent cooling down to room temperature (Fig. 2.15a,b). The GISAXS map before annealing reveals DBRs, confirming the perpendicular orientation (Fig. 2.15c). After annealing and cooling, the straight DBRs are preserved (Fig. 2.15d), i.e. the lamellar orientation is still mainly perpendicular, in contrast to the loss of orientation encountered when annealing at 150°C. The most striking change observed after annealing at 60°C are the intensity oscillations along q_z. We attribute them to the decreased roughness of the film surface achieved by thermal annealing.

We conclude that thermal annealing at 150°C results in a partial loss of the perpendicular orientation. In contrast, annealing at 60°C only results in flattening of the film surface and leaves the lamellar arrangement unaltered.

This project is funded by the Graduate School 'Materials Science of Complex Interfaces'.

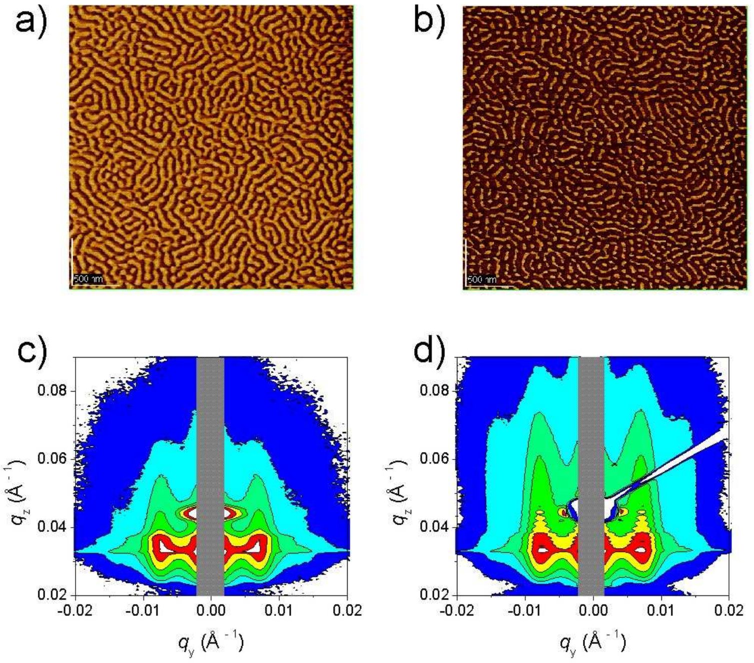

Figure 2.15:
AFM images of a thin lamellar P(S-*b*-B) film at room temperature (a) and after annealing at 60°C and subsequent cooling to room temperature (b). Image size 3 μm × 3 μm. (c.d) Corresponding GISAXS maps.

[1] L. Tsarkova et al., Langmuir **22**, 8089 (2006)

[2] M.N.Groves, M.A. Singh, et al., J. Appl. Crystallogr. **39** 120 (2006)

[3] D.-M. Smilgies, P. Busch, C.M. Papadakis, D. Posselt, Synchr. Rad. News **15**, 35 (2002). P. Busch, D. Posselt, D.-M. Smilgies, M. Rauscher, C.M. Papadakis, Macromolecules **40**, 630 (2007)

[4] P. Busch, M. Rauscher, D.-M. Smilgies, D. Posselt, C.M. Papadakis, J. Appl. Cryst. **39**, 433 (2006)

[5] R.J. Albalak, M.S. Capel, E.L. Thomas, Polymer **39**, 1647 (1998). M. Shibayama, T. Hashimoto, H. Kawai, Macromolecules **16**, 1434 (1983).

2.9 Structural instabilities in lamellar diblock copolymer thin films during solvent vapor uptake

C. M. Papadakis, Z. Di, D. Posselt[1], D.-M. Smilgies[2]

[1] IMFUFA, Department of Science, Systems and Models, Roskilde University, Denmark
[2] Cornell High-Energy Synchrotron Source (CHESS), Cornell University, USA

Thin block copolymer films are promising candidates for a variety of applications, such as the preparation of nanoporous films, nanostructured templates, photonic crystals and biosensors [1]. Long-range order can be achieved by thermal annealing, application of an electric field or solvent vapor treatment with subsequent drying. However, the molecular mechanisms and mesoscopic rearrangements involved in solvent annealing are still largely unexplored.

The thin film geometry allowed us to study the processes during vapor treatment in great detail [2] because the lamellae are macroscopically oriented. Using in-situ, real-time grazing-incidence small-angle X-ray scattering (GISAXS) with 2D detection, structural changes parallel to the lamellar interface can be distinguished from those along the film normal. We addressed the question how the swollen blocks are accommodated in the thin film geometry, where the lateral extension of the lamellar interfaces is very high.

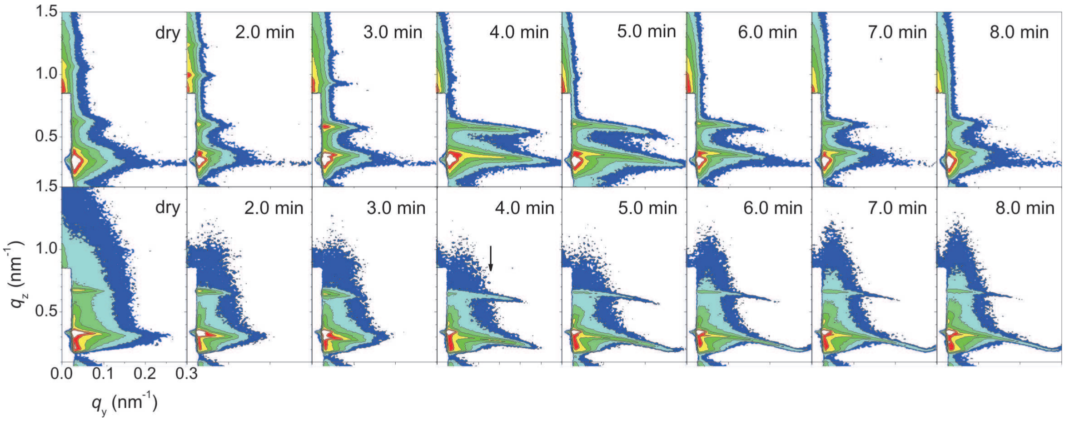

Figure 2.16:
(a) 2D GISAXS maps before and during vapor treatment. Upper row: thick film, lower row: thin film. Logarithmic intensity scale. The times after injection of toluene are indicated.

A symmetric poly(styrene-*b*-butadiene), P(S-*b*-B), diblock copolymer having a bulk lamellar thickness, $D_{\mathrm{lam}}^{\mathrm{bulk}} = 18.9$ nm was studied. Two thin films having thicknesses of 100 nm and 210 nm were investigated. GISAXS experiments were performed at CHESS beamline D1 using a vapor cell. Toluene, a good and close to non-selective solvent, was injected into a reservoir in the sample cell through a long Teflon capillary, and GISAXS images were taken subsequently every 10 s, while the film was immersed in saturated vapor. The lamellar thickness in the thin film geometry, $D_{\mathrm{lam}}^{\mathrm{film}}$, was determined using the distorted-wave Born approximation [3].

Before vapor treatment, the lamellae in both films were aligned parallel to the film surface, as revealed by the presence of diffuse Bragg sheets (DBSs) appearing along the film normal, q_z (Fig. 2.16). Representative GISAXS images of both films taken after injection of toluene into the cell are shown in Fig. 2.16. During the first 3 min of solvent vapor exposure, the DBSs moved downwards and became more intense. Then, they suddenly spread out along q_y and curved downwards. In addition, side peaks at finite q_y appeared next to the DBSs in this time regime. Then, the DBSs moved again towards larger q_z-values, their lateral width decreased, and the side peaks vanished. We thus witnessed complex re-ordering processes during exposure to saturated solvent vapor, and both films behaved very similarly.

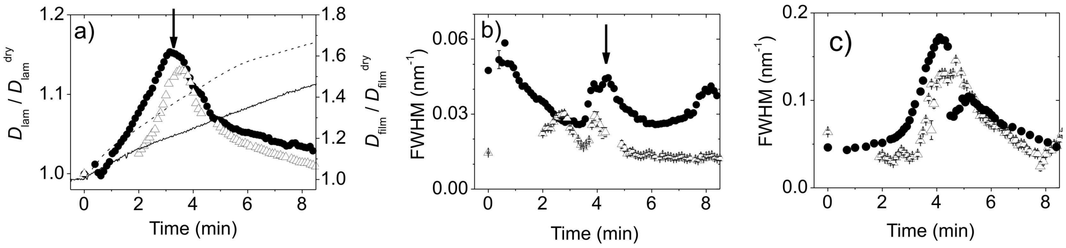

Figure 2.17:
(a) Lamellar thicknesses ((●) thick film, (△) thin film) and film thicknesses (full line: thick film, dashed line: thin film) of the two films, (b) FWHM of the DBS along q_z and (c) FWHM of the DBS along q_y.

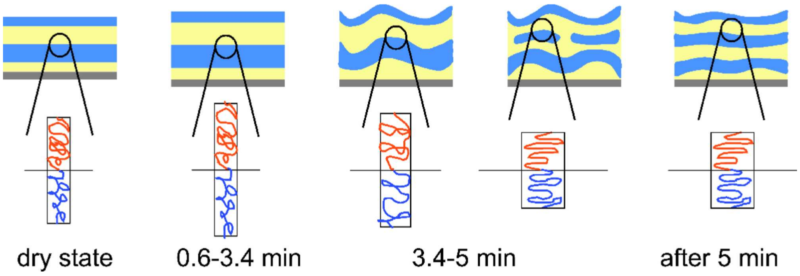

Figure 2.18:
Suggested scenario. The lamellar structure is depicted on top, the molecular conformation in the bottom.

An analysis of the DBS at $q_z = 0.6\ \mathrm{nm}^{-1}$ shows that $D_{\mathrm{lam}}^{\mathrm{film}}$ increased and reached maximum values (Fig. 2.17a). The situation then suddenly reversed, i.e. contrary to expectation, the lamellae became thinner again. D_{film} increases much more strongly than $D_{\mathrm{lam}}^{\mathrm{film}}$. The FWHMs of the DBS along q_z of both films reached a maximum 3-5 min after the injection (Fig. 2.17b). We ascribe the maximum to break-up and reorganization of the lamellar stack. The widening of the DBS along q_y (Fig. 2.17c) is due to an increase of the correlated roughness of the lamellar interfaces. The downward bend of the diffuse scattering maxima is attributed to thickness variations of the thin film with oppositely curved interfaces.

These processes are due to the tendency of the blocks to assume a more coiled state in the presence of solvent than in the dry state, Fig. 2.18 [4]. After uniaxial swelling due to the addition of solvent to the lamellae, the copolymers' chain conformation becomes more coiled, resulting in a higher demand of interfacial area per chain. Therefore, the lamellar interface first increases by roughening, and then by the creation of extra lamellae. This leads to a reorganization of the lamellar stack.

This project is funded by the Graduate School 'Materials Science of Complex Interfaces'.

[1] R.A. Segalman, Mat. Sci. Eng.: R: Reports **48**, 191 (2005)

[2] D.-M. Smilgies, P. Busch, C.M. Papadakis, D. Posselt, Synchr. Rad. News **15**, 35 (2002). C.M. Papadakis, Z. Di, D. Posselt, D.-M. Smilgies, Langmuir(Letters) **24**, 13815 (2008)

[3] P. Busch, M. Rauscher, D.-M. Smilgies, D. Posselt, C.M. Papadakis, J. Appl. Cryst. **39**, 433 (2006)

[4] R.J. Albalak, M.S. Capel, E.L. Thomas, Polymer **39**, 1647 (1998). M. Shibayama, T. Hashimoto, H. Kawai, Macromolecules **16**, 1434 (1983).

2.10 Structural changes of lamellar block copolymer thin films in solvent vapor

Z. Di, C. M. Papadakis, D. Posselt[1], D.-M. Smilgies[2], A. Timmann[3]

[1] IMFUFA, Department of Sciences, Roskilde University, Roskilde, Denmark
[2] Cornell High-Energy Synchrotron Source (CHESS), Cornell University, USA
[3] HASYLAB at DESY, Hamburg

Solvent annealing has recently emerged as a powerful alternative to thermal annealing of block copolymer (BCP) thin films. The solvent has a strong effect on the effective T_g (positive) and the Flory-Huggins segment-segment interaction parameter χ (negative) of the polymers and thus has an influence on the long-range order as well as the structure dimension. We have investigated the structural changes of thin films from lamellar poly(styrene-*b*-butadiene) (P(S-*b*-B)) diblock copolymers during treatment with saturated cyclohexane (CHX) vapor using in-situ, real-time grazing-incidence small-angle X-ray scattering (GISAXS). CHX is slightly selective for PB.

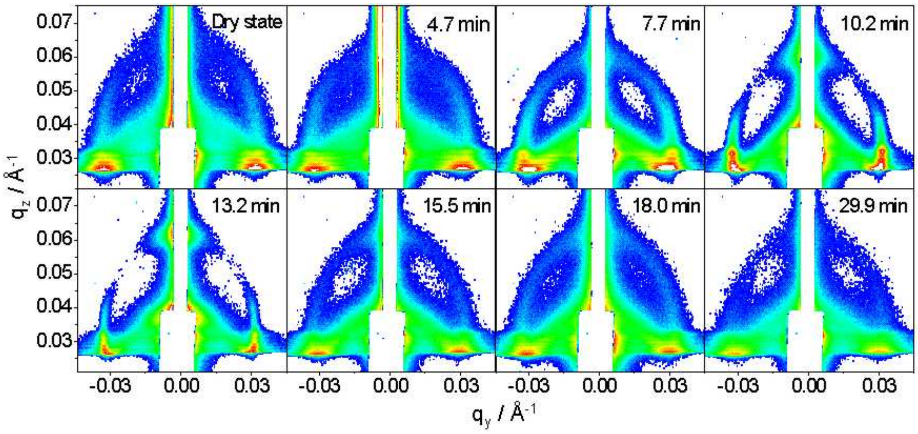

Figure 2.19: GISAXS images of the P(S-*b*-B) thin film during treatment with saturated CHX vapor for the times given in the figures.

Thin film of P(S-*b*-B) was prepared by spin coating from toluene onto a UV cleaned Si wafer. The symmetric BCP has a molar mass of 22 kg/mol. It is expected to form lamellae parallel to the film surface after thermal annealing [1]. However, the as-prepared sample shows a mixed lamellar orientation, as evident from the diffuse Debye-Scherrer ring in the GISAXS image (Fig. 2.19, dry state). When the film is subjected to saturated CHX vapor, the GISAXS images reveal two stages (Fig. 2.19): (i) During the first 13 min, the ring splits up into sharper diffuse Bragg rods and sheets, indicating the presence of perpendicular and parallel lamellae. (ii) The ring becomes more pronounced and broader again. Thus, a transient state is observed for the time range 10-13 min, characterized by a more well-defined lamellar orientation and an increased long-range order.

The thickness of the parallel lamellae, D_{lam}, is calculated from the position (projection to Z-axis) of Bragg sheets using the distorted-wave Born approximation [2]: Instead of simple swelling, D_{lam} shows complex behavior as a function of vapor treated time (Fig. 2.20a): after an incubation time of $\sim$3 min, strong swelling up to 14%, a plateau and a slow decrease to a value slightly larger (4%) than the one in dry state are observed. From the intensity oscillations of the diffuse Bragg rod (Fig. 2.20b), which are due to waveguide resonances inside the film, the film thickness, D_{film}, during vapor treatment can be deduced [3] (Fig. 2.20c). The film swells continuously until a degree of swelling of 90% is reached. Comparing with the final degree of swelling of D_{lam} (4%), it indicates the growth of additional parallel lamellae.

Therefore, three interesting effects have been identified during vapor treatment: (i) A transient state with improved long-range order. (ii) Complex behavior of D_{lam}. (iii) Growth of additional

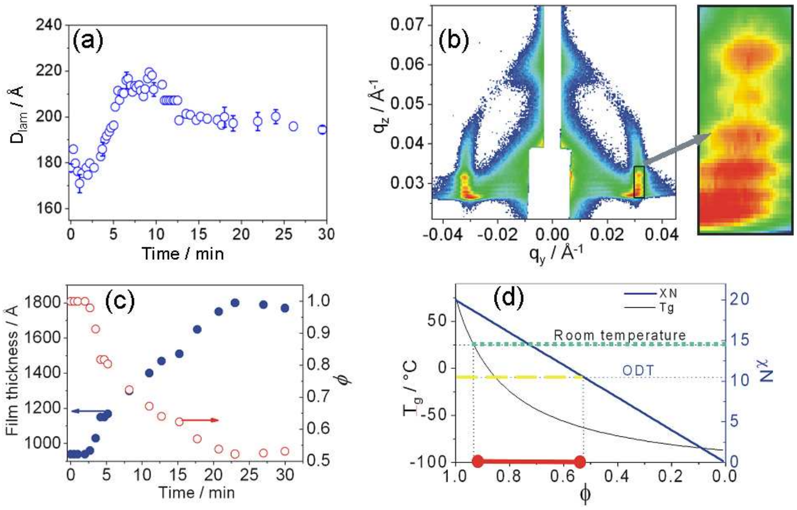

Figure 2.20:
(a) thickness of the parallel lamellae in the P(S-*b*-B) thin film during vapor treatment as deduced from the position of the diffuse Bragg sheets.(b) 2D GISAXS image taken during vapor treatment with a zoom of a Bragg rod. (c) film thickness as a function of treatment time (blue dots) and the resulting volume fraction of PS-PB (red circles) (d) the effective T_g (black thin) and χN (blue thick) as a function of volume fraction of polymer

parallel lamellae. Similar to thermal annealing, vapor treatment increases the polymer mobility, thus making equilibration of the film possible. The effective T_g of the polymer-solvent blend as a function of the actual polymer volume fraction, ϕ, can be estimated by the Kelley-Bueche equation [4]. In our system, ϕ can be calculated from the film thickness ($\phi = \frac{D_{film}^{dry}}{D_{film}^{swollen}}$) (Fig. 2.20c). When the effective T_g is well below room temperature (RT), the polymer mobility is strongly increased and equilibration is possible. In our system, since T_g of PB is very low (-89 °C), we only need to consider the effective T_g of PS. Fig. 2.20d shows that the effective T_g of PS drops below RT for $\phi < 0.9$ (the range marked by the turquoise dots). However, when too much solvent is incorporated, the lamellar structure may become disordered. The effective Flory-Huggins segment-segment interaction parameter between PS and PB is given by $\chi_{eff} = \phi\chi$ (Fig. 2.20d). The lamellar structure is preserved only when $\chi N > (\chi N)_{ODT}$, where ODT stands for order-to-disorder transition and N for the degree of polymerization. For a symmetric diblock copolymer χN=10.5. The lamellar structure is thus only preserved for $\phi > 0.5$ (the range marked by a yellow dashed line). In summary, only for $0.5 < \phi < 0.9$ (the range marked by a red dumbbell), a lamellar equilibrium state can be achieved. At dry state, in the sample studied by us, $\phi = 1$. ϕ decreases from 1 to 0.5, which may explain the existence of the transient state with better defined lamellar orientation. Meanwhile, the changes of the mobility and the interaction between the two blocks have a complex influence on D_{lam}. At first, as long as $T_g > RT$, the polymer chains are immobile, and the lamellae swell following $D_{lam} \propto D_{film} \propto \phi^{-1}$. After additional CHX uptake, $T_g \ll RT$, i.e. the chains become mobile and a more-well defined lamellar orientation is established. As a consequence of the reduction of χ_{eff}, the polymer chains tend to become more coiled [5,6], which results in a decrease of D_{lam}. Because of volume conservation, the increase of D_{film} and the decrease of D_{lam} lead to the growth of additional parallel lamellae, i.e. a major reconstruction of the lamellar stack.

[1] Busch, P.; Posselt, D.; Smilgies, D.-M.; Papadakis, C.M. et al., *Macromolecules* **2003**, 36, 8717 and **2007**, 40, 630.

[2] Busch, P.; Rauscher, M.; Smilgies, D.-M.; Posselt, D.; Papadakis, C. M., *J. Appl. Cryst.* **2006**, 39, 433.

[3] Feng, Y. P.; Sinha, S. K. et al., *Phys. Rev. Lett.* **1993**, 71, 537.

[4] Kelley, F. N.; Bueche, F., *J. Polymer Sci.* **1961**, 50, 549.

[5] Noolandi, J.; Hong, K.-M., *Ferroelectrics* **1980**, 30, 117.

[6] Shibayama, M.; Hashimoto, T., et al., *Macromolecules* **1983**, 16, 1427.

2.11 Creation of lateral structures in diblock copolymer thin films during vapor uptake and subsequent drying

C.M. Papadakis, P. Černoch[1], P. Štěpánek[1], C. Darko, E. Metwalli, D.-M. Smilgies[2], S.V. Roth[3]

[1] Institute of Macromolecular Chemistry, Academy of Sciences of the Czech Republic, Prague
[2] Cornell High-Energy Synchrotron Source (CHESS), Cornell University, USA
[3] HASYLAB at DESY, Hamburg

Laterally structured block copolymer thin films are promising candidates for a variety of applications, such as the preparation of nanostructured sensors [1]. Solvent annealing offers a simple and flexible method with a potentially high degree of controllability through careful choice of solvent [2]. For thin films of poly(4-octylstyrene-*b*-butylmethacrylate) (P(OS-*b*-BMA)) diblock copolymers, it has been observed that lateral structures are obtained by treatment of a spin-coated film with hexane vapor and subsequent drying [3]. We have followed the processes going on during treatment with cyclohexane (CHX) and subsequent drying using in-situ, real-time grazing-incidence small-angle X-ray scattering (GISAXS) and X-ray reflectometry (XR). In this way, the lamellar orientation, the lamellar thickness, the film thickness and the surface roughness could be monitored. It was found that the treatment with CHX results in the perpendicular lamellar orientation which is stable upon subsequent drying.

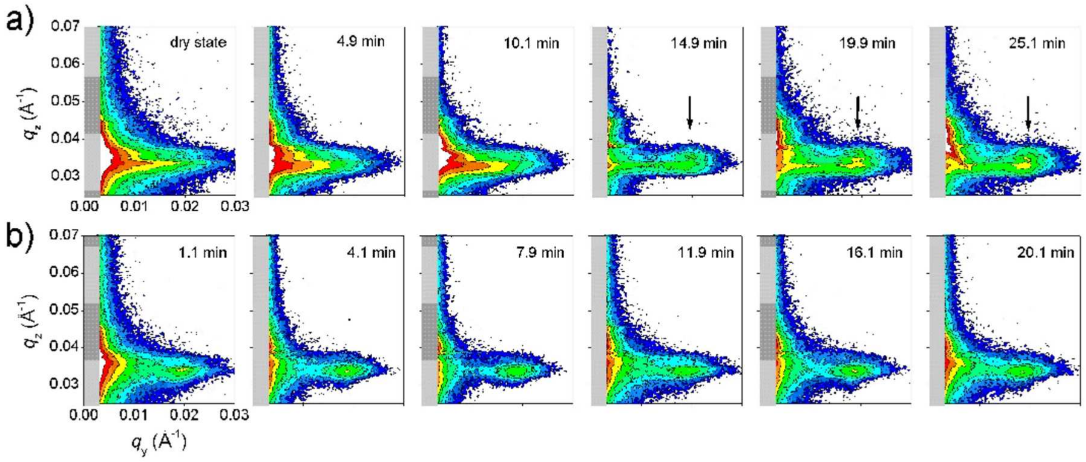

Figure 2.21:
GISAXS images of a thin film of (P(OS-*b*-BMA)) diblock copolymers during treatment with saturated CHX vapor (a) and during drying (b). The times after injection of liquid CHX are indicated. The arrows mark the intensity maximum.

The polymer under study has an overall molar mass of 35 600 g/mol and a weight fraction of POS of 62 %. In the bulk, it forms the lamellar morphology with a lamellar thickness of 260 Å [3]. The film was prepared by spin-coating. The film thickness was 373 Å with a surface roughness of 13 Å. GISAXS experiments were performed at CHESS beamline D1 with measuring times of 3 s. Liquid CHX was injected into a reservoir in the sample cell which was at ambient pressure. Drying of the sample was carried out by lifting the lid of the sample cell.

The changes during exposure to saturated CHX vapor are evident from the time series of GISAXS images shown in Fig. 2.21a. After 12 min, an intensity maximum, presumably due to perpendicular lamellae, can be discerned which moves towards higher q_y-values until its position stays constant after 15.4 min. The peak becomes more intense with time, i.e. the domains consisting of perpendicular lamellae grow. The lamellar thickness in the swollen state amounts to 321 ± 1 Å (Fig. 2.22a), thus a factor of 1.2 higher than in the dry, bulk state. The film thickness has nearly doubled to 714 Å, and the surface roughness has decreased to 8 Å.

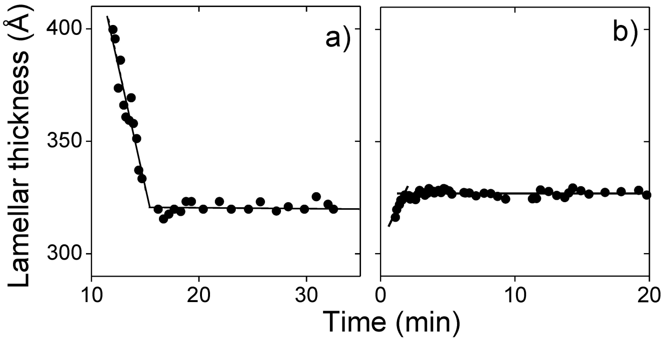

Figure 2.22:
Lamellar thickness deduced from the intensity maximum during vapor treatment with CHX (a) and during drying (b).

To characterize the stability of the such obtained laterally structured thin film morphology upon drying, we followed the structural changes during drying as well. The intensity maximum persists during drying (Fig. 2.21b), i.e. the perpendicular lamellar orientation is stable. The lamellar thickness increases immediately and reaches a constant value of 327 ± 2 Å after 1.8 min (Fig. 2.22b), thus the dry value from the bulk is not recovered. The film thickness has decreased to 389 Å with a surface roughness of 7 Å, i.e. the initial film thickness is nearly recovered, but the surface roughness is as low as in the vapor.

We conclude that the the P(OS-*b*-BMA) / CHX system allows the creation of thin films with perpendicular lamellae which are stable upon drying. The uptake of CHX allows the glassy PBMA component to become mobile as well. In this way, large-scale restructuring becomes possible.

This project is funded by the Graduate School 'Materials Science of Complex Interfaces'.

[1] Y.S. Jung et al., Nano Letter **8**, 3776 (2008)

[2] C.M. Papadakis, Z. Di, D. Posselt, D. Smilgies, Langmuir **24**, 13815 (2008).

[3] P. Černoch et al., Eur. Polym. J. **43**, 1144 (2007).

2.12 Multiscale study of crystallization in diblock copolymer thin films at different supercooling

C.M. Papadakis, C. Darko, E. Metwalli, I. Botiz[1], G. Reiter[1], D.W. Breiby[2], J.W. Andreasen[3], S.V. Roth[4], D.-M. Smilgies[5]

[1] Institut de Chimie de Surfaces et Interfaces, CNRS-UHA, Mulhouse, France
[2] Department of Physics, Norwegian University of Science and Technology, Trondheim
[3] Risø National Laboratory for Sustainable Energy, Technical University of Denmark, Roskilde
[4] HASYLAB at DESY, Hamburg
[5] Cornell High-Energy Synchrotron Source (CHESS), Cornell University, USA

Polymer crystallization is a fascinating example of structure formation by molecular self-assembly featuring the interplay of different length and time scales. Polymer crystallization involves both the diffusion of amorphous chains towards the growth front and their folding into regular structures. Complex processes at the growth front have been the subject of current discussion, such as the initial formation of small crystalline grains which eventually fuse to form a lamella [1]. However, it is still not clear if an orientational correlation exists between chain stems of different grains. In thin film geometry, lamellar structures align parallel to the substrate surface.

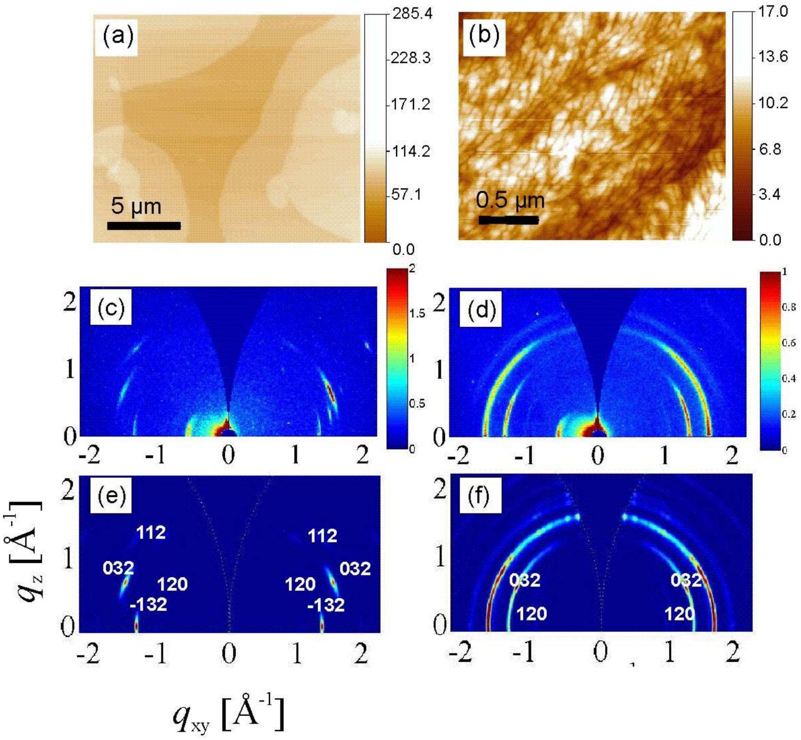

Figure 2.23:
AFM images of PS-*b*-PEO thin films crystallized at 50°C (a) and at 25°C (b). (c,d) Corresponding GIWAXS maps. (e,f) Simulated GIWAXS maps for the perpendicular (e) and the tilted orientation (f) of the PEO chain stems.

We have investigated structures resulting from crystallization of symmetric polystyrene-*b*-poly(ethylene oxide) (PS-*b*-PEO) diblock copolymers in thin film geometry [2]. Short chain lengths were chosen for both blocks (molar mass 3000 g/mol) allowing to distinguish between different folding states of the PEO block. A very low order-to-disorder transition (ODT) temperature is estimated for an amorphous block copolymer (-90°C), thus far below the crystallization temperatures used, i.e. the crystallization is unconfined. Thin films were prepared by spin-coating, heating above the melting point of PEO and fast cooling to the crystallization temperature, T_x. Strong and weak supercooling were compared. We combined optical microscopy, AFM, grazing-incidence small- and wide-angle scattering (GISAXS, GIWAXS) to determine the orientation of the crystalline PEO blocks within the films.

The surface texture of films crystallized at 25°C and at 50°C are very different (Fig. 2.23a,b). Whereas at 50°C, terraces are observed, at $T_x = 25°\text{C}$, a rough surface consisting of small objects is observed, which we attribute to individual crystalline PEO grains which formed at the advancing growth front. The growth rates at strong supercooling are three orders of magnitude higher than at low supercooling. Using GISAXS, we found that the repeat distance, i.e. the thickness of a PS-*b*-PEO bilayer, decreases with decreasing T_x, and is only at $T_x = 50°\text{C}$ in accordance with once-folded, PEO blocks being perpendicular to the lamellar interface. GIWAXS (Fig. 2.23c,d) together with simulated GIWAXS maps of the PEO crystals (Fig. 2.23e,f) confirmed that the PEO chain stems are tilted at strong supercooling with a wide distribution of tilt angles.

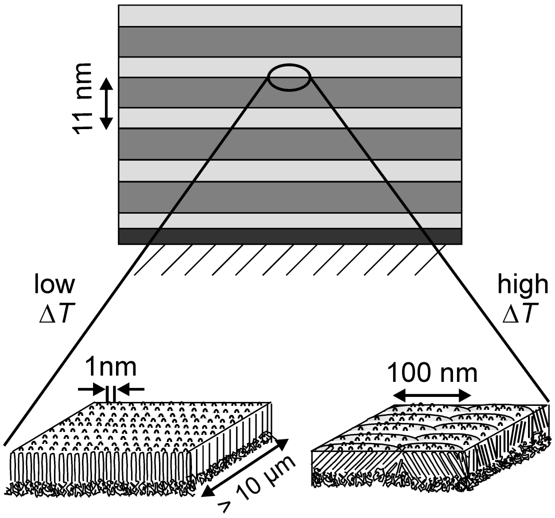

Figure 2.24:
Schematics of the structures of the films crystallized at 50°C (a) and at 25°C (b). Approximate length scales are indicated.

We conclude that each of the grains observed in the AFM image at $T_x = 25°\text{C}$ consists of chains with a specific tilt angle (Fig. 2.24). The tilt angle varies from grain to grain. We suggest that the crystalline domains, which grow at a constant growth rate from a single nucleation point, are not built up from a large lamella with uniformly oriented crystalline chains. A possible reason for this is repeated nucleation events at the growth front. The grain size increases with decreasing supercooling. Our work shows that only a detailed multiscale structural analysis can explain the observed surface morphologies and we related them to different mechanisms of crystal growth.

This project is funded by DFG (Pa771/3) and the Incentive Fund for Research Collaborations between TU München and the Danish Technical University.

[1] T. Hugel et al., Acta Polymerica **50**, 214 (1999). L. Gránásy et al., Nature Materials **3**, 645 (2004).

[2] C. Darko, E. Metwalli, I. Botiz, G. Reiter, D.W. Breiby, J.W. Andreasen, S.V. Roth, D.-M. Smilgies, C.M. Papadakis, Phys. Rev. E, accepted.

2.13 Break-away crystallization in thin films of cylinder-forming PI-*b*-PEO diblock copolymers

C.M. Papadakis, C. Darko, K. Troll, Z. Di, D.-M. Smilgies[1], A. Timmann[2], S. Förster[3]

[1] Cornell High-Energy Synchrotron Source (CHESS), Cornell University, USA

[2] HASYLAB at DESY, Hamburg

[3] Department Chemie, Universität Hamburg

In thin films of diblock copolymers with one crystallizing block, crystallization may be confined by the microphase-separated morphology or unconfined in the disordered state [1]. In bulk studies of the hexagonal cylindrical phase, crystallization of the block forming the cylinders was observed to destroy the microphase-separated hexagonal structure and to transform it into crystalline lamellae within an amorphous matrix [2]. The thin film geometry offers the possibility to macroscopically align the cylinders.

We have investigated the long-term behavior of a thin film of a low molar mass, cylinder-forming poly(isoprene-*b*-ethyleneoxide) (PI-*b*-PEO) (block molar masses 2100 and 1100 g/mol) diblock copolymer. A thin film was prepared by spin-coating from toluene solution onto Si wafers. The film thickness is ~ 140 nm. The samples were annealed at 62°C for a few minutes, i.e. above the melting point of PEO, and were then quenched to room temperature (RT). The surface morphology was monitored using optical microscopy (OM) and atomic force microscopy (AFM), whereas the inner film structure was investigated using grazing-incidence small- and wide-angle X-ray scattering (GISAXS, GIWAXS) at beamlines BW4 and BW2 at HASYLAB, DESY.

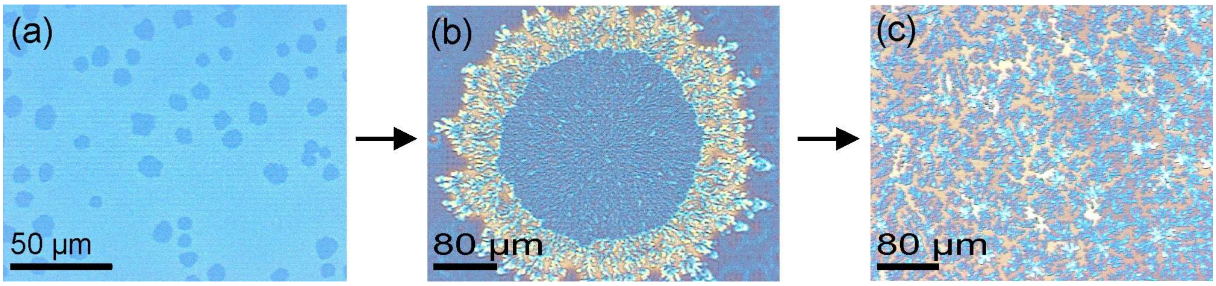

Figure 2.25:
Optical micrographs of a PI-*b*-PEO thin film right after quenching (a), after 41 days at RT (b), and after 148 days at RT (c). The lighter, the higher the film thickness.

Right after quenching to RT, the film surface was flat with large terraces (Fig. 2.25a), as expected for lying cylinders, which were revealed using AFM. Only after 41 days at RT, PEO crystals of circular shape with a grainy texture were observed (Fig. 2.25b), which continued growing until the entire film area was crystalline after 148 days at RT with a terraced surface morphology (Fig. 2.25c).

These changes of the surface morphology are due to the restructuring of the morphology inside the thin film. The buried mesosopic structure changed significantly with time. The hexagonal cylindrical structure due to microphase separation is conserved when cooling from the molten state of PEO to RT (Fig. 2.26a). The repeat distance of the hexagonal lattice is 10.0 ± 0.5 nm. Within 148 days at RT, the hexagonal morphology transforms into a weakly ordered layered structure with a similar repeat distance (9.3 ± 0.3 nm, Fig. 2.26b). The crystallization of PEO within 148 days is reflected in the presence of the (120) Bragg reflection in the GIWAXS intensity (Fig. 2.26c). The PEO chain stems are thus parallel to the film normal.

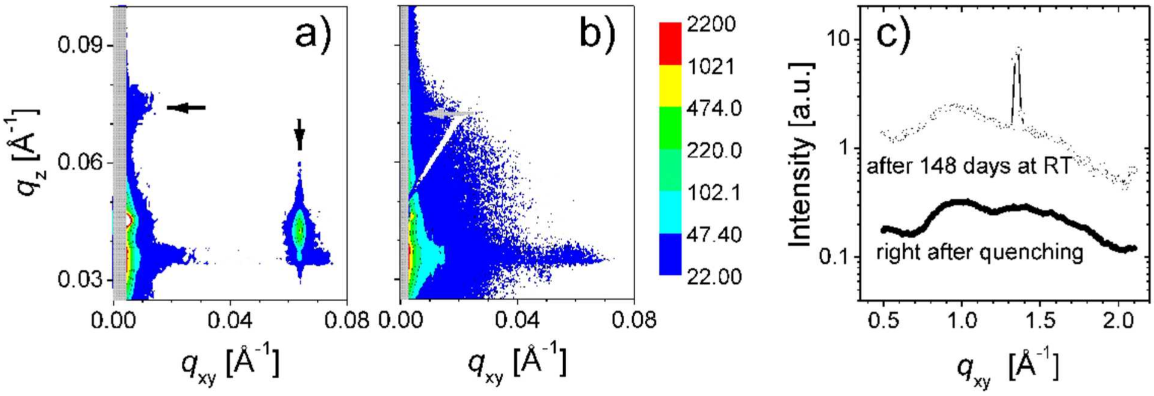

Figure 2.26:
2D GISAXS images of a PI-*b*-PEO thin film right after cooling to RT (a) and after 148 days at RT (b). The arrows indicate the diffuse Bragg reflections. (c) GIWAXS intensity profiles of the same films. The lines are guides to the eye.

In summary, we have observed very slow break-away crystallization in thin films from a low molar mass, cylinder-forming PI-*b*-PEO diblock copolymer. The crystallization of PEO in cylinders immersed in a PI matrix results in the destruction of the cylinders and the formation of crystalline PEO lamellae which are separated by PI and which are parallel to the substrate plane. In the resulting crystalline lamellae, the PEO chain stems are parallel to the film normal.

This work was financially supported by DFG (Pa771/3) and by the Incentive Fund for Research Collaborations between TU München and the Danish Technical University.

[1] A.J. Ryan et al., Macromolecules **28**, 3860 (1995).

[2] D.J. Quiram et al., Macromolecules **31**, 4891 (1998).

3 Polymer films for application in photovoltaics

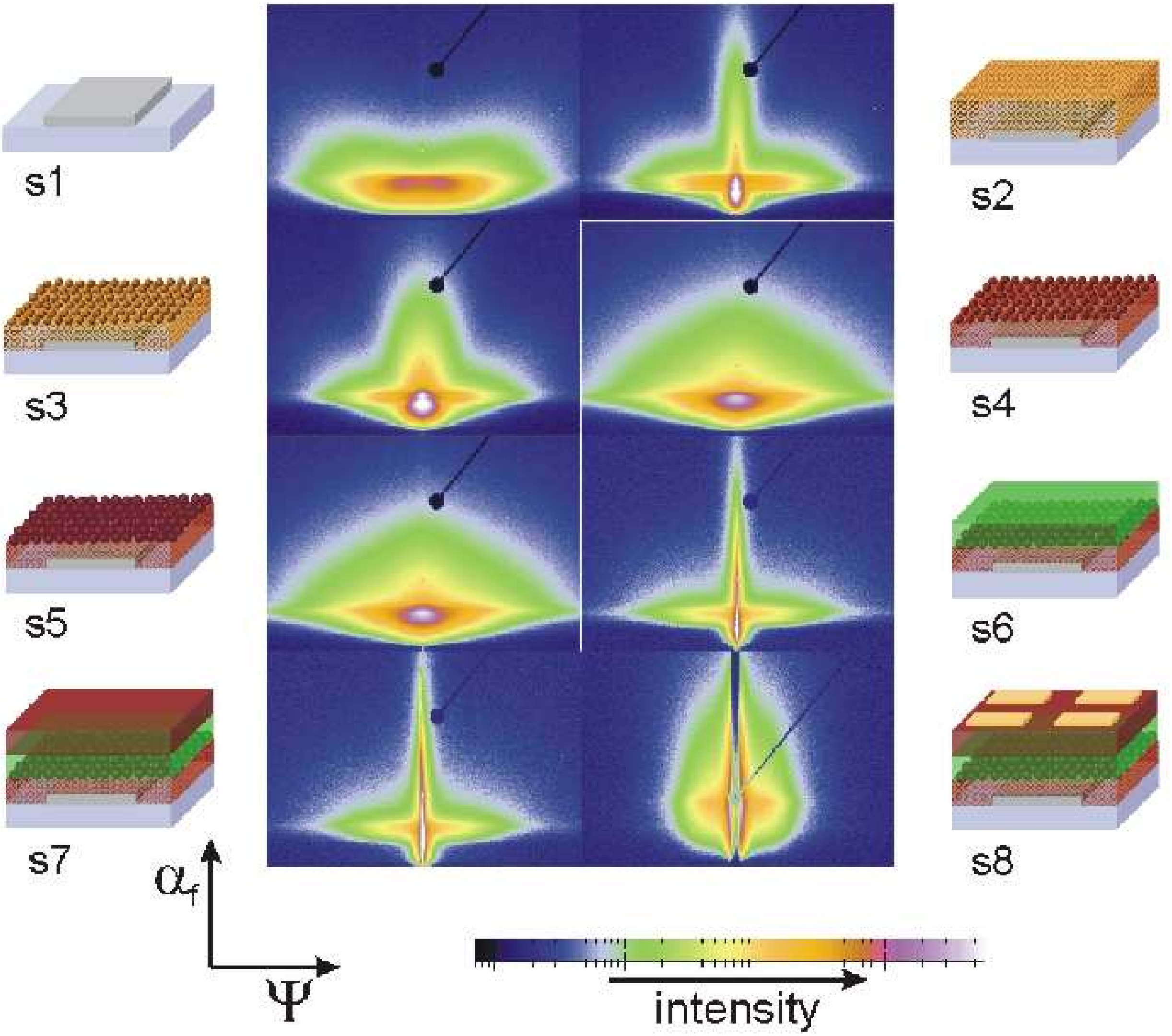

3.1 Structure control of conjugated block copolymers via adding a homopolymer

M. A. Ruderer, R. Cubitt[1], P. Müller-Buschbaum

[1] ILL, Grenoble, France

Conjugated polymers have shown to be interesting candidates for organic photovoltaics due to their high absorption coefficient, mechanical flexibility, easy processability and low cost. Furthermore the possibility to chemically tune the properties of the polymers, like conductivity, absorption range, solubility etc., makes a broad application feasible. In contrast to inorganic semiconductors, conjugated polymers have a higher exciton binding energy in the range of 1 eV which is much above room temperature. Therefore an efficient charge carrier separation can just occur at the interface of two polymer phases with different band structures which makes an active layer of a combination of two different photoactive polymers necessary. In addition the short exciton life time and consequently its short diffusion length, in the range of a few 10 nm, constrains the morphology of the active layer, i.e. the structure length of the phase domains has to be in the range of the exciton diffusion length. As in a layered system the total film thickness is limited by the mentioned conditions and consequently the absorption is low a bulk heterojunction is typically used as the active layer. [1]

The main approach for such systems is the blending of two conjugated polymers. Due to changes of the molecular composition, blending ratio, solvent, pre- and post treatment of the devices the morphology of the polymer blend is optimized. Nevertheless polymer blends tend to phase separate in the range of hundred nanometers instead of the exciton diffusion length to minimize the free energy of the system [2]. To overcome this problem one promising approach is to use conjugated block copolymers. Due to the covalent bond of two polymers micro-phase separation occurs and nanostructures in the desired range are generated.

The structure of block copolymers is defined by the ratio of the two blocks. To adapt the morphology to match the desired spatial dimensions via the synthesis of block copolymers with different block lengths is therefore a tedious work. Instead of changing the composition of the block copolymer via synthesis, an alternative approach is offered by blending the conducting block copolymer with a homopolymer which is equal to one of the blocks to adapt the morphology and match the desired spatial dimensions [3, 4].

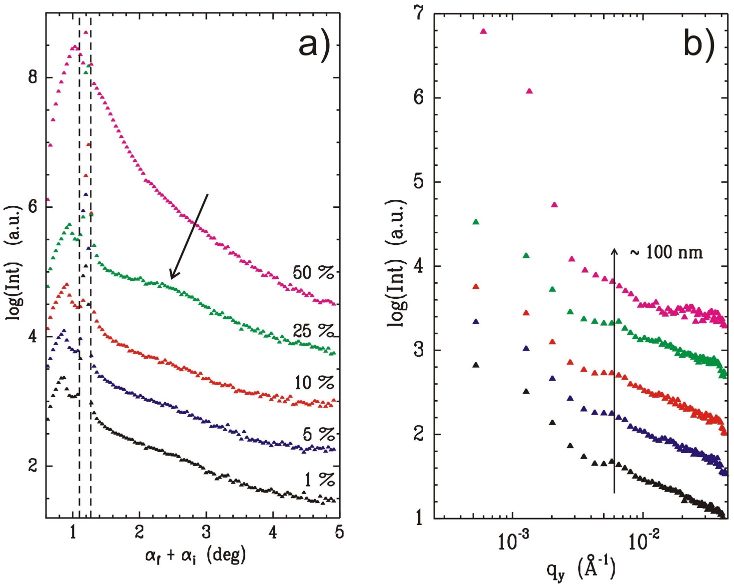

Figure 3.1:
a) Detector cuts of P(S-b-PP) with different ratios of dPS increasing from bottom to top. The dashed lines mark the specular peak. The arrow highlights the maximum corresponding to a vertical length of 16 nm. b) Out-of plane cuts of P(S-b-PP) with different ratios of dPS increasing from bottom to top. The arrow marks a structure length of around 100 nm. All curves are shifted for clarity.

A diblock copolymer with a rigid conjugated block and a conventional coiled block is focused. The rigid block is made of poly(p-phenylene) (PPP) and the coiled block of polystyrene (PS).

Due to the immiscibility of both blocks and the ratio $f_{PPP} = 0.41$ the block copolymer forms lamellae. By adding the homopolymer polystyrene the PS-block swells and the structure is modified. A series of five samples with different homopolymer ratios from 1 v% to 50 v% and a film thickness of about 200 nm was prepared on Si-substrates via spin coating technique.
The inner film structure was determined with grazing incidence small angle neutron scattering (GISANS) [5]. Therefore fully deuterated polystyrene (dPS) was used as the added homopolymer to increase the scattering contrast. As conjugated polymers are sensitive to any high energy radiation, e.g. X-rays, neutrons are used for scattering measurements. Consequently, the scattering probe does not alter the molecular structure or degrade the photoactive film.
Figure 3.1a shows the detector cuts of the films contating P(S-b-PP) and dPS. The dPS ratio is increasing from bottom to top. On the left side of the specular peak (dashed lines) the Yoneda peak is detected. With increasing dPS ratio it is shifted to higher angels respectively higher q_z as a direct evidence for the dPS ratio. At higher angles one modulation in the curve, highlighted by an arrow, can be distinguished. It is most pronounced for a dPS ratio of 25 v% (green curve) and corresponds to a vertical length of about 16 nm which is a sign of an enrichment layer with this thickness.
The out-of plane cuts (Figure 3.1b) give information about lateral structures in the polymer films. Surprisingly, a structure size of about 100 nm is found for every dPS ratio (arrow in figure 3.1b). This would mean, that the block copolymer micro-phase separation structure is not swollen by the incorporation of the homopolymer and the homopolymer has to be located in enrichment layers at the interfaces.

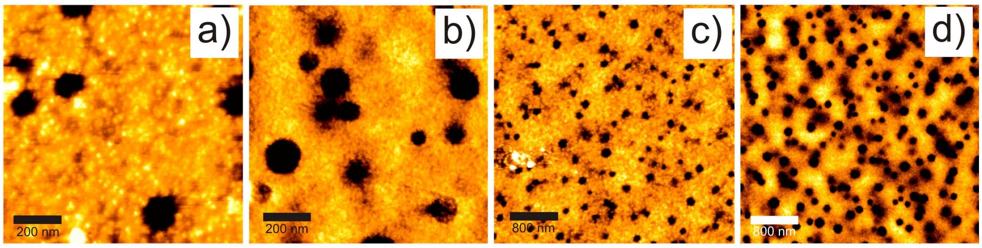

Figure 3.2:
AFM images of P(S-b-PP) + dPS films with different ratios of dPS: a) and c) have a ratio of dPS of 25 v% and b) and d) of 1 v%. The images a) and b) have a scan size of 1 μm x 1 μm and c) and d) of 4 μm x 4 μm. The color code is adjusted independently for each image.

The topography was detected by atomic force microscopy (AFM). In figure 3.2 the AFM images of two samples, dPS ratio of 1 v% (b,d) and 25 v% (a,c) are shown. For both samples holes (dark area) with a depth of around 15 nm are found which is consistent with the results of the GISANS measurements for the 25 v% sample. The mean size and the density of the holes is higher for the 1 v% sample. But for neither of both samples a significant ordering of the holes was determined. Consequently, the prominent lateral length scale of 100 nm found in the GISANS measurements has to correspond to an inner film structure. In addition to the holes the 25 v% sample shows spherical objects in the range of 10 nm on the surface (see figure 3.2a). The surface between the holes of the 1 v% sample seems to be smooth (see figure 3.2b).

[1] S. Günes et al., Chem. Rev. **107**, 1324 (2007)

[2] M. A. Ruderer et al., ChemPhysChem **10**, 664 (2009)

[3] P. L. Soo et al., J. Polym. Sci., Part B: Polym. Phys. **36**, 923 (2004)

[4] J. Perlich et al., Langmuir **23**, 10299 (2007)

[5] P. Müller-Buschbaum et al., Langmuir **22**, 9295 (2006)

3.2 Surface and structure analysis of thin polymer blend films based on MEH-PPV and PVK

R. Meier, P. Müller-Buschbaum

We report structural and surface analysis of photoactive thin polymer films based on blends of novel conducting materials. Since the discovery of the conducting properties of polymers, organic thin films have become of great interest for versatile applications such as organic thin film transistors, light emitting diodes or solar cells. In our study films based on MEH-PPV (poly[2-methoxy-5-(2-ethylhexyloxy)-1,4-phenylenevinylene]) and PVK (poly N-vinylcarbazole) are investigated. It has been shown that, due its charge transfer properties, MEH-PPV is a very promising candidate for applications [1].

Especially for polymer light emitting diodes (PLEDs) an interpenetrated network of conjugated polymer MEH-PPV and PVK can emit white light in combination with a an additional polymer [2]. Therefore the phase separation of the different polymers is crucial.

For applications polymers have the advantage to be solution processable. For MEH-PPV and PVK the solvent of choice is toluene. The polymers are blended in solution at a constant volume ratio of 3 parts MEH-PPV to 2 parts PVK. The blended solution is spin-coated on acidic pre-cleaned silicon and glass substrates. In order to investigate the dependence of the typical structure size in thin films on the polymer concentration a series of different concentrations is studied: (a) 3 parts of $1g/l$ MEH-PPV in tol. : 2 parts of $3g/l$ PVK in tol. ; (b) $1.5g/l$ MEH-PPV in tol. : $4.5g/l$ PVK in tol. ; (c) $2g/l$ MEH-PPV in tol. : $6g/l$ PVK in tol. ; (d) $3g/l$ MEH-PPV in tol. : $9g/l$ PVK in tol.

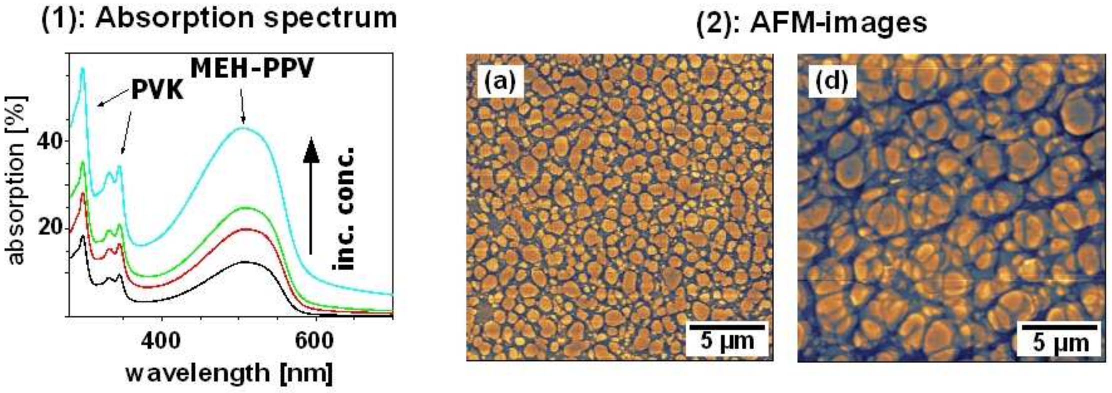

Figure 3.3:
(1) UV-Vis absorption spectra for the different concentrations and (2) AFM topography images for sample (a) and (d) ($\sigma_{P_V}(a) = 10nm$ and $\sigma_{P_V}(d) \approx 30nm$).

The energy of the HOMO (highest occupied molecular orbital) of the hole conducting MEH-PPV is -5.1 eV and of the LUMO (lowest unoccupied molecular orbital) is -2.8 eV. Respectively for PVK it is $-6eV$ and $-2.3eV$. Therefore the band gap energies can be calculated to be $E_{g,MEH-PPV} = 2.3$ eV and $E_{g,PVK} = 3.7$ eV. The UV-Vis spectra in Fig. 3.3 also show the good absorption abilities of MEH-PPV for red light and of PVK in the UV region. It can be seen that the absorption strongly depends on the film thickness. These were determined using the ellipsometer from the newly installed SPEM (*Nanofilm*). Therefore angle-of-incidence measurements were performed and the characteristic $\Delta-$ and $\Psi-$values were obtained. A single-layer-model for fixed refractive and exctinction coefficients was used to determine the thickness d of the polymer films: $d(a) = 16.1 \pm 3.3$ nm, $d(b) = 25.1 \pm 2.6$ nm, $d(c) = 35.6 \pm 2.9$ nm and $d(d) = 60.8 \pm 2.2$ nm.

The atomic force microscope (AFM) from the SPEM was used to characterize the surface of the polymer films. In Fig. 3.3 two AFM topography images of films with the lowest and highest polymer concentrations are shown (samples (a) and (d)). The films show phase separation at the micro scale, which is very well tuneable via the polymer concentrations in their solution and hence the thickness of the films. From the images a typical grain size for the different films can be determined by taking into account multiple line cuts: $\Lambda(a) = 0.8-1.0\mu m$, $\Lambda(b) = 1.0-1.3\mu m$, $\Lambda(c) = 1.6-2.2\mu m$ and $\Lambda(d) \approx 2.0-3.0\mu m$.

The inner film structure is analysed with grazing incidence ultra small angle x-ray scattering (GIUSAXS) measurements. These measurements were performed at the BW4 at HASYLAB and are very well suited to detect the large structure features of the MEH-PPV-PVK-films. Fig. 3.4 shows the two dimensional images of the MAR-CCD detector and the out of plane cuts taken at the position of the Yoneda peak with maximum intensity.

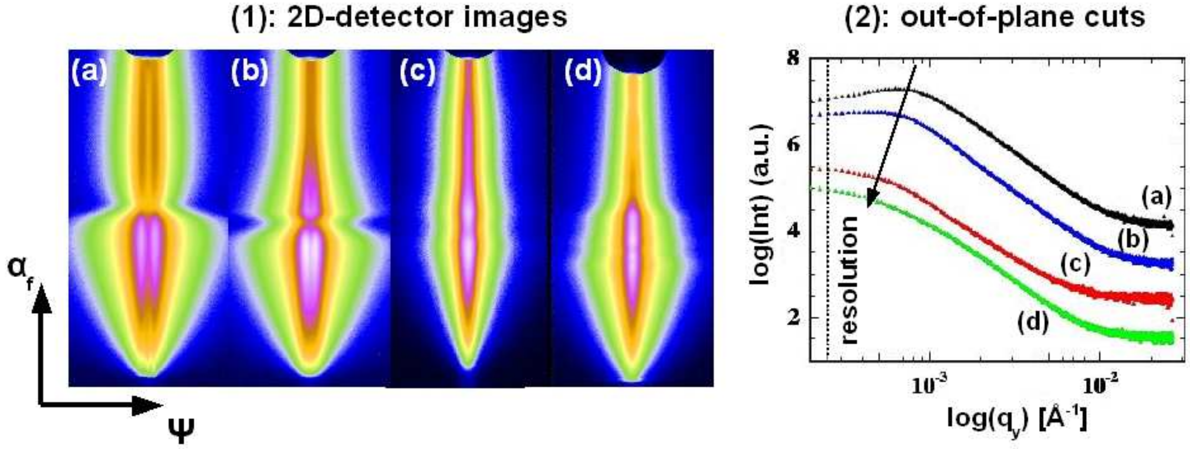

Figure 3.4: (1) 2d-detector images and (2) out-of-plane cuts for samples (a) to (d)

The 2D-images show a splitting of the Yoneda peak for the samples (a) and (b). For the samples with higher polymer concentration the typical structure size is enlarged and not so defined. Hence instead of two separated Yoneda peaks a slight shoulder is detectable. The structure factors from the out-of-plane cuts for sample (a) and (b) are in good agreement with the surface images: $\Lambda(a) = 0.88\mu m$ and $\Lambda(b) = 1.05\mu m$. For samples (c) and (d) the out-of-plane cuts have to be fitted.

It could be shown that the structure size of the thin films based on a polymer blend of MEH-PPV and PVK can be tuned via the polymer concentration in solution. The electrical properties for the different films will be determined in ongoing experiments. So far the poor surface conductivity could not be measured. Hence as a following step the conductivity and photoconductivity will be measured through the film using conducting FTO glass substrates. The analysis of the inner film structure will be complemented by fitting the cuts and the 2D-detector images with the simulation software IsGISAXS.

[1] R. Meier et. al., Physical Review B 77, 195314, 2008

[2] S. Yang et. al., Journal of Electronic Materials, Vol. 37, No. 11, 2008

3.3 SLD determination of conducting polymers based on PPV derivates

R. Meier, M. A. Ruderer, G. Kaune, J. Perlich, R. Georgii[1], P. Müller-Buschbaum

[1] FRM-II, Garching, Germany

Due to their photoactive properties conducting polymers show bright prospects for application in organic solar cells or organic light emitting diodes and therefore have been in focus of world-wide soft matter research over the last years [1]. Due to their chemical structure they are sensitive to high energy radiation. Hence, neutron scattering seems an appropriate non-destructive way to study conducting polymer films, however, the number of neutron scattering experiments which had been performed so far are extremely limited. We report first neutron scattering length density measurements on thin conducting polymer films focusing on different novel p-phenylene vinylene (PPV) derivates, such as MEH- , MDMO- , M3EH- , and MEH-CN-PPV.

For sample preparation the conducting polymers were dissolved in organic solvents (e.g. toluene, chloroform) and spin-coated on glass substrates. The glass substrates were cleaned in acidic bath before use. We measured the critical edge for these materials using neutron reflectivity (NR). A typical neutron reflectivity curve including its critical edge is shown in Fig. 3.5. The experiments were performed at the MIRA instrument of the neutron research facility FRM-II. In order to determine the critical edge accurately, the measurements were performed at a small q_z range around the critical edge with a high resolution (small step size Δq_z). The wavelength of the neutrons after a multilayer monochromator was $10.8\mathring{A}$ and the detector was a ^3He-counting tube.

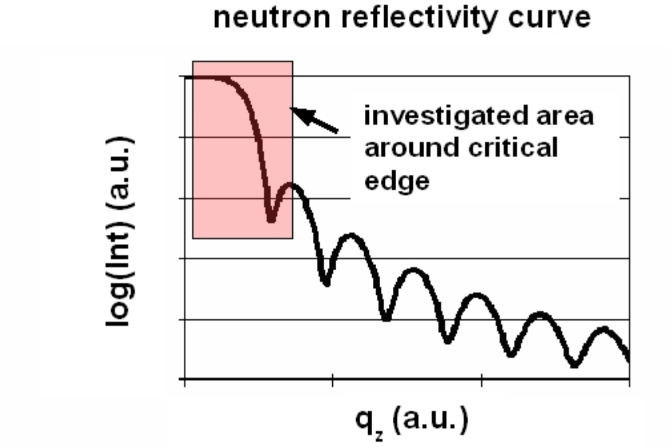

Figure 3.5:
Typical neutron reflectivity curve over a large range for q_z. The investigated area around the critical edge is emphasized.

In order to increase contrast, the polymer films have also been prepared out of deuterated solvents instead of the commonly used protonated solvents. An improvement of contrast could be attributed to the fact that remaining amounts of solvent might still be embedded in the polymer matrix [2] or that a chemical exchange reaction between the polymer and the deuterated solvent occurs. For the samples spin-coated on glass substrates no significant shift of the critical edge could be observed due to this use of deuterated solvents.

We also compared the already mentioned different novel PPV derivates among themselves. Fig. 3.6 shows the critical edge for these materials for films with a fixed film thickness. The thickness of all films was determined afterwards with a laboratory x-ray reflectivity set-up. As an example the x-ray-reflectivity curves for M3EH-PPV solved in deuterated chloroform and deuterated toluene can be seen in Fig. 3.6. The concentration of the polymer in solution was 8 g/l for both solvents and the fits were obtained using the *Parrat* algorithm. For chloroform the film thickness is 90.1 nm and for toluene 39.3 nm only. Hence in order to detail on the effect of the polymers

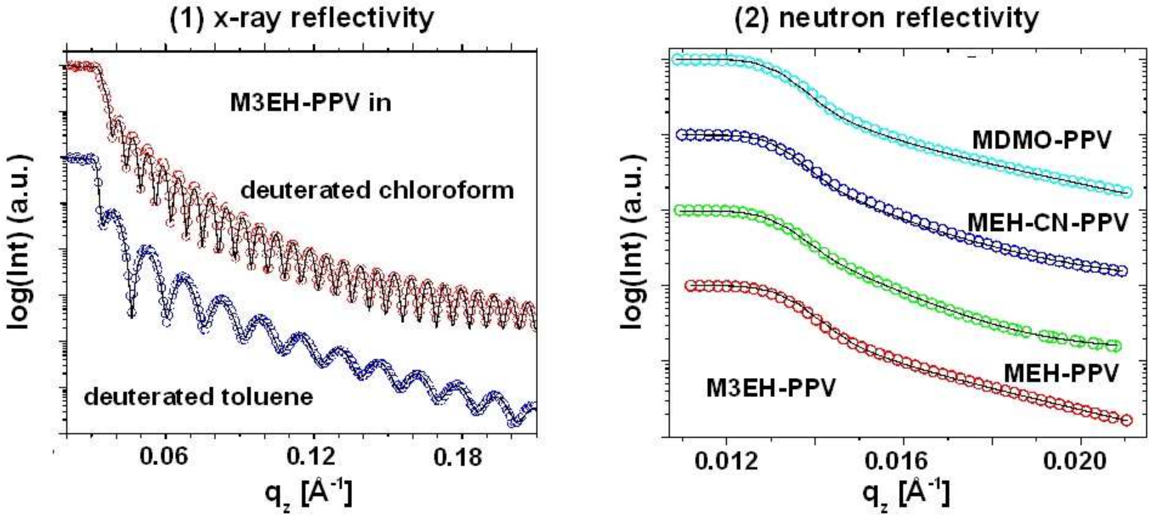

Figure 3.6:
(1) X-ray reflectivity for M3EH-PPV in chloroform and toluene and (2) neutron reflectivity near the critical edge for different PPV derivates.

(type of PPV derivate) on the position of the critical edge the solvent for the different polymer films shown in Fig. 3.6 was deuterated chloroform and the film thickness was almost constant for the different polymers. We can detect an influence of the polymer used. Hence, we can state that the scattering length density varies for the different materials, which allows for contrast in a neutron scattering experiment and thus is the prerequisite of future experiments.

After fitting the scattering length density of the used glass substrates (*Pilkington Optifloat*) this information was used to determine the neutron scattering length densities by fitting the measured curves with *Motofit*. For the different conducting polymers the attendant preliminary scattering length densities (SLDs) are shown in table below:

polymer	SLD (10^{-6} Å^{-2})
M3EH-PPV	0.58
MEH-PPV	0.67
MEH-CN-PPV	0.25
MDMO-PPV	0.44

These values have to be confirmed by NR experiments on silicon substrates and over a larger q_z-range.

Finally we can state that first neutron scattering length densities for conducting polymers were obtained. These results are of interest for further GISANS experiments. In the first neutron experiments the thin polymer films were spin-coated on glass substrates. The scattering length density of the glass turned out to be large in comparison to silicon. Hence the use of silicon substrates might emphasize the shift due to deuterated solvents. These experiments have already been performed at the Mira set-up, but the data analysis is still ongoing. Additional measurements over an increased q_z-range are useful for better statistics and for evaluation of film roughness.

[1] S. C. Veenstra et. al., Progress in Photovoltaics: Resarch and Application 2007 (15)

[2] J. Perlich et. al., Macromolecules, 2009, 42, 337-344

3.4 Thin polymer films for photovoltaic applications

S. M. Prams, M. A. Ruderer, R. Meier, P. Müller-Buschbaum

The idea of directly converting the suns radiation into electric current sure is an alluring thought and therefore subject of many research efforts. The most widely spread solar technology at the moment is based on anorganic semiconductors, for instance silicon. Decades of research and engineering have resulted in ready-made devices that can be put on rooftops or solar parks. The power conversion efficiency of this technology is yet considerably higher compared to others, but the slow down in the speed of improvement may convey the impression that we are already close to the maximum reachable. The use of silicon in solar technologies has many sound aspects but also disadvantages in terms of high financial and energy costs as well as problems resulting from the material stiffness. These factors lead to limitations that narrow the field of possible applications.

This is where conjugated polymers come into play. Its not about competing with anorganic devices but all about bringing solar energy generation down from the rooftop and into everyday life. By covering with an photovoltaic coating theoretically ideally nearly every product could be turned into an photovoltaic device. Of course this will not be reasonable for every product but a huge area of possible applications makes this research-topic very promising. Another aspect of polymers shows great promise for future use: The fact that today plastics industry is highly developed justifies the assumption of cheap and fast production capabilities for future polymer-base functional products.

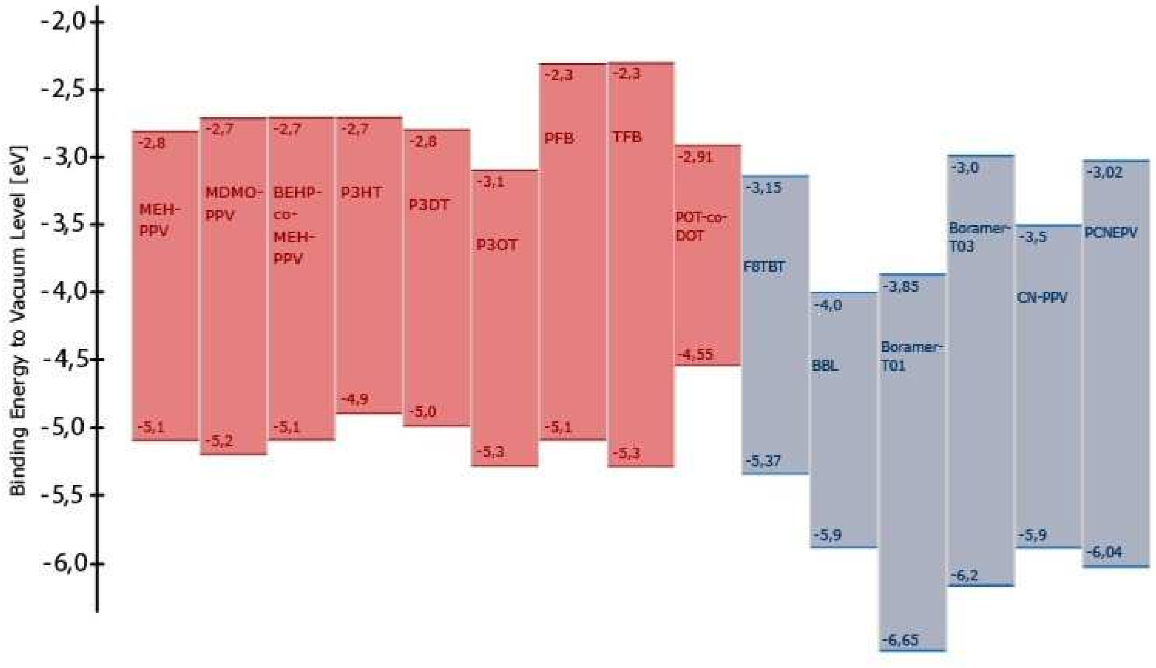

Figure 3.7: HOMO and LUMO of some selected conducting polymers, red: p-type, blue: n-type.

The use of conducting polymers is the basic requirement for working electronic devices. Conductance is established by conjugated bonds within and in between the monomers. Yet there is only a limited but steadily growing number of conducting polymers available. Fig 3.7 shows a selection together with the assumed band gap positions derived from the highest occupied molecular orbital (HOMO) and the lowest unoccupied molecular orbital (LUMO).

As shown in Fig 3.7 there are some polymers assumed to be of n-type and some of p-type behavior. For a photovoltaic device high mobility of both charge carriers, electrons and holes is needed. Hence a combination of n- and p-type polymers is of advantage. Apart from that, a distinct band architecture of the chosen polymers is required: If the band gap of the first polymer would be energetically lying within the band gap of the second polymer, the combination can be useful for an organic LED (OLED) but not for a solar cell due to much recombination in the smaller band gap area. What is desired is a step-like arrangement where the LUMO of the n-type polymer lying below the LUMO of the p-type polymer and the HOMO of the n-type polymer lying below the HOMO of the p-type polymer. Thus for binary blend systems the selection of two conducting polymers has to start with the inspection of the HOMO and LUMO levels. Beside this important aspect the resulting structures due to phase separation of both polymers are of essential importance.

To illustrate this, we focus on an example system based on poly (3-hexylthiophene) (P3HT). Thin films of a mixture of P3HT and an n-conducting polymer (not shown in Fig 3.7) where produced via spin-coating from toluol solution. Different concentrations where selected, ranging from 6 mg/ml to 12 mg/ml. Additionally, the temperature conditions during fabrication were altered. The Samples were investigated via UV-VIS spectroscopy and optical microscopy.

As a first step the glass substrates where cleaned for 15 minutes in an acidic bath consisting of H_2O, H_2O_2 and H_2SO_4 [1]. P3HT and the n-conducting polymer were solubilized in toluol resulting in two solutions with a concentration of 12 mg/ml. P3HT showed a bad solubility at room temperature but was soluble after heating the solution for some time. Subsequently four solutions with the concentrations 12 mg/ml (**P1**), 10 mg/ml (**P2**), 8 mg/ml (**P3**) and 6 mg/ml (**P4**) were prepared by mixing the two polymer solutions with the respective amount of toluol. These solutions were kept under constant temperature until the preparation of the films.

First investigations of **P1** by light microscopy as shown in Fig 3.8 revealed rather big separated aggregations of polymers and a very inhomogeneous size and density distribution over the sample. We suggest that the solubility problems at room temperature mentioned above led to an precipitation due to the cooling during spin-coating.

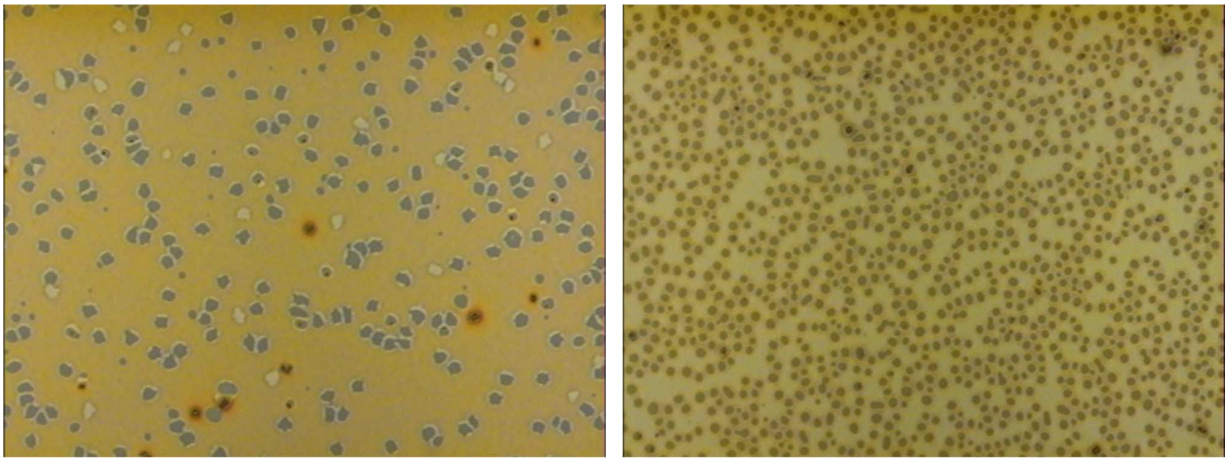

Figure 3.8: Samples from **P1** at scale factor 100 without heating (left), with heating (right).

Although the structure size decreases with heating the substrate during film application, it is still several orders of magnitude above the desired length scale of the exciton diffusion length in the low ten nm regime. To evaluate the influence of the film thickness on the observed texture size further investigations are necessary.

[1] P. Müller-Buschbaum et al., Spectrochimica Acta Part B 59 (2004) 1789

3.5 Preservation of the morphology of a self-encapsulated thin titania film in a functional multilayer stack: An X-ray scattering study

J. Perlich, M. Memesa[1], J. S. Gutmann[1,3], P. Müller-Buschbaum

[1] Max-Planck Institute for Polymer Research, Mainz, Germany
[2] Johannes Gutenberg University, Mainz, Germany

Nanostructured titania thin films have attracted increasing interest because of their intriguing physical properties. In most potential applications, the morphology of the nanostructured titania is of crucial importance for the performance. For example in photovoltaics, the morphology influences charge carrier transport routes and thus electron-hole recombination probabilities. Consequently, the control of the morphology is crucial for the preparation of nanostructured titania thin films. As a consequence, the preservation of the tailored morphology is the main requirement for the successive stages of preparation towards a photovoltaic system.

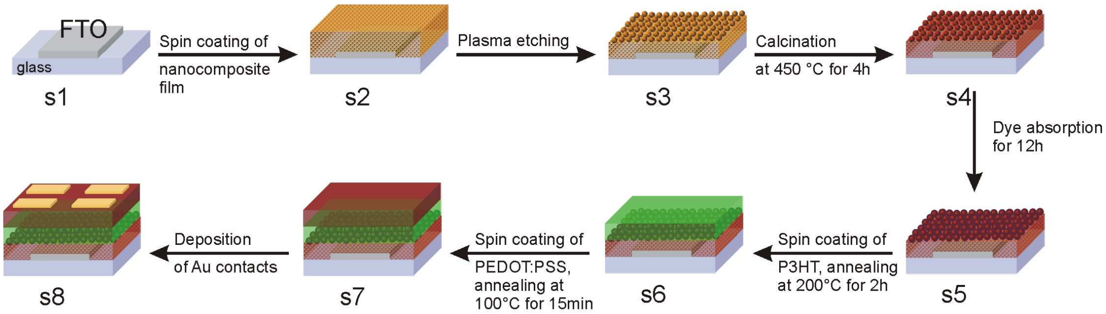

Figure 3.9:
Scheme of the preparation route of the functional multilayer stack resulting in a photovoltaic demonstration cell. Stages of the cell preparation. Taken from [1].

In the presented work, structural changes of the tailored titania morphologies are tracked as a function of a multilayer stack build-up [1]. The investigated preparation stages of the functional multilayer, which form a photovoltaic demonstration cell resembling a so-called hybrid photovoltaic cell, are schematically presented in Figure 3.9. For the fabrication a novel approach is employed, which comprises the integrated self-encapsulation of the titania nanostructures hence an encapsulation mechanism supplied by its own preparation components [2]. The encapsulation serves as alternative to the conventional compact titania barrier layer.

Within the experiment the described multilayer stack build-up is characterized using microfocus grazing incidence small angle X-ray scattering (μ-GISAXS) at the HASYLAB beamline BW4 [3]. The recorded 2d scattering patterns and the corresponding stage of the multilayer build-up are shown in Figure 3.10a. From the qualitative point of view the 2d scattering pattern of the substrate shows strong diffuse scattering (broad intensity distribution) parallel to the horizontal axis at small exit angles α_f, which can be clearly attributed to the strong well-defined roughness of the FTO layer. After the spin-coating of the polymer nanocomposite film, the 2d scattering pattern changes considerably. The noticeable increase of intensity in vertical direction indicates an induced smoothing of the FTO roughness. Nevertheless, the subsequent etching of the PDMS, hence reducing its thickness, has only an influence on intensity in vertical direction. The horizontal distribution remains, thus there is no change in the titania morphology. After calcination, the titania nanostructures are located directly on top of the FTO smoothing the surface. Additionally to the characteristic FTO structure a characteristic length scale originating from the titania nanostructures is expected. As a consequence the GISAXS measurement results in a 2d scattering pattern resembling a combination of the pattern of bare FTO as well as the nanocomposite layer. The coating of a dye monolayer has barely influence on the intensity distribution.

Continuing the stack build-up with spin-coating the P3HT layer and successive annealing results again in a pronounced change, but the scattering pattern appears to have similar shape as the pattern after the spin-coating of the polymer nanocomposite film. After spin-coating and annealing of the PEDOT:PSS layer, the scattering pattern slightly changes, which can be attributed to the slight loss of scattering contrast from the underlying films. But since there is no change in the shape of the pattern, the PEDOT:PSS does not change the hitherto observed structures. Finally, the μ-GISAXS measurement of the complete device stack with the sputtered Au cathode yields a broader intensity distribution occurring at the expense of a decreasing out-of-plane intensity.

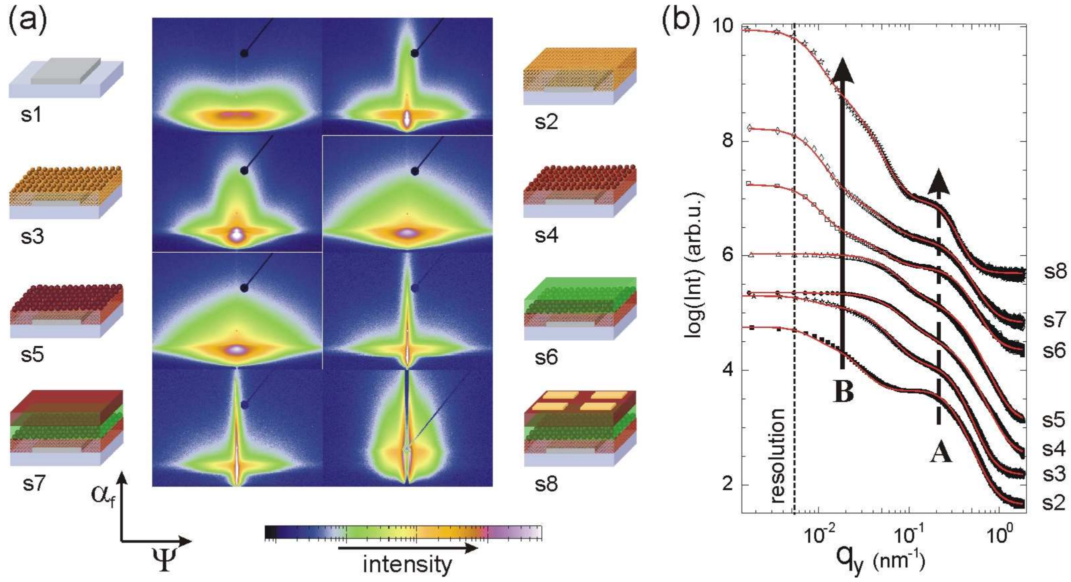

Figure 3.10:
(a) A composition of 2d scattering patterns as a function of the stack build-up. (b) Out-of-plane cuts at the position of the critical angle for titania as a function of the q_y component of the scattering vector. The dashed line indicates the resolution limit of the μ-GISAXS experiment. The two structures are marked with A and B. The arrows display schematically the structures as a function of the stack build-up. Taken from [1].

In order to obtain a quantitative measure from these 2d scattering pattern so-called out-of-plane cuts are performed (see Figure 3.10b). Two most prominent in-plane-length scales are observed: the smaller structure (Λ_A = 36 nm) is provided by the substrate FTO-electrode, whereas the bigger structure (Λ_B = 479 nm) originates from the active layer morphology. In other words, the demonstration cell is fully characterized by two lateral lengths over the entire multilayer stack build-up process. From these findings, we can conclude that for the investigated type of multilayer stack the tailored morphology of the titania thin film is preserved throughout the entire multilayer fabrication process and thus tailoring of this lateral structure to match typical mean free paths is meaningful. Furthermore, applying the required additional functional layers and associated thermal treatment do not produce unintentionally any further and unwanted structure to the layer stack nor destroy the fabricated nanostructure.

[1] J. Perlich, M. Memesa, A. Diethert, E. Metwalli, W. Wang, S. V. Roth, A. Timmann, J. S. Gutmann, P. Müller-Buschbaum, ChemPhysChem (2009) *accepted*

[2] M. Memesa, S. Weber, S. Lenz, J. Perlich, R. Berger, P. Müller-Buschbaum, J. S. Gutmann, *submitted*

[3] S. V. Roth, R. Döhrmann, M. Dommach, M. Kuhlmann, I. Kröger, R. Gehrke, H. Walter, C. Schroer, B. Lengeler, P. Müller-Buschbaum, Rev. Sci. Instr. **77**, 085106 (2006)

3.6 Nanostructuring inorganic material by copolymer-assisted self-assembly and its multifunctional use for dye-sensitised solar cells

S. Guldin, S. Hüttner[1], U. Steiner[1], P. Müller-Buschbaum

[1] Department of Physics, Cavendish Laboratory, University of Cambridge, GB

Among all new generation photovoltaic concepts dye-sensitized solar cells (DSSCs) are particularly promising with reported record efficiencies of 11%. In this system charge carrier generation takes place in a photoactive layer of dye molecules which is sandwiched between an electron and a hole conducting material. The most crucial efficiency parameters in this device concept are therefore an extremely high interfacial area, favorable dynamics of charge-carrier reactions and electronic band alignment of the three components: electron conducting inorganic semiconductor, dye, hole transporting material.
The aim of this work was the development and study of a material system which enables the control over several device limiting factors of the inorganic electron conducting material.

I. Control over the structure on the 10 nm length scale
An alternative approach was pursued to synthesise mesoporous TiO_2, namely *nanostructuring inorganic material by copolymer-assisted self-assembly*. The main aim of this approach was to overcome the lack of structural control in conventionally used methods by introducing a structure directing agent in form of a diblock copolymer, poly[1,4-isoprene-*b*-(ethylene oxide)] (PI-*b*-PEO) ($M_w = 32$ kg/mol). Suitable inorganic nanoparticles are preferentially incorporated by one block of the amphiphilic copolymer and therefore take part in the self-assembly process of copolymers, known as microphase separation.

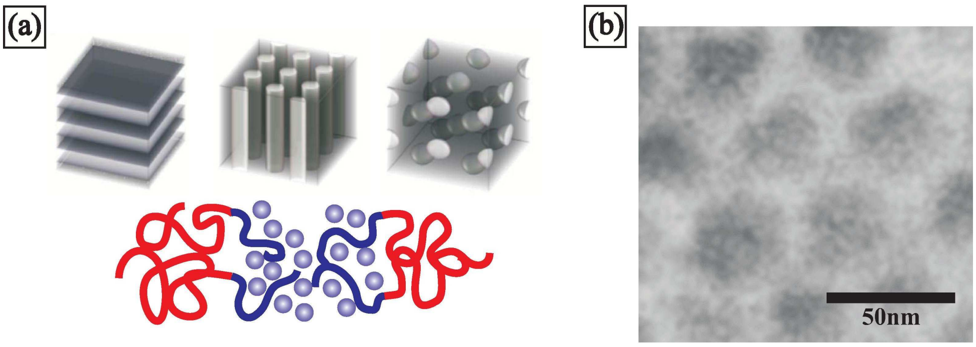

Figure 3.11:
(a) Schematic representation of a copolymer/sol material assembly and typical evolving structures which mainly depend on the volume ratio of the two components. (b) Cross-sectional SEM image (close-up) of a copolymer derived TiO_2 film.

Control over the resulting morphology is achieved by fine-tuning of the molecular weight of the copolymer blocks and the amount and nature of the incorporated TiO_2 nanoparticles. The developed hydrolytic sol-gel chemistry is particularly useful, because it produces well dispersed particles with diameters significantly smaller the radius of gyration of the PEO block. This enables a satisfactory incorporation of these particles into the diblock copolymer assembly, producing homogeneous morphologies on the length scales of the copolymer blocks. Ordered morphologies structures are obtained within hours with a quality and reproducibility which is highly tolerant to ambient conditions. Pore sizes of around 20 - 25 nm were achieved, significantly larger than the random micropores in films derived from sintering of 20 nm-sized nanoparticles or other copolymer approaches. This opens up the possibility for enhanced pore infiltration of solid state hole conducting materials.

II. Control over crystallinity and crystal structure

Previous approaches with other copolymer agents reported of low temperature resistance and collapse of structures at desirable crystallization temperatures. The developed material system enabled the synthesis of significant thicker TiO_2 walls (12 - 15 nm) which resulted in structural stability up to 650 °C. Such high annealing temperatures are accompanied by anisotropic crystallite growth within the confined network to up to 24 nm in size, 60 % larger than crystallite sizes reported so far in copolymer derived morphologies. The associated resistivity was 83 % less than in typical low temperature annealing procedures (400 °C), allowing higher electron mobilities and potentially less charge carrier recombination.

III. Control over structure on micrometer length scale for absorption enhancement

The effect of a photonic crystal top layer on the efficiency of dye-sensitized solar cells has been controversially debated. Different theoretical approaches report a variety of possible effects associated with the periodic dielectric lattice in the photonic crystal. However no experimental approach enabled a suitable layer sequence for a regular illumination of a working device.

A polymer-derived mesoporos structure is not porous before temperature annealing. This enables to deposit additional layers such as a photonic layer before creating the pores in all layers by high temperature treatment as shown in Figure 3.12.

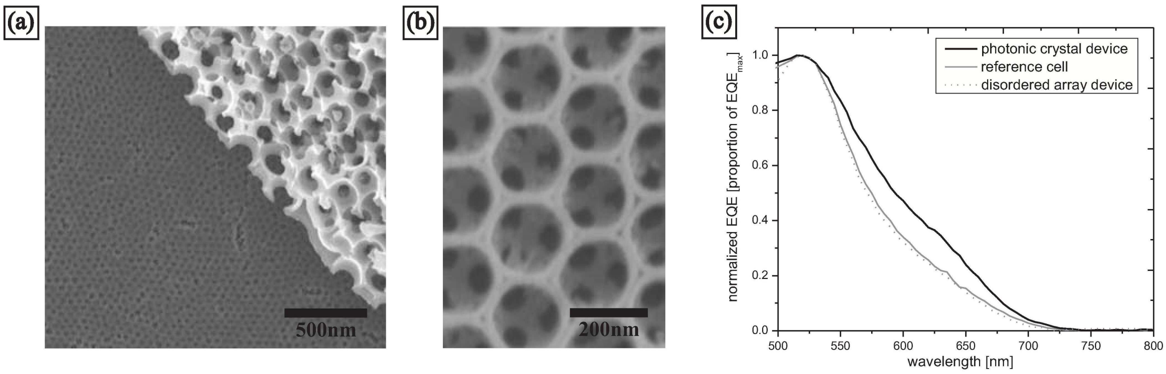

Figure 3.12:
(a) Tilted (45°) SEM image of a TiO_2 photonic crystal on top of a mesoporos underlayer. (b) SEM top view of a photonic crystal layer. (c) Normalized quantum efficiency spectra of different cell types.

In this work, a functioning double layer solar cell in the previously identified optimal configuration could therefore be assembled for the first time. The normalized spectral response of the solar cells was significantly increased in the yellow to red wavelength range. Since multiple scattering as a result of imperfection of the crystal can be ruled out, the resulting effects have to be attributed to the periodic dielectric lattice in the photonic crystal. A normalized increase in photon to electron conversion of up to 20.4 % was observed in the range from 520 nm to 725 nm. Device performance was determined on ultrathin TiO_2 films (400 nm) in order to exclude any possible contributions from other sources of light enhancement, like scattering at cracks.

[1] H. J. Snaith and L. Schmidt-Mende, Advanced Materials **19**, 3187-3200 (2007)

[2] A. Mihi and H. Miguez, Journal Of Physical Chemistry B **109**, 15968-15976 (2005)

[3] S. Guldin, S. Hüttner, M. Kolle, M. E. Welland, P. Müller-Buschbaum, R. H. Friend, U. Steiner, N. Tetreault, in preparation

4 Polymer-hybrid systems

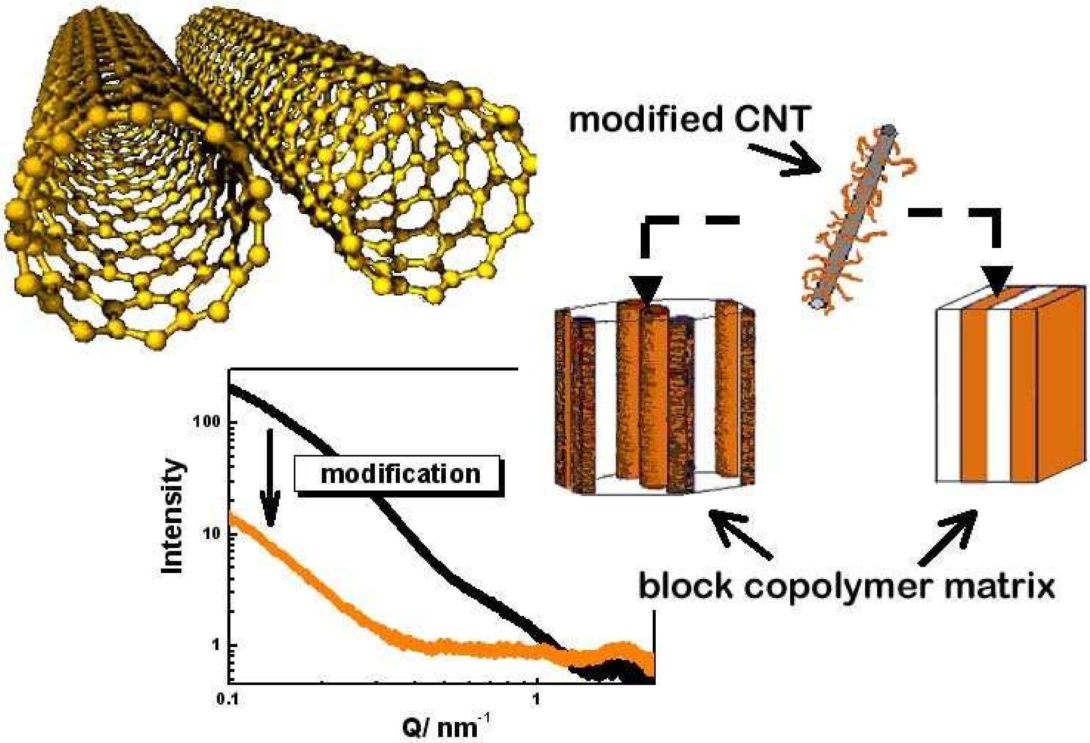

4.1 Sidewall modification of carbon nanotubes for preparation of functional nanocomposites

A. A. Golosova, A. Timmann[1], R. Jordan[2], C. M. Papdakis

[1] HASYLAB at DESY, Hamburg

[2] TU München, Department Chemie, Garching

In polymer nanocomposites, the nanometer size active fillers can change the material properties of polymer matrices within a wide range. Among such fillers, carbon nanotubes (CNTs) have been paid attention for various potential applications because they can lead to mechanical reinforcement and superior thermal and electrical conductivities, as well as thermal resistance. However, until now CNT-polymer composites face the same challenges as common fillers, namely, the efficient incorporation and compatibilization of the CNTs with the surrounding polymer matrix, which is crucial for the anticipated improved properties of the composite.

To tune the surface properties of CNTs and improve their dispersion ability within solvents or polymer matrices we will extend a recently developed modification to form self-assembled monolayers from (bi)phenyl diazonium salt derivatives as well as various polymer grafts by surface-initiated polymerization on carbon-based substrates [1] to the sidewall modification of CNTs. Modified carbon nanotubes (mCNTs) will then be incorporated into suitable bulk block copolymers, which are known to exhibit a well-defined phase behavior in respect to overall molecular weight and the internal fraction of the individual blocks. Depending on the coating, the mCNTs will accumulate in one of the polymer phases of the block copolymer. In this way the block copolymer morphology will serve as a three dimensional (3D) template for the directed assembly of the mCNT.

The project started with the sidewall chemical modification of single-walled (SW) and multi-walled (MW) CNTs in acetonitrile solution of 4′-substituted aryl diazonium salts (nitro-, chlor-, and trifluorocarbon- (bi)phenyl) (Fig. 4.1). In order to compare the results of the newly applied modification procedure with the previously used methods, we also performed modification of carbon nanotubes with diazonium compounds according to the techniques described in the literature (the "Tour" reaction [2], and the reaction in hydrophosphorous acid/water solution [3]). Successful covalent functionalization of the nanotubes was confirmed by Raman spectroscopy and thermo-gravimetric analysis (TGA).

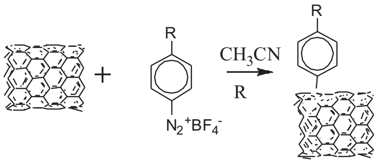

Figure 4.1:
Sidewall CNT modification (R= NO$_2$, Cl, CF$_3$)

The Raman spectra of modified CNTs (Fig. 4.2) are significantly different from the one of raw SWCNTs. The main feature is the increase of the intensity of the disorder mode (D-band), relative to a G-band (which is due to the graphitic structure) as expected for the conversion of sp^2-hybridized carbons to sp^3-hybridization state due to the introduction of covalently bound moieties to the nanotube sidewalls.

While Raman spectroscopy supplies us with information about the structure of the carbon nanotube framework, TGA gives the chemical composition of the samples. Upon heating up to 900 ^{0}C in argon atmosphere, the observed weight losses were in the range of 5-10 %, which is lower than the reported values (for "Tour reaction" [2], electrochemical modification [4], etc). One of the possible reasons is the use of a much smaller concentration of the diazonium salt (0.15-0.5 equivalents relative to the amount of atomic carbon while in the "Tour" reaction 16 equivalents of salt are used). Second, the CNTs used in the present study have large diameters (ca 1.4 nm and 13-16 nm for SW and MW CNTs, respectively), thus their reactivity of is lower. Moreover, it is well known that electrochemical modification and functionalization of carbon nanotubes in water solution of diazonium salts results in multilayer formation of the aniline derivatives on the carbon surfaces [3, 4]. In the case of surface modification by aryl diazonium salts in acetonitrile solution the formation of monolayers was confirmed [1]. Thus we attribute the smaller mass loss values to the fact of the formation of monolayers on the carbon nanotube surfaces.

To investigate the structure and dispersion ability of modified CNTs, we performed small-angle X-ray scattering (SAXS) experiments at BW4 at HASYLAB on dilute aqueous dispersions (0.1 wt. %) of raw and modified SW and MW CNTs (Fig. 4.3). Since the dispersions were visually inhomogeneous, measurements were carried out at several locations of the sample. The strong scattering from big agglomerates observed for raw CNTs (both SW and MW) was significantly reduced for the modified CNTs, which confirms better dispersibility of the miodified samples.

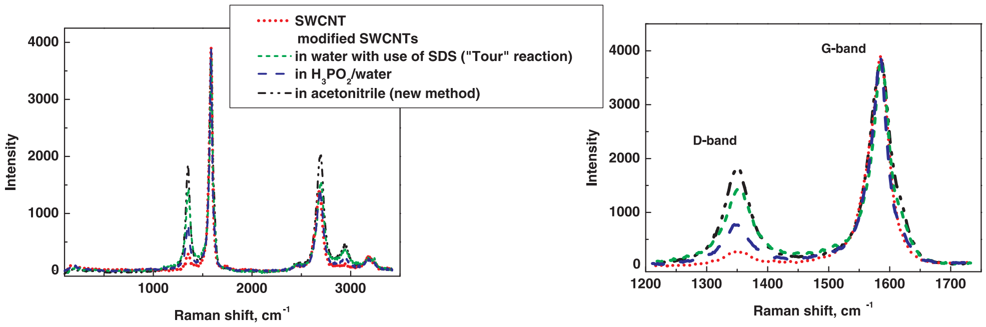

Figure 4.2:
Raman spectra of SWCNTs: raw and modified by different techniques (right figure is a zoom of the region 1200-1750 cm^{-1})

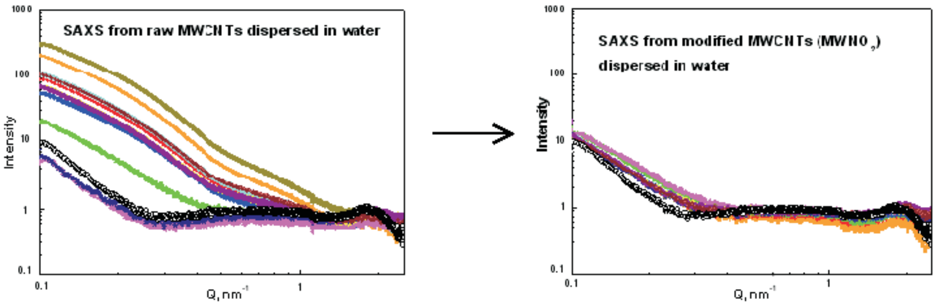

Figure 4.3:
SAXS from aqueous dispersion of raw (left) and modified (right) MWCNTs (different lines correspond to different locations along the sample)

The project has been funded by the International Graduate School of Science and Engeneering (IGSSE).

[1] S. Q. Lud, R. Jordan et al. *J. Am. Chem. Soc.* **128** 16884 (2006) U. Schmelmer, R. Jordan et al. *Small* **3** 459 (2007)

[2] C. A. Dyke, J. M. Tour *Nano Lett.* **3** 1215 (2003)

[3] P. Abiman, G. G. Wildgoose, R. G. Compton *Int. J. Electrochem. Sci.* **3** 104 (2008)

[4] J. K. Kariuki, M. T. McDermott *Langmuir* **15** 6534 (1999)

4.2 Progressive selective gold deposition from a flowing stream of solution onto a polymer template

E. Metwalli, J.-F. Moulin[1], S.V Roth[2], P. Müller-Buschbaum

[1] GKSS-Forschungszentrum, Geesthacht, Germany
[2] HASYLAB at DESY, Hamburg, Germany

Deposition of gold nano-particles on solid surfaces in an ordered pattern with high spatial density and controllable size is important for possible applications in nanoelectronics, nanocatalysts, bioelectronics, magnetic recording devices, and gas sensors. The soft nanostructured polymer film can be used as a template for patterning of hard inorganic materials such as metal nanoparticles [1]. The recent advances in the patterning of polymers have enabled the fabrication of integrated micro- and nanosystems with a high degree of complexity and functionality. By deposition of nanoparticles onto block copolymer templates, a selective affinity of the nanoparticles to one or another block of the block copolymer film will provide a controllable distribution of nanoparticles. For instance, noble metal particles was found to preferentially decorate a particular domain in diblock copolymer films [2]. X-ray standing wave fluorescence [3] was recently used to prove that gold nanoparticles tend to diffuse toward the center of the poly(2-vinylpyridine) (P2VP) domains of polystyrene-block-poly(2-vinylpyridine), P(S-*b*-2VP), diblock copolymers. The interaction of gold with P2VP in P(S-*b*-2VP) diblock copolymer via bonding with nitrogen atoms explained the preferential adsorption to the P2VP domains. Gold decoration of polystyrene on polystyrene-block-polymethylmethacrylate P(S-*b*-MMA) diblock copolymer thin films is explained by the difference in the wetting properties of the two copolymer domains. Generally, the specific nature of the selective gold-polymer interaction that causes the self-assembly is still far from being completely understood.

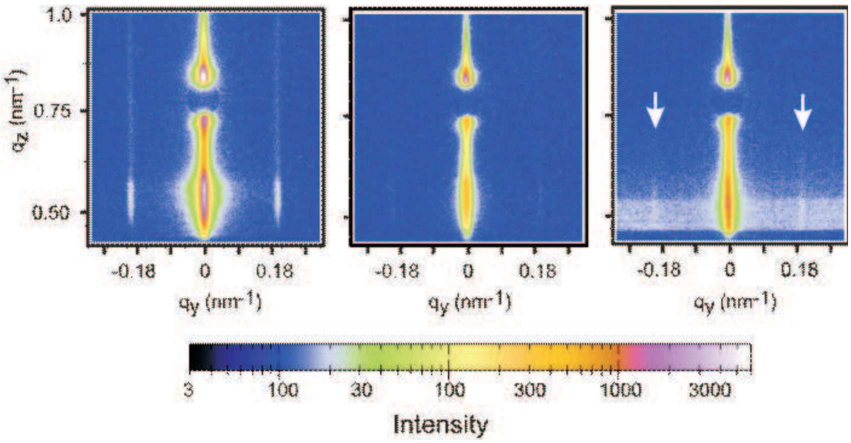

Figure 4.4:
2d GISAXS patterns for the dry, wet (DI water) polymer film, and after injection of gold nanoparticles into the fluidic channel (from left to right).

In the present work we introduce the flow deposition technique to investigate the deposition behavior of gold nanoparticles onto a phase-separated polystyrene-block-polyethylene oxide P(S-*b*-E) diblock copolymer film. The parallel cylinder morphology of the diblock copolymer thin film has been attached to a fluidic cell and a solution of gold nanoparticles was injected in the flow channel. The fluidic cell is mounted on the beamline of grazing incidence small-angle X-ray scattering (GISAXS) to investigate the in situ progressive gold nanoparticles decoration of the polymer film. The continuous flow stream of the nanoparticles solution force the nanoparticles to move along the flow channel and only those with preferential interaction to one of

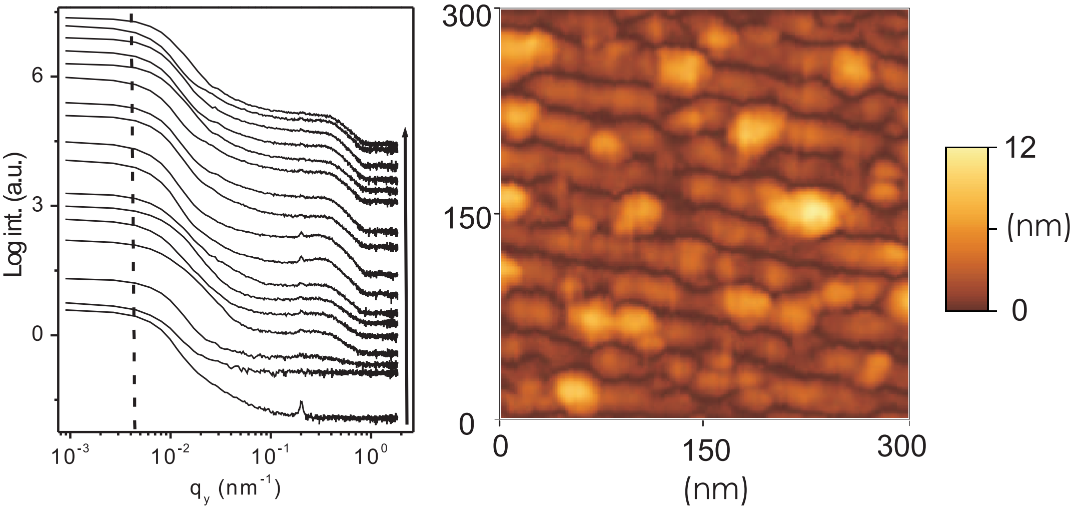

Figure 4.5:
Out-of-plane q_y cuts of the GISAXS patterns of polymer film in contact with a flowing stream of gold nanoparticles solution. From bottom to top the dry, wet (DI water) polymer film, and during a continuous flow-stream (2μ/min) of gold nanoparticles solution in steps of 200 s. The AFM image shows aggregates of the gold particles on top of the cylinder domains.

the diblock domains will gradually assemble, leading to formation of patterned metal/polymer nanocomposite.

From Figure 4.4 the polymer template of P(S-*b*-E) shows two characteristic peak maxima indicating a periodic structure of about 28 nm. After the DI water injection into the fluidic channel, a disappearance of the side peaks is observed due to loss of the contrast by water that act as a mediator between the two polymer blocks of the phase-separated block copolymer. The gold nanoparticles with 9.6 nm is immediately injected following the water stream and the side peaks are instantaneously reappeared indicating a strong selectivity adsorption of the gold nanoparticles to one phase of the block copolymer film. The out-of-plane q_y cuts of 2d GISAXS patterns collected while a stream of the nanoparticles solution is continuously flowing on top of the polymer template is shown in Figure 4.5. The continuous stream of gold nanoparticles solution in the fluidic channel and subsequent GISAXS measurements reveals an increase of the continuous gold selective deposition. As the subsequent additional amount of gold nanoparticles increases, the overall surface scattering is dominating with much less selectivity characteristics of the gold particles as an almost monolayer of gold film is approached. AFM measurments have been performed ex-situ for a polymer film that has been exposed to the flow-stream of gold nanoparticles solution (5 nm) for only short time. The image in figure 4.5 indicates a preferential adsorption to one particular domain in consistent to the GISAXS results. These experiments suggest an efficient alternative gold nanopattering method compared to those based on complex and costly vapor deposition techniques.

[1] E. Metwalli, S. Couet, K. Schlage, R. Röhlsberger, V. Körstgens, M. Ruderer, W. Wang, G. Kaune, S.V. Roth, P. Müller-Buschbaum, Langmuir **24**, 4265 (2008)

[2] M.M. Abul Kashem, J. Perlich, L. Schulz, S.V. Roth, P. Müller-Buschbaum, Macromolecules **41**, 2186 (2008)

[3] B.H. Lin, T.L. Morkved, M. Meron, Z.Q. Huang, P.J. Viccaro, H.M. Jaeger, S.M. Williams, M.L. Schlossman, J. Appl. Phys. **85**, 3180 (1999)

4.3 Investigation of a colloidal silver nanoparticle gradient layer prepared by drying between two walls of different wettability

S. V. Roth[1], M. Kuhlmann[1], H. Walter[2], A. Snigirev[3], I. Snigireva[3], B. Lengeler[4], C. G. Schroer[5], M. Burghammer[3], C. Riekel[3], P. Müller-Buschbaum

[1] HASYLAB at DESY, Hamburg, Germany
[2] CSEM SA, Zürich, Switzerland
[3] ESRF, Grenoble, Switzerland
[4] RWTH Aachen, Aachen, Germany
[5] TU Dresden, Dresden, Germany

Colloidal nanoparticles are fascinating and versatile building blocks for the fabrication of two- (2D) and three-dimensional (3D) micro- and nano-structures [1], because of their uniform size, shape, composition, and properties (both surface and bulk). The self-organization of such nanoparticles turned out to be a powerful tool for the construction of highly ordered colloidal crystals, biological active substrates and optical and electronic devices [4-6].

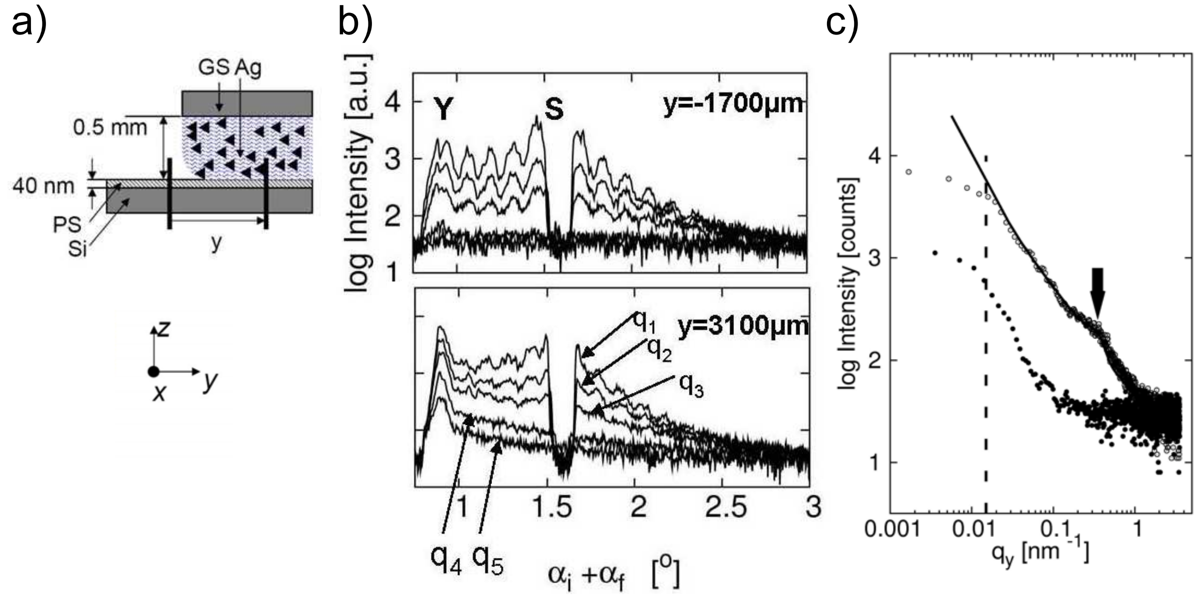

Figure 4.6:
a) Sketch of the sample preparation. The colloidal silver nanoparticle solution (Ag nanoprisms) was filled in the gap (0.5 mm) between the substrate (Si-wafer covered with 40 nm PS) and a glass slide (GS). The resulting menisci are exaggerated for clarity. The investigated part is marked with y. b) Detector (Δq_y=0) and off-detector scans performed for the pure PS and the silver nanoparticle covered part ($q_{1,2,3,4,5}$ correspond to Δq_y=0 nm^{-1}, 0.011 nm^{-1}, 0.021 nm^{-1}, 0.06 nm^{-1}, 0.12 nm^{-1} respectively. Y denotes the region of the Yoneda peaks resulting from the Si-substrate, the PS-layer and the Ag-nanoparticle layer. The change in amplitude of the resonant diffuse scattering (RDS, wiggles) is clearly visible as well as the build-up of intensity for $\Delta q_y \neq 0$ along the gradient.c) Out-of-plane scans of the pure PS-film at y= -1700 μm (filled circles) and of the Ag nanoprism structure at y= 3100 μm (open circles) for q_z= 0.102 Å^{-1}. The side maximum at $q_{y,max}$ (marked with arrow) indicates the most-prominent in-plane length as a result of the build-up of the Ag nanostructure. The solid line is fit to the data using the program IsGISAXS [6]. The dashed line marks the resolution of the μGISAXS experiment.

In the presented work we investigated the structure of a colloidal silver (Ag) nanoprism gradient, prepared by drying between a non-wettable spin-coated polystyrence (PS) surface and a wettable glass slide, which was removed after drying, see fig. 4.6a). The experiment was performed at the beamline ID13 of ESRF (wavelength 0.97 nm, beam size 5 μm, step size 100 μm). As can be seen in the detector and off-detector scans in fig. 4.6b), the PS film shows a well-defined roughness correlation with the underlying silicon (Si) surface, which decreases in the Ag nanoprism covered part. Fig. 4.6c) two out-of-plane scans are shown for the two positions in fig. 4.6b). Here, a fit using a prism-model in IsGISAXS is used to fit the data and to extract the corresponding nearest-neighbor distance ξ and the geometry of the nanoprisms (edge 14 nm, height 7 nm).

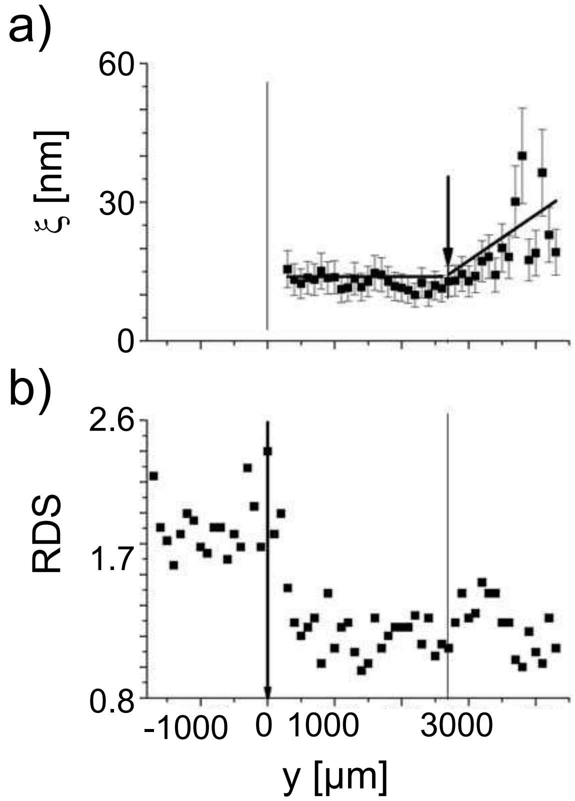

Figure 4.7:
a) Nearest neighbor distance of the deposited nanoprisms ξ, plotted as a function of y. Note the double gradient structure: PS-Ag-layer with constant ξ followed by a region of increasing ξ at a position of y= 2600 μm indicating the end of the influence of the meniscus boundary conditions (Fig. 4.6a)). b) Resonant diffuse scattering amplitude (RDS amplitude) as a function of the scan position. The nominal zero point (vertical arrow) shows a marked decrease in the RDS amplitude due to the additional roughness induced by the Ag-layer. The arrows and the vertical lines indicate the two cross-over points.

In fig. 4.7 we quantify our analysis by presenting the nearest-neighbor distance ξ and the RDS-amplitude. Clearly, a double cross-over regime is visible. Firstly, the decrease in RDS-amplitude stems from statistically deposited nanoprism (onset of the gradient, y=0 μm) with constant ξ. Here, the drying kinetics is governed by the meniscus, see fig. 4.6a). Secondly, ξ shows a marked increase to a final plateau value. For y$\leq$4300 μm the increased, but again constant ξ indicate the equilibrium structure of this complex, double-structured gradient.

[1] T.A. Witten, Rev. Mod. Phys. **71** S367 (1999)

[2] J. Aizenberg et al., Nature **398**, 495 (1999)

[3] R. Singhvi et al., Science **264**, 696 (1994)

[4] S.-D-. Tzeng et al., Adv. Mater **18**, 1147 (2006)

[5] S.V. Roth et al., Appl.Phys.Lett. **91**, 091915 (2007)

[6] R. Lazzari J. Appl. Cryst. **35**, 406 (2002)

4.4 Formation of magnetic nanoparticles inside a block copolymer template - an *in situ* GISAXS study

M. M. Abul Kashem, K. Schlage[1], S. Couet[1], R. Röhlsberger[1], S. V. Roth[1], P. Müller-Buschbaum

[1] HASYLAB at DESY, Hamburg, Germany

Metal-polymer nanocomposite films receive increasing attention due to the potential novel applications related to the optical and magnetic behavior. So far, different preparation techniques have been established. Among them sputter deposition of the metal is frequently used.

In the present investigation we focus on the formation of a regular array of magnetic nanoparticles by sputter deposition of iron, using a diblock copolymer thin film template. Selective positioning of iron atoms was achieved because of polar interactions between the diblock copolymer and the iron atoms. An *in situ* observation of the sputter deposition of iron and spatial positioning of iron atoms inside the block copolymer template was carried out with grazing incidence small angle x-ray scattering (GISAXS). Besides, atomic force microscopy (AFM) was also used to image the allocation of iron nanoparticles on the polymer template.

The templates used in this investigation were prepared by spin coating of a solution of an asymmetric PS-*b*-PMMA diblock copolymer in toluene on top of a PS-*r*-PMMA copolymer grafted silicon substrate. Approximately 80 nm thick films of PS-*b*-PMMA, having ordered arrays of upright cylindrical domains of PMMA, were obtained by subsequent annealing at 165 °C in an oven under vacuum (1×10^{-3} mbar) for 72 hours. A portable DC magnetron sputtering chamber equipped with an ultra-high vacuum (UHV) system and two beryllium windows enabling the GISAXS experiment simultaneously on the thin polymer film during sputter deposition of iron [1] had been used for *in situ* observation of the nanoparticle formation inside the PMMA domains present in the template. Argon (purity = 6.0) plasma was used to knock the iron atoms out of the target. The target was an isotope ^{57}Fe of iron (purity = 99.999%). Iron was sputtered at a working pressure of 5×10^{-3} mbar (Argon pressure) for 19 minutes with a rate of approximately 0.2 nm/minute. The *in situ* GISAXS [2] experiment was carried out at the beamline BW4 at HASYLAB with an incident angle $\alpha_i = 0.32°$. The GISAXS data were recorded every minute during sputtering. Along with the *in situ* GISAXS study, one template was prepared separately with sputtering of 1.6 nm nominal thicknesses of iron to investigate the surface topography of the thin films by AFM.

Figure 4.8(a) shows out-of-plane cuts (at the critical angle of PS) obtained from the 2d GISAXS patterns after every 60 seconds of sputtering starting from the template without sputtered iron. The out-of-plane cut before sputtering shows no intensity peak. Although the template has a regular ordered array of upright cylindrical domains of PMMA, no pronounced scattering from the regular distances among cylindrical domains as a structure factor peak is observed. The reason for the absence of the structure factor peak is because the electron density difference between PS and PMMA phases is not high enough to produce any strong scattered intensity within the very short measurement time. After sputter deposition of 0.2 nm (nominal thickness) of iron, a peak appears at a position of $q_y = 1.46 \times 10^{-1}$ nm^{-1}. This peak is the structure factor peak arisen from the distances between neighboring cylinders of PMMA in the template. The position of the peak corresponds to a real space distance of (43 ± 4) nm. The appearance of this peak can occur only if there is a generation of electron density contrast among the nanostructures present in the template with a regular lateral distance and/or with a regular shape of the structures upon sputter deposition of iron. This means that the sputtered iron creates this electron density difference between the cylindrical domains of PMMA and the matrix PS. This is a clear indication that the sputtered iron atoms deposit preferentially onto the PMMA domains of the template, because PMMA has a polar carbonyl group in the polymer as a side chain. A carbonyl group due to its

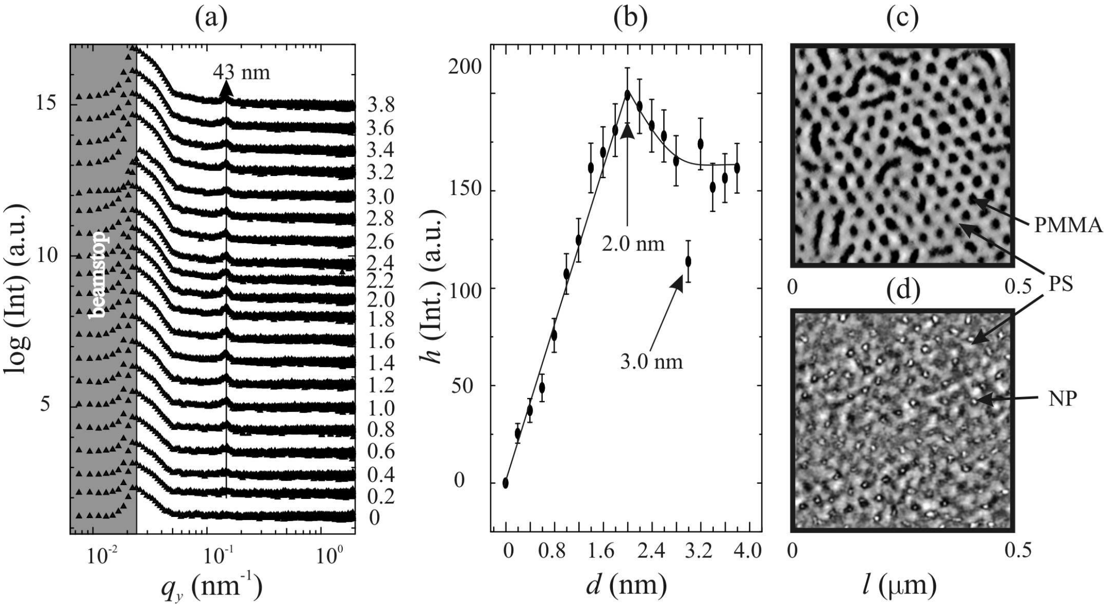

Figure 4.8:
(a) Out-of-plane cuts made from the 2d scattered intensity patterns of all GISAXS measurements during the sputter deposition of iron on PS-*b*-PMMA thin film template. The numbers on the right side of each curve correspond to the nominal thicknesses of sputtered iron in nm. The cuts are shifted vertically for clarity. (b) Height (h) of the peaks at position of $q_y = 1.46 \times 10^{-1}$ nm^{-1} in the out-of-plane cuts in Figure (a) as a function of nominal thickness (d) of iron sputtered on the template. The solid line is a guide to the eyes only. (c) and (d) are the AFM phase images of the used template before and after sputter deposition of 1.6 nm (nominal thickness) of iron, respectively. Iron nanoparticles on in the PMMA domain is visible in (c). l is the length of the image.

strong electrophilic nature attracts the nucleophilic iron atoms. To get more about the nature of the selective wetting of iron atoms in the block copolymer template, the height of the peak at position $q = 14.6 \times 10^{-2}$ nm^{-1} in the out-of-plane cuts are plotted as a function of the nominal thickness of sputtered iron shown in Figure 4.8(b). The intensity of this peak increases linearly with the amount of sputtered iron up to 2.0 nm of iron sputter deposition (nominal thickness). The intensities decrease with further sputter deposition of iron and remain constant after 2.8 nm of iron sputter deposition. This means that iron atoms deposit on the PMMA domains up to a limit (2.0 nm) of nominal thickness of sputtered iron. Further sputtering causes diffusion of iron into the PS matrix causing a decrease of electron density contrast between iron doped PMMA domains and PS matrix. After sputtering of 3.0 nm of iron, lateral structure appears for a short time and disappears after 3.2 nm of iron sputtering. As a result, a large drop of intensity is observed marked by an arrow in Figure 4.8(b). The AFM investigation on the template before and after sputter deposition of 1.6 nm of iron (nominal thickness) was carried out and the phase images are presented in Figure 4.8(c) and 4.8(d), respectively. Iron nanoparticles as the bright objects inside the PMMA cylinders (dark phases) are visible. Formation of nanoparticles occurs as a result of minimization of the surface free energies of iron atoms.

Thus, sputter deposition of iron on a block copolymer template can be used to produce array of magnetic nanoparticles.

1 T. Diederich, S. Couet, R. Röhlsberger, Phys. Rev. B 76, 054401 (2007)

2 P. Müller-Buschbaum, Anal. Bioanal. Chem. 376, 3 (2003)

4.5 Magnetoelastic effects in magnetic nanoparticle diblock-copolymer nanostructures

L. Schulz[1], A. Omran, W. Schirmacher, B. Russ[2], S. Vallopilly[3], P. Böni[2], W. Petry, P. Müller-Buschbaum

[1] Now at Dept. de Physique, Université de Fribourg, Switzerland

[2] Phys.-Dept. TUM. E21

[3] LENS, Indiana University Cyclotron Facility, 2401 Milo B. Sampson Lane, Bloomington, IN 47408, USA

Magnetic properties of thin composite films, consisting of polystyrene-coated γ-Fe_2O_3 (maghemite) nanoparticles embedded into polystyrene-block-polyisoprene (PS-b-I) copolymer films have been investigated. The magnetization measured as a function of external field and temperature show typical features of super-paramagnets including a hysteresis at low temperatures and blocking phenomena, as expected for polydispersive samples. However, the differential magnetic susceptibility depends only weakly on temperature between room temperature and 2K. This strongy contradicts the superparamagnetic model, for which a Curie law is expected. These findings can be explained if a magnetoelastic coupling is assumed, i.e. the applied magnetic field leads to a mechanical torque of the nanoparticles.

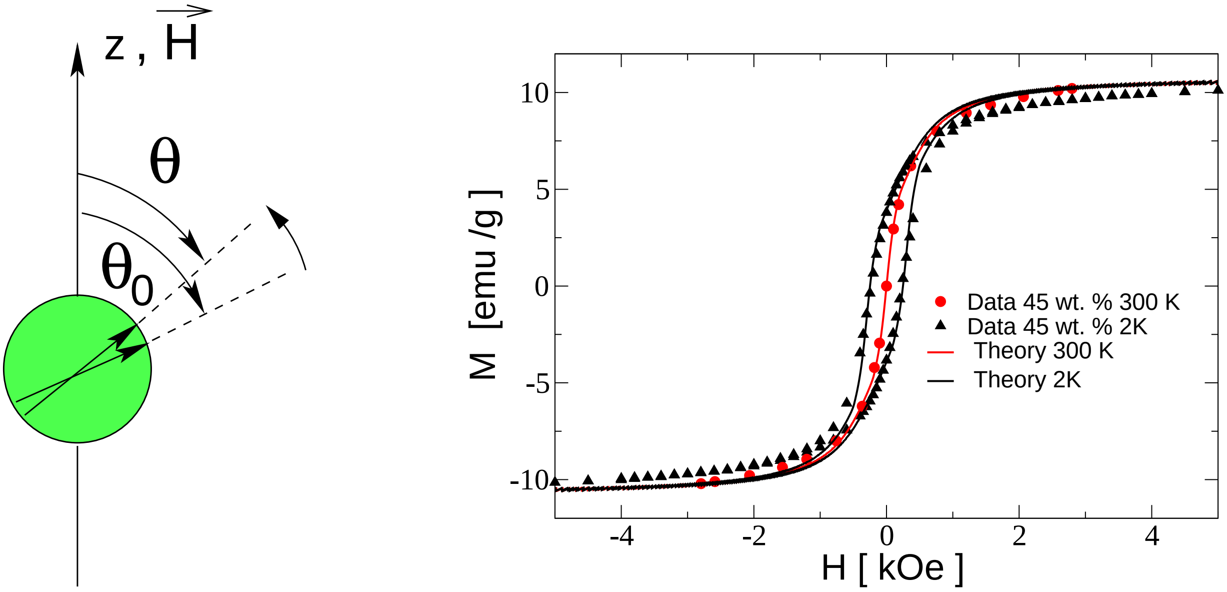

Figure 4.9:
Left: Sketch of the mechanic torque, which leads to a mechanical twist towards the field.
Right: Magnetization curves at T = 300 K and 2 K compared with fits of our torque model

To be able to explain the data we have to assume that the magnetic moments of a part of the particles (the largest ones) are thermally frozen, i.e. can neiter be switched by thermal nor magnetic excitations. The remaining part (the smaller ones) can switch their spins according to the classical superspin blocking model of Stoner, Wohlfarth [1], Néel [2] and Brown [3]. The twist of the immobile spins leads to a temperature-independent magnetic susceptibility, which is inversely proportional to the shear modulus. We extract from our data a shear modulus of $G \approx 1$ MPa, which is about the shear modulus of rubber. Inserting a suitable coercitivity into the equation of states of the mobile spins we are able to nicely fit our magnetization data (see Fig. 4.9).

[1] E. C. Stoner, E. P. Wohlfarth, Phil. Trans. Roy. Soc. **240A**, 599 (1948), reprinted at IEEE Trans. Magn. **27**, 3475 (1991).

[2] L. Néel, Ann Geophys. (CNRS) **5**, 99 (1949).

[3] W. F. Brown, Phys. Rev. **130**, 1677 (1963).

4.6 In situ GISAXS study of gold film growth on conducting polymer films

G. Kaune, M. A. Ruderer, E. Metwalli, S. Couet[1], K. Schlage[1], R. Röhlsberger[1], S. V. Roth[1], P. Müller-Buschbaum

[1] HASYLAB at DESY, Hamburg, Germany

In recent years a new application for metal coatings on polymer films has emerged in the field of organic electronics. Here, a thin metal film is used to apply electrical contact to the active layer of an electronic device, e.g. a light emitting diode (OLED), an organic field effect transistor (OFET) or an organic solar cell. In addition to small organic molecules numerous conjugated polymers are frequently used in the device layout [1]. Among them poly(N-vinylcarbazole) (PVK) is of particular interest [2], due to its outstanding thermal and chemical stability and its ability to form charge transfer complexes.

A thin gold layer was deposited on top of a 10 nm thick PVK film by DC magnetron sputtering and the cluster growth was monitored in-situ with grazing incidence small angle scattering (GISAXS). A deposition rate of only 0.32 nm/min was achieved by a low sputtering power of 3 W and an additional shielding mask. The incident angle was set to 0.8^o (above the critical angle of gold) and a wavelength of 0.138 nm was used. The experiment was performed in a stop-sputtering mode, i.e. each deposition step was followed by a subsequent GISAXS measurement. In total, 49 deposition cycles were carried out and a 15.1 nm thick gold layer deposited. The collected 2D images were simulated with a cluster model to extract morphological parameters such as cluster radius, height and distance. The best results were obtained with a model combining clusters with spheroidal and parallelepipedal shape, where the spatial arrangement of the clusters was calculated based on a 1D paracrystal model. Figure 4.10 shows a comparison of four selected scattering images and the corresponding simulations.

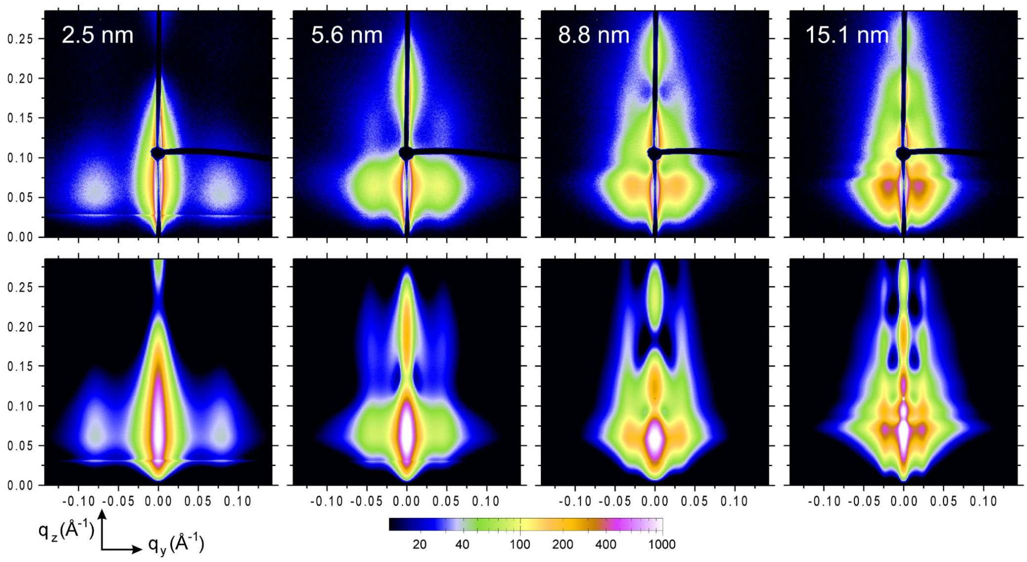

Figure 4.10:
Composite image of four representative measured GISAXS scattering patterns (upper row) and corresponding simulations (lower row). The images were taken at 2.5, 5.6, 8.8, and 15.1 nm thick gold layers.

The modelling procedure was applied to all 2D GISAXS scattering patterns to follow the temporal evolution of cluster size and spatial distribution. The resulting values of cluster height, radius and correlation distance are shown in figure 4.11 as a function of the deposited film thickness. For the cluster height, a nonlinear progress with the deposited gold amount is obvious. Up to a value of 9 nm, the cluster height exceeds the film thickness, proving a 3D growth mode with pronounced height growth in the early stage of cluster formation. The cluster radius increases continuously with deposited gold amount. A similar behavior shows the correlation distance, indicating a cluster growth with permanent coalescence. Three distinct growth regimes with different scaling laws $D \sim d^{\alpha}$ and a transition at a thickness of 1.3 nm are pronounced. For the radius scaling a second transition is visible at a film thickness of 9 nm, the point where complete surface coverage is reached. Afterwards, the radius scaling is identical to the correlation distance scaling.

The results obtained from simulation of the scattering data suggest a cluster growth process proceeding in four stages, with a characteristic kinetic process assigned to each stage (Figure 4.11). In the first stage of nucleation, impinging gold atoms diffuse along the PVK surface and form nuclei [3]. In the second stage, these nuclei grow laterally by capturing adatoms on the surface and gold clusters with a spheroidal shape form. At a point where two clusters get in close contact to each other coalescence occurs and a larger cluster forms. At a layer thickness of 1.3 nm enhanced coalescence sets in, cluster radius as well cluster distance increase very fast and the clusters start to assume an irregular shape (coarsening). In the final stage, a continuous layer has formed and grows further in thickness. Simultaneously, cluster coalescence continues and a grain structure characteristic for vapor-deposited thin films develops [4].

In summary, we investigated the formation of a gold layer on a conductive polymer surface from nucleation to a continuous layer, intending to understand the basic growth mechanism and the principles of cluster morphology evolution, whose knowledge is a prerequisite in a controlled gold film preparation.

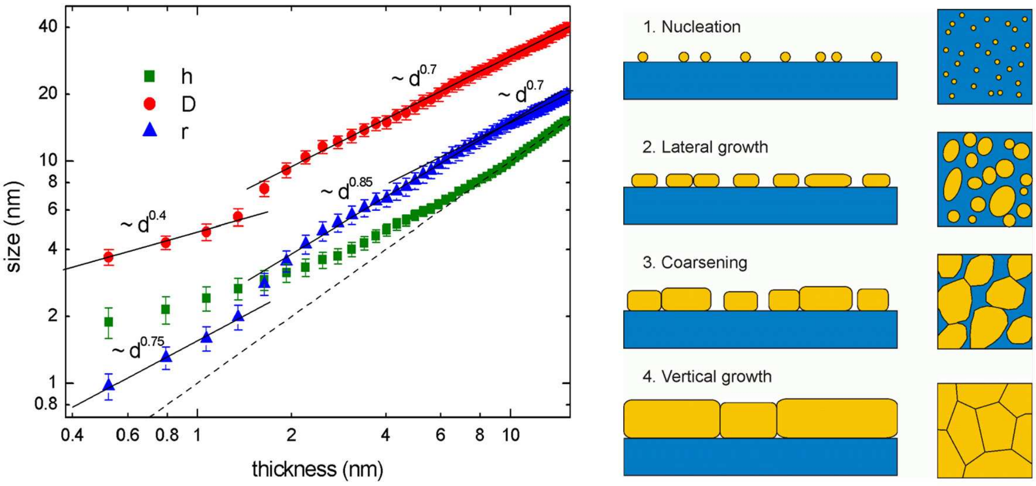

Figure 4.11:
Left: Evolution of cluster height (squares), radius (triangles) and correlation distance (circles) with gold deposition. For the lateral cluster dimensions, distinct growth regimes with characteristic scaling laws are distinguishable. Right: Schematic drawing of the cluster growth process.

[1] C. J. Brabec, N. S. Sariciftci, J. C. Hummelen, Adv. Funct. Mater. **11**, 15 (2001)

[2] G. Kaune, W. Wang, E. Metwalli, M. A. Ruderer, R. Roßner, S. V. Roth, P. Müller-Buschbaum, Eur. Phys. J. E **26**, 73 (2008)

[3] J. A. Venables, G. D. T. Spiller, M. Hanbücken, Rep. Prog. Phys. **47**, 399 (1984)

[4] G. Kaune, M. A. Ruderer, E. Metwalli, W. Wang, S. Couet, K. Schlage, R. Röhlsberger, S. V. Roth, P. Müller-Buschbaum, ACS Appl. Mat. Interfaces **1**, 353 (2009)

5 Biopolymers

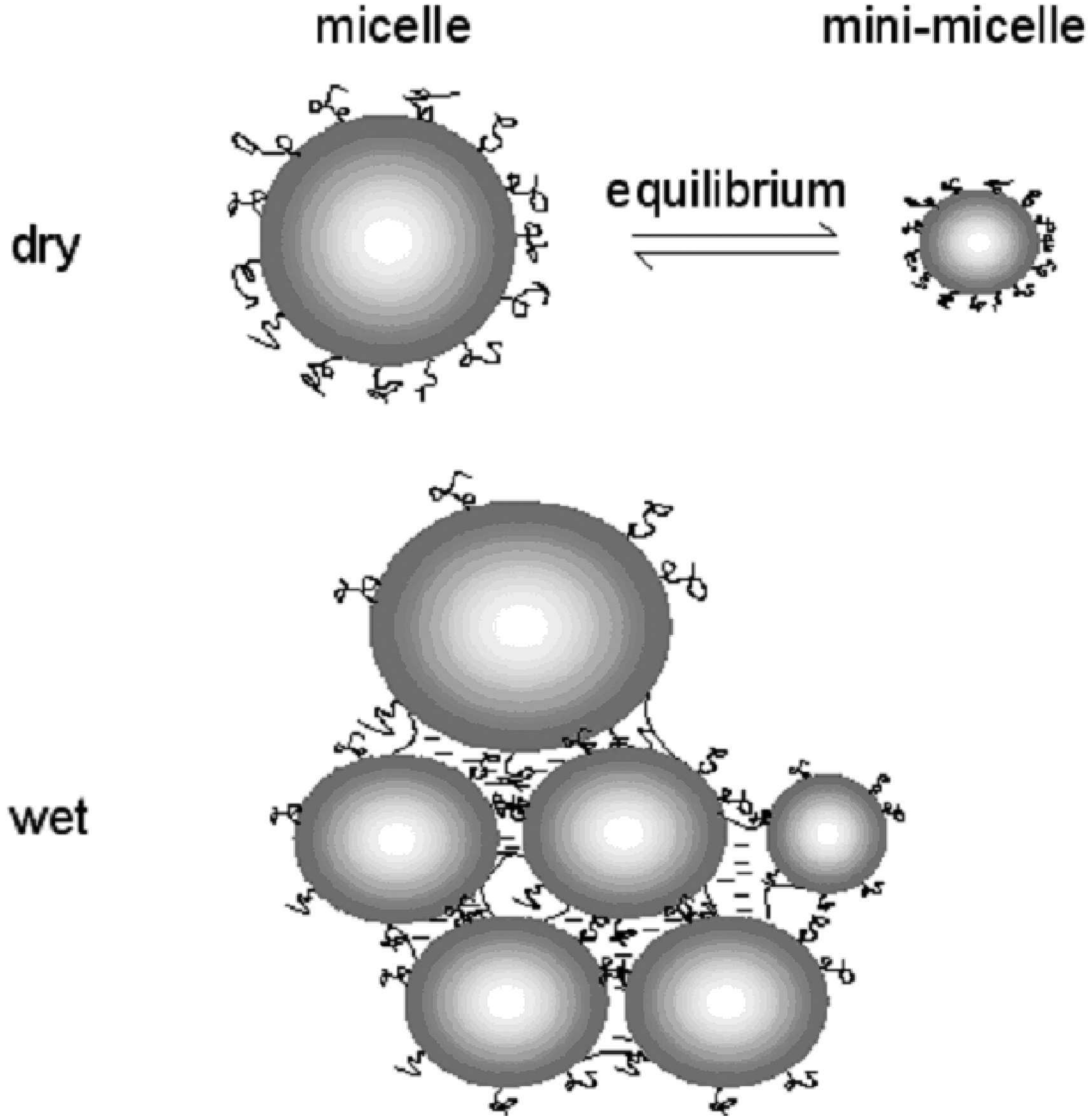

5.1 Dynamics of the Phospholipid DMPC

S. Busch, C. Smuda, L. C. Pardo Soto[1], T. Unruh
[1] Universitat Politècnica de Catalunya

The phospholipid DMPC is an amphiphilic biomolecule which consists of two lipophilic tails and a hydrophilic head which is directly joined to the tails. When put in water, it self-organizes into layers which "hide" the lipophilic tails from the water.

The cells all living beings consist of are in fact nothing else than the space surrounded by such a bend layer. Inside the cell, there are even more compartments which are again separated by phospholipid bilayers summing up to a total membrane surface in a human body of about 5km^2. However, it is not only the vast occurrence in nature that makes phospholipids an interesting subject matter, but also their technological importance. They are widely used in different technological areas, for instance in food industry as stabilizers of dispersions, as e. g. chocolate.

They are also used in pharmaceutical applications. Being endogeneous substances, phopholipids promise to cause no immune reaction and are already approved by the FDA. Their field of application is for example parenteral nutrition or drug delivery. Drug delivery systems became necessary because only about a third of newly discovered drugs are water soluble [1] – leaving the remaining two thirds in need for a drug delivery system if they have to avoid the intestinal tract.

Several pathways are possible, including injection, skin delivery, or inhalation – the number of drug delivery patents increased dramatically in the past ten years. The two most often used drug delivery systems – liposomes and nanoparticles – rely on phospholipids.

Somewhat resembling an empty cell, a single phospholipid bilayer shell is called vesicle, liposomes are multilamellar vesicles. Lipophilic drugs can for example be transported in the lipophilic parts of the phospholipid shells. Nanoparticles contain – as the particles in food industry (where they do not need to be nanometer sized) – a lipophilic core which is stabilized by phospholipids.

We perform a study of the dynamics of the phospholipids on a picosecond time scale with quasielastic neutron scattering at the time-of-flight neutron spectrometer TOFTOF at the Forschungsneutronenquelle Heinz Maier-Leibnitz (FRM II). This dynamics can be imagined to be important for storage or drug release properties, respectively.

A problem of the before-mentioned drug delivery systems which are stabilized only by phospholipids is their unsatisfactory storage stability which can however be enhanced dramatically by the addition of co-emulsifiers such as sodium glyco-cholate. We aim to understand these changes in stability from a molecular point of view, regarding changes in the dynamics.

As the amount of phospholipid in drug delivery systems is very small, we also studied pure phospholipid–D_2O mixtures with large fractions of phospholipid (up to 50%). In these systems, the phospholipid can not only form multilamellar vesicles but also liquid crystals. We used these liquid crystals to study the motions of phospholipid molecules in the membrane in detail.

There are several motions that can occur on our observation time scale. On the one hand, there are localized motions which will also on the long run not macroscopically displace the molecule. On the other hand, there is a long-range motion which moves the center-of-mass of the molecule on a length scale larger than the size of the molecule.

The nature and speed of the long-range motion has been debated in the literature. Some neutron scattering experiments in the 1990s yielded diffusion coefficients which were up to two orders of magnitude larger than the ones measured by macroscopic methods such as fluorescence recovery after photobleaching while others postulated that the long-range motion could not be resolved by quasielastic neutron scattering.

This contradiction was solved by the free volume theory [2] which stated that the phospholipid performs a localized motion in a cage of its neighbours until by chance a gap opens through which the molecule can escape from this cage. The diffusion inside the cage is assumed to be very fast, explaining the neutron scattering experiments.

However, this escape mechanism was never directly observed in molecular dynamics simulations. In a recent study [3], special emphasis was given to this question with the result that rather than escaping from the neighbours, the molecules move collectively with their neighbours.

With incoherent quasielastic neutron scattering, it is not possible to directly probe if a motion is collective or not as the autocorrelation function (mainly of the hydrogen nuclei) is probed.

However, the evaluation of the data including a long-range and two localized motions (which were approximated by two Lorentzians in the scattering function) permits two possible explanations of the long-range motion.

Assuming a flow-like behaviour ($\Delta x \propto v \cdot t$), it is possible to fit the data. Fickean diffusive behaviour would result in a different Q-dependence of the linewidth. However, also a diffusional model can be made to fit the data by introducing an additional parameter, which corresponds to a stop-and-go motion where the go-phases are diffusive.

Comparing the drug delivery systems to these data of liquid crystals is hard due to the dramatically reduced fraction of phospholipid in the sample; it seems however that vesicles exhibit a more diffusive behaviour – but there is virtually no change between a phosphiolipid bilayer (as in the vesicle) to a monolayer (as around a nanoparticle). The addition of sodium glyco-cholate enhances the mobility *of the DMPC* which could be related to its stabilizing effect.

Studies with other additives are in progress. Myristic acid, one of the "tails" of the phospholipid, has been shown to increase the fusion capability of vesicles with cells, presumably increasing the drug release rate. On the contrary, cholesterol is known to decrease the dynamics of the phospholipid membrane which could result in a hindered release.

[1] http://new.pharmacircle.com/

[2] Vaz, Almeida, Biophys. J. **60**, 1553 (1991)

[3] Falck, Róg, Karttunen, Vattulainen JACS **130**, 44 (2008)

5.2 Towards highly ordered casein films on solid supports

R. Gebhardt[1], M. Burghammer[1], C. Riekel[1], U. Kulozik[2], P. Müller-Buschbaum

[1] ESRF, Grenoble, France

[2] TU München, Chair for Food Process Engineering and Dairy Technology, Freising-Weihenstephan, Germany

Casein micelles are colloidal particles of spherical shape with an average diameter of about 100 nm and a large polydispersity. This polydispersity can be approximated by a log-normal-distribution covering a broad range of micelle diamaters. The casein micelle of bovine milk consists of four different phosphor-proteins which can be divided into two groups: the calcium insensitive κ-casein and the calcium sensitive α_{S1}-, α_{S2}- and β-caseins. While the self-associating behavior of individual caseins in aqueous solution has been well investigated, the micellar substructure of casein micelles are still the subject of debate. It is generally accepted that the stability of casein micelles is ensured by an outer hairy layer of κ-caseins.

After investigating the film structure of casein micelles in a gradient of calcium [1] and rennet enzyme [2], we have explored possibilities to achieve highly ordered casein films. In a recent grazing incidence small-angle x-ray scattering experiment with x-ray beam diameters of micron size (μGISAXS) such highly ordered casein films were probed [3]. The increase in order changes the scattering patterns as compared to the normal polydisperse casein film system. In an ordered film, the layer-structure of the casein becomes apparent in the GISAXS patterns by vertical and horizontal Bragg-rods as well as by an indication of Bragg-spots. An example is shown in figure5.1.

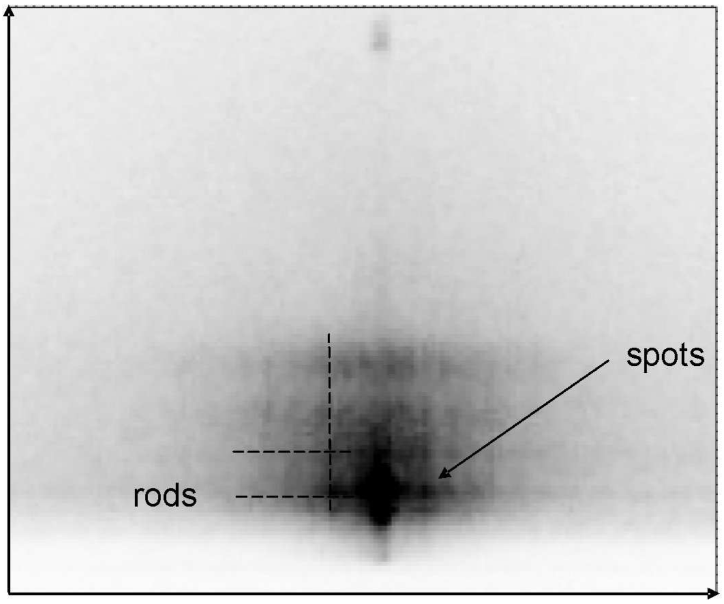

Figure 5.1:
μGISAXS pattern of a structured casein film with Bragg-rods and spots indicated by the arrows. In addition the specular and the Yoneda peak are visible in the central part of the scattering.

For colloidal hard spheres such as casein micelles a face centered cubic packing is indicated by theory while a random hexagonal closed structure is generally observed in experiment [4]. The proper evaluation of the μGISAXS data, which should provide insights in the order of the casein layer, is still in progress.

The batch-wise size sorting of casein micelles was achieved by incremental ultra-centrifugation of the casein solution prior to the film preparation. This centrifuging was performed at the EMBL (Grenoble) using different sets of parameters. By ultra-centrifugation we decrease the heterogeneity of the sample approaching an ideal homogeneous size distribution. The polydisperse system is transferred into a nearly monodisperse one, which is the prerequisite for the installation of highly ordered casein films. In addition of importance is the preservation of the installed size distribution from the ultra-centrifugation during the subsequent processing steps in the thin film preparation.

Beside μGISAXS experiments, ex-situ atomic force microscopy (AFM) measurements were performed in order to get information about the surface morphology. Figure 5.2 shows an AFM image of nearly homogeneous, closely packed casein micellar film. Individual micelles are visualized. However, from the shown AFM image it is difficult to extract the overall degree of order because the method is only sensitive to the film surface and does not provide any information of buried structures.

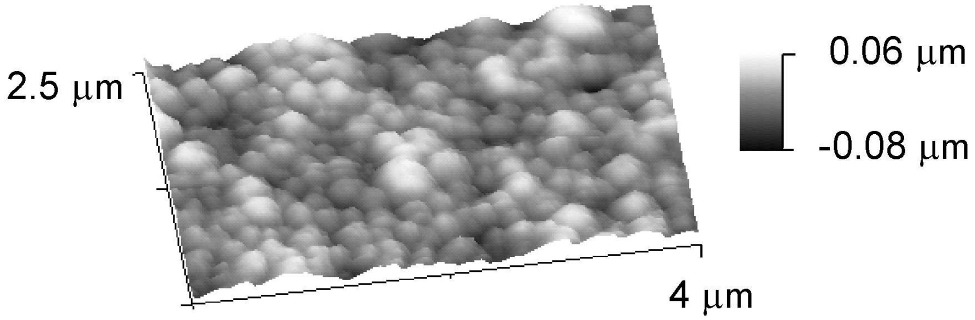

Figure 5.2:
Corresponding casein film topography measured ex-situ with the new ID13 beamline AFM.

In the future there are plans to integrate an atomic force microscope in the μGISAXS- setup of the ID13 beamline in order to perform in-situ experiments. By doing so, highly ordered areas on the casein film surface could be investigated in view of their molecular packing. So far, a vertical one has replaced the previously used horizontal μGISAXS setup [5]. Two crucial benefits of the new setup are, on the one hand the faster exchange between conventional SAXS/WAXS and μGISAXS (because the exhausting displacement of the beamline - microscope holder is avoided) and on the other hand an exact positioning on the focus of the x-ray beam. The latter can be conducted by parallel optical focusing of both, the highly aligned beamline microscope and the μGISAXS microscope on one and the same sample feature. However, this new μGISAXS geometry is restricted to the investigation of dry surfaces.

[1] R. Gebhardt, M. Burghammer, C. Riekel, S.V. Roth, P. Müller-Buschbaum, Macromol. Biosci., **8**, 347 (2008)

[2] R. Gebhardt, S. V. Roth, M. Burghammer, C. Riekel, A. Tolkach, U. Kulozik, P. Müller-Buschbaum, submitted, (2008)

[3] R. Gebhardt, C. Vendrely, M. Burghammer, C. Riekel, S. V. Roth, and P. Müller-Buschbaum, submitted, (2008)

[4] A.V. Petukhov, I. P. Dolbnya, D. G. A. L. Aarts, G. J. Vroege, H. N.W. Lekkerkerker, PRL, **90**, 2, 028304-1 (2003)

[5] R. Gebhardt, M. Burghammer, C. Riekel, S.V. Roth, P. Müller-Buschbaum E13 Annual report, 65, (2007)

5.3 In situ GISANS study of water uptake into thin films of casein micelles

E. Metwalli, J.-F. Moulin[1], R. Gebhardt[2], R. Cubitt[3], A. Tolkach[4], U. Kulozik[4], P. Müller-Buschbaum

[1] GKSS-Forschungszentrum, Geesthacht, Germany
[2] ESRF, Grenoble, France
[3] ILL, Grenoble, France
[4] Chair for Food Process Engineering and Dairy Technology, Freising-Weihnstephan, Germany

Milk and milk components are used to make related food products. One component of milk is casein protein, which plays an important biological role in stabilizing the colloidal form of calcium phosphate in milk and thereby inhibits crystal growth in the secretary cells of the glands [1]. Casein proteins in bovine milk include four main types: α_{1s}-casein (38 %), α_{2s}-casein (10 %), β-casein (36 %) and κ-casein (13%), which are involved in formation of hydrated casein micelles of size on the order of 150-300 nm. Casein-associated water molecules are divided into [2] different classes based on the method used to study the system. In general, for dairy protein systems, they are classified as (i) structural water, i.e., water molecules directly involved in the stabilization of the protein structure; (ii) hydration water, which refers to a monolayer of water molecules that is dynamically oriented and exhibits restricted motion due to a significant decrease in the translational and rotational modes of motion caused by macromolecular-water interactions; and (iii) hydrodynamic hydration water, which is transported with the protein during diffusion in an aqueous solution.

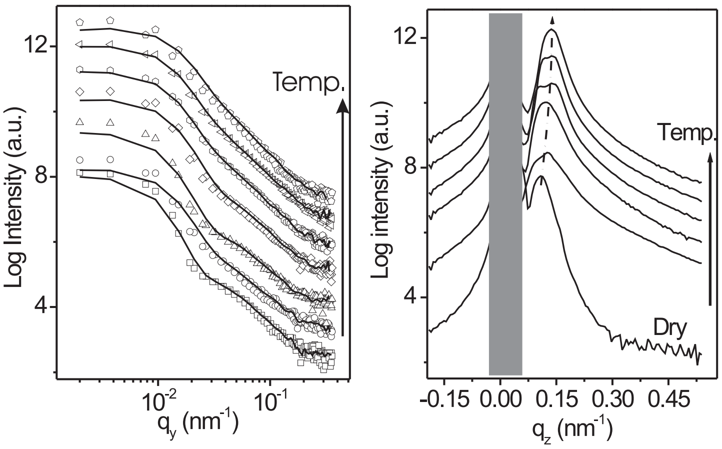

Figure 5.3:
Slices parallel (left) and Slices perpendicular (right) to the sample surface from the 2d GISANS data measured in D_2O at different temperatures (from bottom to top: dry casein protein film; films in water vapor at 30, 40, 50, 60 and 70 °C). For the left graph: Data (symbols) are shown together with the best fit (lines). From the right graph: A shift of the Yoneda peak towards higher q_z values with increasing temperatures (dash curved line) indicates an increase of the amount of incorporated D_2O in the casein protein film.

The extent of the ordering of the monolayer hydration water molecules is quite different from those characterizing the fast and random motion of free or bulk water. In this investigation, we examined the casein-associated water in casein protein films exposed to water vapor rather than in aqueous solutions. Since casein proteins do not denature in their dry format, the preparation of casein micelles in a thin dry film is possible with spin coating [3]. Studying the casein micelle in its dry format and its interaction with water vapor without exposing the protein to direct contact with an aqueous medium overcomes some of the limitations in other techniques. The water content of the casein micelle films in water-vapor atmosphere is investigated using time-resolved grazing incidence small-angle neutron scattering (GISANS). Using the GISANS technique and introducing contrast with the use of deuterated water vapor we successfully studied the kinetic of the water uptake at 30 °C and detailed the structure inside the D_2O vapor-equilibrated protein films. At 30°C a total water content of about 0.36 g water/ g protein is found. This value of the water incorporated into the casein protein film is an intermediate value between previously-reported values using solution-based experimental methods such as SAXS and NMR. The increased amount of water uptake as a function of water-vapor temperature indicated a continuous structural reorganization (Figure 5.3) of the film due to the correspondingly new equilibrium conditions. Structural changes upon swelling with water are identified and attributed to the hydration layer around the micelles. Modelling of the GISANS data is performed in the framework of an approach using two objects of spherical shape, but different sizes. Figure 5.4 shows the progressive particle radius changes with increasing of water contents. Upon water uptake, assemblies of protein molecules in the size range of 15 nm (mini-micelle) is observed and attributed to the formation of high contrast D_2O outer shell on the small objects that already exist in the protein film. For the large objects (>100 nm), the mean size increases at high D_2O vapor temperature because of possible aggregation between hydrated micelles. Mini-micelles aggregation by water bridges between neighboring ones forming large objects is schematically represented in Figure 5.4 [4].

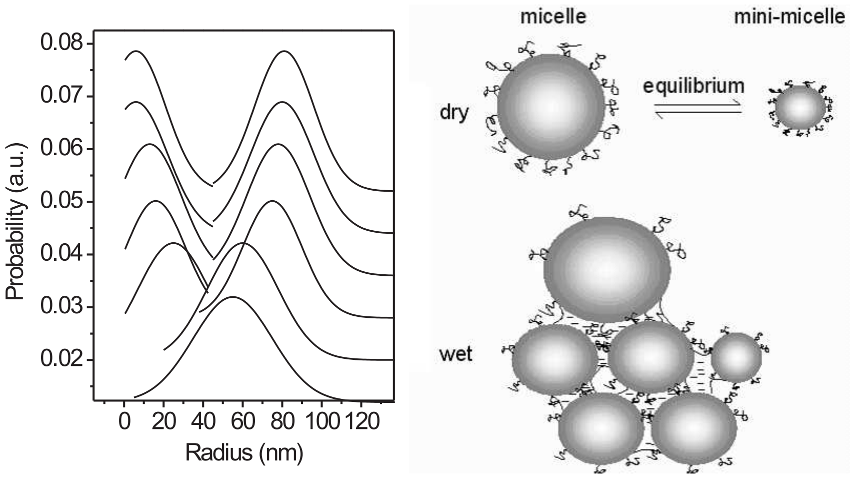

Figure 5.4:
Result of the fitting is the radius and radius distribution of the two assumed objects (left). The samples from bottom to top: dry casein protein film; films in water vapor at 30, 40, 50, 60 and 70 °C. The curves are shifted along the y-axis and some of the data points at the zero probability are removed for clarity of the presentation. Schematic model (right) explaining the coexistence of standard micelles and mini-micelles (dry) and the formation of micelle aggregate upon water-vapor uptake by association of different size micelles (wet).

[1] C. Holt, *In Developments in Dairy Chemistry-3*, Elsevier, London (1985).

[2] J.E. Kinsella, CRC Crit. Rev. Food Sci. Nutr. **21**, 197 (1984)

[3] P. Müller-Buschbaum, R. Gebhardt, E. Maurer, E. Bauer, R. Gehrke, W. Doster, Biomacromolecules **7**, 1773 (2006)

[4] E. Metwalli, J.-F. Moulin, R. Gebhardt, R. Cubitt, A. Tolkach, U. Kulozik, P. Müller-Buschbaum, Langmuir, ASAP article, (2009)

6 Dynamics in soft matter

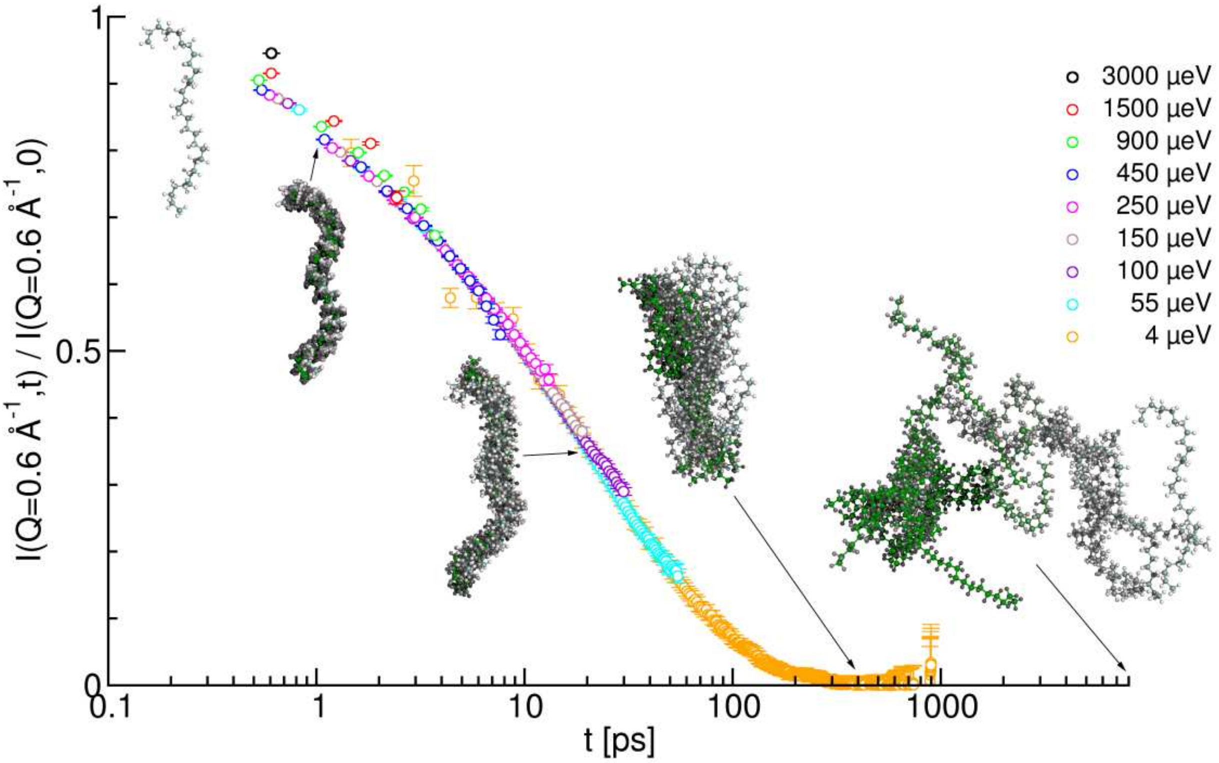

6.1 Proton dynamics in hydrous sodium trisilicate melt

F. Yang, A. Meyer[1], T. Unruh, J. Wuttke[2]

[1] Institut für Materialphysik im Weltraum, DLR, 51147 Köln
[2] Jülich Center for Neutron Science, FZ-Jülich, Aussenstelle am FRM II, 85748 Garching

Dissolved water in silicate melts plays an important role in many geological processes. In nature several weight % of water can be stably dissolved in silicate melts at high temperature under high pressure in the magma chamber. Decompression of such a melt during ascent to the earth surface is a major mechanism which constitutes active volcanism. The addition of water to silicates is known to result a drastic, non-linear drop of the melt viscosity by many orders of magnitude.The relaxation behaviour of the melt determines the volcanic eruption style, which is controlled by the degassing kinetics of the water. Therefore, the knowledge of the dynamics of water in the silicate melts represents an essential key to predict the properties of the melts [1]. However to understand the relaxation behaviour of the melt two important questions still need to be addressed: 1) The dissolution mechanism of water in silicate melts; 2) The diffusion mechanism of water components in the melt.

We performed high temperature high pressure quasielastic neutron scattering experiment which allows direct observation of water dynamics in hydrous silicate melt on a microscopic scale under magma chamber conditions. The investigation benefits from neutron scattering techniques from two aspects: neutron has large penetration depth in metals so even with the massive pressure cell an acceptable signal-to-background ratio can be still obtained; it is isotope sensitive and with a contrast variation via H_2O/D_2O substitution pure proton information can be extracted.

High temperature high pressure experiments have been conducted at the neutron time-of-flight spectrometer TOFTOF at FRM II. Left panel in Fig.6.1 shows the measured intermediate scattering function $S(q,t)$ of the proton in hydrous sodium trisilicate melt at 1150 K, obtained by subtraction of the D_2O sample signal from the H_2O sample signal. The intermediate scattering function can not be described by an (stretched) exponential function, like that of the sodium in dry sodium silicate melts [2]. Instead two unusual characters can be identified. First the signal exhibits extreme stretching, which is best described by a logarithmic decay. Second the signal does not fully decay to zero. It has a slow component which is represented by a constant $f^2(q)$ at large time and its decay is out of the current time window.

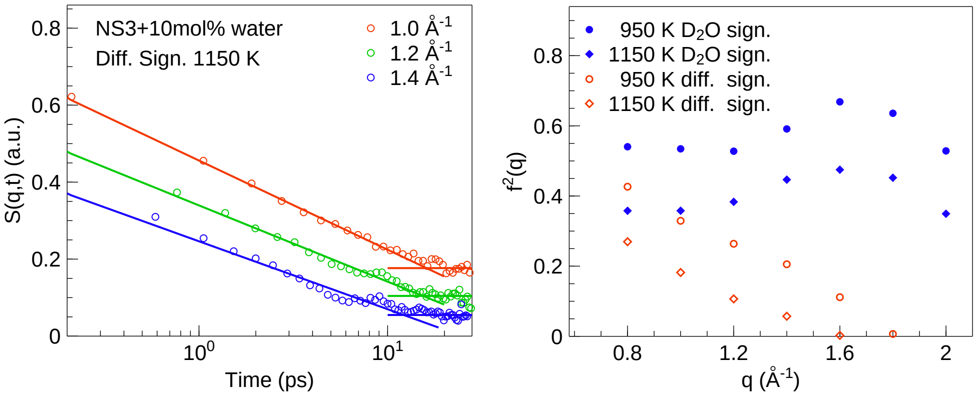

Figure 6.1:
Intermediate scattering function of the pure proton dynamics in hydrous sodium trisilicate melt. Left: Fitting the spectra with a logarithmic decay plus a non-zero constant value $f^2(q)$ at 1150 K and different q values. Right: q dependence of the plateau value $f^2(q)$ for different temperatures, all of them show smooth decay. Values from the D_2O sample are shown for comparison.

Dissolved water is known to partially react with the silicate matrix via following reaction

$$2SiO_2 + H_2O \rightarrow 2SiOH \tag{6.1}$$

which results two different dissolved forms: -OH and H_2O. However as it can be seen that the q dependence of the slow component $f^2(q)$ only shows a smooth decay (Fig.6.1 right panel). An assignment of the slow component to molecular water cannot be satisfied, since otherwise structure features in the $f^2(q)$ from water would be expected. Our observation shows no evidence of different proton environments in the melt.

Mode coupling theory predicts dynamics of logarithmic like decay to be a result of different competitive arrest mechanisms. This has been shown already on the calculations of binary hard spheres mixtures with a sufficient large size disparity, for example in colloid systems or dry sodium trisilicate melts [3-4]. Our results have shown qualitatively similar feature to the theory predictions. Therefore, this is a possible explanation of the mechanisms existing in hydrous sodium trisilicate melt. In such scenario, smaller size particles like proton can still diffuse in the immobile large particle matrix like Si-O before the complete system frozen in, resulting a glass-glass transition.

To verified such interpretation it is necessary to study the long time relaxation behaviour of the system. Mode coupling theory predicts the final decay of the intermediate plateau value $f^2(q)$ towards zero to be a stretched exponential function. In order to study such decay, measurement were performed on the neutron backscattering spectrometer SPHERES at FRM II. Neutron backscattering instruments can provide energy resolutions down to sub μeV range which gives access to ns time scale. However, neutron backscattering is inherently a flux limited technique, neutrons pass the sample and its environment twice before being detected. As it could be seen from Fig.6.2 that no quasielastic broadening can be quantitatively resolved due to the high background created by the cell (note that the spectra have not been corrected for the background yet), only a decrease of the elastic intensity can be observed with increasing temperature.

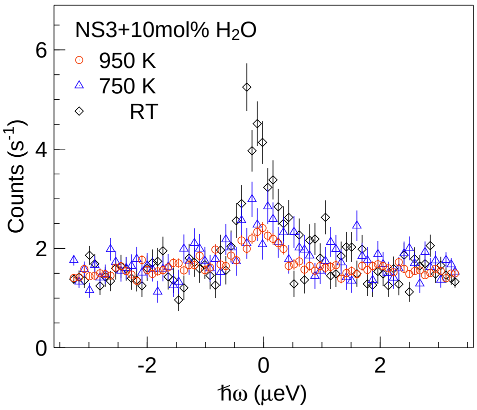

Figure 6.2:
Measured spectra of a hydrous sodium trisilicate sample at room temperature, 750 K and 900 K at the backscattering spectrometer SPHERES with a Doppler driver speed of 0.5m/s. No quasielastic broadening can be quantitatively resolved due to the high background, especially at elevated temperatures where the elastic intensity was low. Higher neutron flux would be necessary in order to study the dynamics in such kind of experiments.

In conclusion an unusually relaxation behaviour of the protons in hydrous sodium trisilicate melts has been found, which exhibits a logarithmic decay to an intermediate plateau value. The result could be explained within the frame work of mode coupling theory by a double glass transition scenario. Further investigation at the larger time scales will give a verification of such interpretation.

[1] D. B. Dingwell, Geological Society, London, **145**, *Recent progress in the experimental determination of magma properties relevant to explosive volcanism*, (1998); edts: J. S. Gilbert and R. S. J. Sparks.

[2] F. Kargl, A. Meyer, M. M. Koza, H. Schober, Phys. Rev. B **74**, 014304 (2006).

[3] A. J. Moreno, J. Colmenero, J. Chem. Phys. **124**, 164507 (2006) and Phys. Rev. E **74**, 021409 (2006).

[4] Th. Voigtmann, J. Horbach, Europhys. Lett., **73**, 459 (2006).

6.2 Molecular motions in pharmaceutical products — Research at TOFTOF

T. Unruh, C. Smuda, S. Busch

The TOFTOF team (cf. Fig. 6.3) can look back on a very successful year 2008. Except for two weeks the spectrometer was operational for all of the 251 days of reactor operation. In this time more than 50 scientific research projects could be executed from which 29 were performed by external groups. Furthermore, 23 original contributions related to measurements performed at TOFTOF were submitted to peer reviewed journals in 2008 from which 16 are already published. Some of the inhouse research projects were initiated by the soft matter group at the spectrometer. These activities will shortly be introduced in this contribution.

Figure 6.3: The TOFTOF team in front of the TOFTOF detector chamber

Our research is focussed on studies of motions and the spatial arrangement of organic molecules in dispersions used in pharmacy as carrier systems for drug delivery but also in food or other industries. Our recent studies included experiments on the dynamics of liquid (bulk and dispersed) phases of simple molecules like oils or fats but also on the motions of stabilizer molecules or other additives as for instance drug molecules in pharmaceutical formulations. From these studies a better insight to the transport mechanism of the molecules in simple molecular liquids and phospholipid mono- and bilayers could be achieved. The understanding of the microscopic structure and dynamics should help to optimize macroscopic physicochemical properties of, e.g., parmaceutical products such as drug release rate or dispersion stability [1].
Already with the first quasielastic time-of-flight neutron scattering (TOF-QENS) experiments it could be demonstrated for the pharmaceutical formulation of coenzyme Q_{10} in the form of nanodroplets stabilized by phospholipids in an aqueous phase that QENS is best suited to study the dynamical properties of molecules inside the nanosized droplets of dispersions [2]. It was, however, found that the dynamics of medium-sized organic molecules in the liquid state is not well understood. Therefore, systematic studies on the picosecond dynamics as probed by TOF-QENS of medium-chain molecules like Q_{10} and n-alkanes were performed [3]. Using the combination of QENS and molecular dynamics (MD) simulations, different diffusive motions could be disentangled ranging from fast tumbling of CH_2-groups to the long range molecular diffusion (cf. Fig. 6.4) [4]. Despite the rod like shape of the molecules the center-of-mass diffusion was found to be essentially isotropic.
Due to the fact that in many organic molecules CH_3-group rotation contributes significantly to the QENS signal, this special local motion has been studied in detail [5]. It could be demonstrated that CH_3-group rotation can be extrapolated from low temperatures of the glassy state to the liquid state by the Arrhenius behavior of the rotational diffusion coefficient. In the liquid state the CH_3-groups rotate free of barrier.

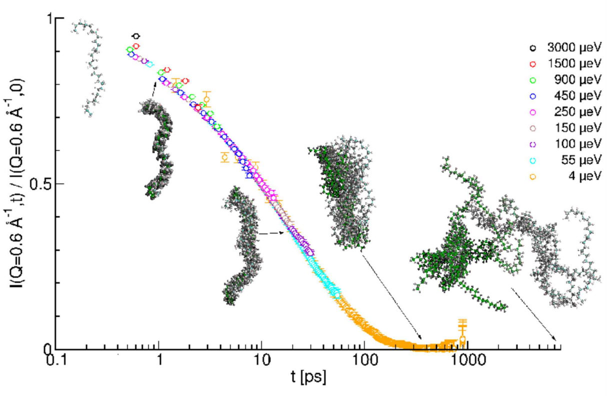

Figure 6.4:
Intermediate scattering function of the n-alkane $C_{32}H_{66}$ at 90°C measured with the TOFTOF spectrometer and using the labeled instrumental resolutions (FWHM of the elastic line). Representative tajectories of a single molecule as extracted from MD simulations of the same liquid alkane are plotted for time ranges between 0ps and 1ps, 20ps, 400 ps and 8 ns, respectively. The time evolution is indicated for each picture by color intensification. For each picture 20 snapshots of the molecule equdistant im time are overlayed.

From TOF-QENS studies of phospholipid (DMPC) liquid crystals, vesicles, and emulsions stabilized by DMPC an evidence was found that the long range motion on a picosecond time scale has a flow-like character. This result confirms recent MD simulations experimentally and adds another piece of knowledge to the understanding of lateral diffusion of molecules in membranes. The interpretation of the dynamics of phospholipid molecules in the stabilizing layer of emulsions is difficult without the knowledge of the structural arrangement of the molecules. For this purpose a special evaluation method of small angle X-ray scattering (SAXS) experiments has been developed and first results for phospholipid layers surrounding solid triglyceride nanoparticles have been achieved [6]. The continuation of this project is now supported by the DFG for three years and a collaboration with the Department of Pharmaceutical Technology of the Technische Universität Braunschweig has been established in order to correlate our results with pharmaceutical parameters of relevant pharmaceutical systems.

[1] H. Bunjes, T. Unruh, *Characterization of Lipid Nanoparticles by Differential Scanning Calorimetry, X-Ray and Neutron Scattering,* Advanced Drug Delivery Reviews **59** (2007) 379–402

[2] T. Unruh, C. Smuda, G. Gemmecker, H. Bunjes, *Molecular dynamics in pharmaceutical drug delivery systems - The potential of QENS and first experimental results,* Quasi-Elastic Neutron Scattering Conference 2006 (QENS2006), eds: P. E. Sokol, H. Kaiser, D. Baxter, R. Pynn, D. Bossev and M. Leuschner, Mater. Res. Soc., Warrendale, PA, 2007, pages 137-145

[3] C. Smuda, S. Busch, G. Gemmecker, T. Unruh, *Self-diffusion in molecular liquids: medium-chain n-alkanes and coenzyme* Q_{10} *studied by QENS,* J. Chem. Phys. **129** (2008) 014513

[4] T. Unruh, C. Smuda, S. Busch, J. Neuhaus, W. Petry, *Diffusive motions in liquid medium-chain* n*-alkanes as seen by quasielastic time-of-flight neutron spectroscopy,* J. Chem. Phys. **129** (2008) 121106

[5] C. Smuda, S. Busch, B. Wagner, T. Unruh, *Methyl group dynamics in glassy, polycrystalline and liquid coenzyme* Q_{10} *studied by quasielastic neutron scattering,* J. Chem. Phys. **129** (2008) 074507; C. Smuda, G. Gemmecker, T. Unruh, *Quasi-elastic and inelastic neutron scattering study of methyl group rotation in solid and liquid pentafluoroanisole and pentafluorotoluene,* J. Chem. Phys. **128** (2008) 194502; C. Smuda, S. Busch, R. Schellenberg, T. Unruh, *Methyl group dynamics in polycrystalline and liquid ubiquinone* Q_0 *studied by neutron scattering,* J. Phys. Chem. B **113** (2009) 916

[6] T. Unruh, *Interpretation of SAXS Patterns of Crystalline Triglyceride Nanoparticles in Dispersion,* J. Appl. Cryst. **40** (2007) 1008-1018

6.3 The influence of the anharmonic interaction on sound attenuation in glassy systems

C. Tomaras, W. Schirmacher

We investigate a 3-dimensional continuum model for vibrational excitations in a disordered environment, based on the anharmonic generalisation of Lame's elasticity theory:

$$\mathcal{L} = \frac{\rho}{2}\partial_t \mathbf{u}(\mathbf{r},t)^2 - \tfrac{\lambda}{2}\, u_{ii}^2(\mathbf{r},t) - \mu(\mathbf{r})\, u_{ij}(\mathbf{r},t)u_{ij}(\mathbf{r},t) + \mathcal{L}_{int} \tag{6.2}$$

$$\mathcal{L}_{int} = \mu \sum_{ijl} u_{ij} v_{il} v_{lj} + g \sum_i u_{ii}^3 \tag{6.3}$$

u_{ij}, v_{ij} are the usual strain- and rotation-tensors of elasticity theory and λ and μ are Lamé's elastic constants.

The disorder is introduced into the theory via a spatially correlated fluctuating shear modulus [1] $\mu(\mathbf{r}) = \mu_0 + \delta\mu(\mathbf{r})$, which fulfils the following statistical properties:

$$\langle \mu(\mathbf{r}) \rangle = \mu_0, \;\; \langle \delta\mu(\mathbf{r})\delta\mu(0) \rangle = (\mu_0)^2 \gamma \exp -|\mathbf{r}|/\xi \tag{6.4}$$

K is the correlation function. $\gamma = \langle (\delta\mu)^2 \rangle / (\mu_0)^2$ is the relative variance of the fluctuation. We call this parameter "disorder parameter". It has been shown by a mean-field treatment [2,3,4,5] that the low-frequency Brillouin linewidth (sound attenuation coefficient) obeys a Rayleigh law $\Gamma(\omega) \propto \omega^4$ in the case of zero anharmonicity $\mathcal{L}_{int} = 0$, the density of vibrational states exhibits the well known boson peak.

The anharmonic interaction $\mathcal{L}_{int}$ provides an additional scattering mechanism for the effective disordered phonons, which can be visualized by common quantum-field theoretical methods [6] in terms of the so called "fish"-diagram Fig. 6.5.

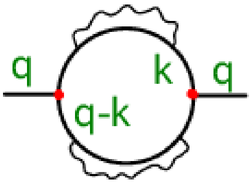

Figure 6.5: basic anharmonic interaction diagram

For low frequencies we obtain an Akhiezer-like sound-attenuation law $\Gamma(\omega) \propto T\omega^2$ Fig. 6.6.

The same effect leads to a temperature dependent enhancement of the excess density of states $g(\omega)/g_{Debye}(\omega)$, which is observed in Neutron and X-ray scattering experiments at frequencies below the boson peak. The theory is in qualitative good agreement with the experimental data of Chumakov et. al. [7] Fig. 6.7.

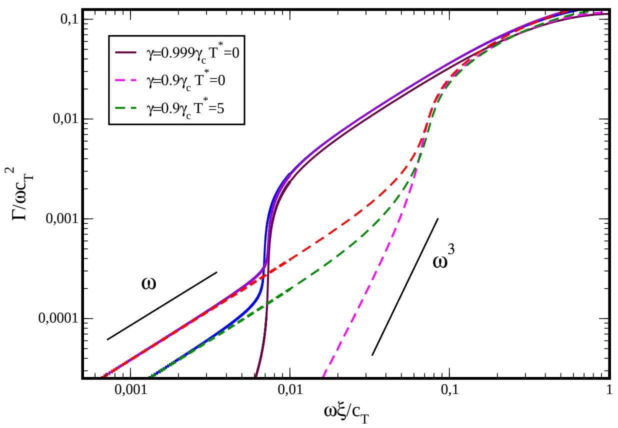

Figure 6.6:
The anharmonic interaction yields a crossover from an Akhizer-like $\Gamma \propto T\omega^2$ to a disorder-induced Rayleigh law $\Gamma \propto \omega^4$

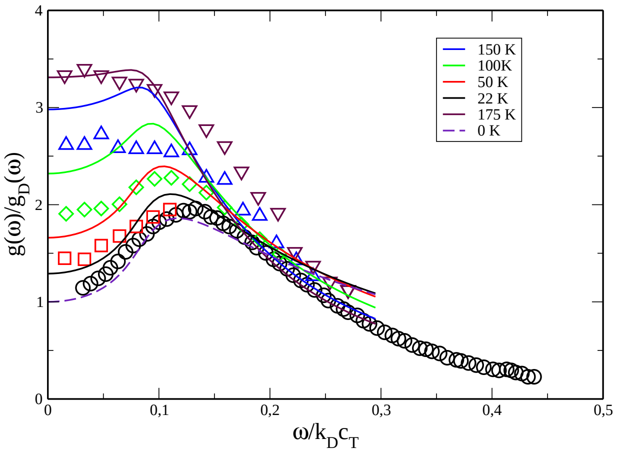

Figure 6.7:
Experimentally obtained normalised density of states from Chumakov et. al. [4] for dibutyl phthalate versus the present theory

[1] W. Schirmacher, B. Schmid, C. Tomaras, G. Viliani, G. Baldi, G. Ruocco, T. Scopigno, phys. stat. sol. (c) **5**, 862 (2008).

[2] W. Schirmacher, Thermal conductivity of glassy materials and the "boson peak", Europhys. Lett. 73(6), 892, 2006.

[3] W. Schirmacher, G. Ruocco, T. Scopigno, Phys. Rev. Lett. **98**, 025501 (2007).

[4] B. Schmid, W. Schirmacher, Phys. Rev. Lett. **100**, 137402 (2008).

[5] B. Schmid, Diploma thesis TU München 2007.

[6] C. Itzykson, J.M. Drouffe, Statistical Field Theory, volume 2, Cambridge University Press, 1989.

[7] A.I. Chumakov et. al., Phys. Rev. Lett. 92, 245508, 2004.

6.4 The diffusion of fluorescence-labeled polyelectrolytes in thin liquid films

N. Kristen[1], R. von Klitzing[1], K. Troll, T. Hoppe, C.M. Papadakis
[1] Stranski-Laboratorium, Institut für Chemie, TU Berlin

Polyelectrolytes play an important role in colloid science and are a good model for complex molecules like DNA or proteins. We study the effects due to geometrical confinement by investigating the diffusion of polyelectrolytes in thin films between two solid supports in comparison to the diffusion in bulk solution [1].

In the present work, the positively charged linear polymer poly(allylaminehydrochloride) (PAH) was used (Fig. 6.8a), having a molecular weight of 56000 g/mol which corresponds to 540 monomer units. To investigate the diffusion behavior with fluorescence correlation spectroscopy (FCS), the polyelectrolyte was labeled with one rhodamine B molecule per polymer (Fig. 6.8b). A simple way to create thin films is to trap the polyelectrolyte solution between two glass slides using polystyrene beads with a defined diameter as spacers [2], see Fig. 6.8c.

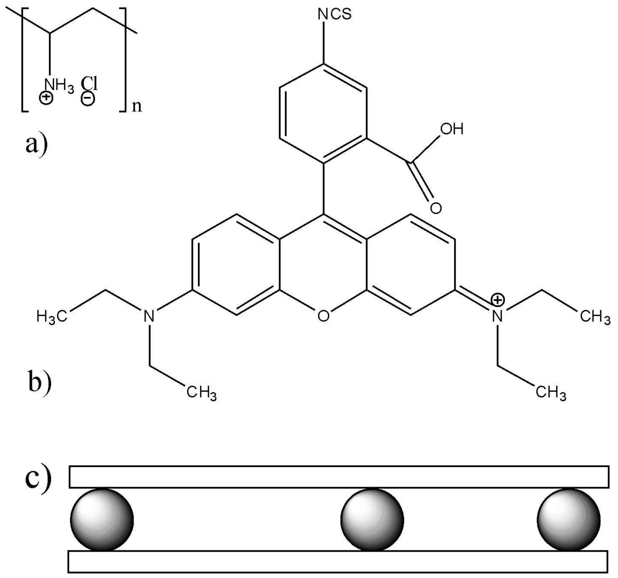

Figure 6.8:
(a) Structure of PAH, (b) structure of rhodamine B, (c) sketch of spacers between two glass slides.

To prevent the adsorption of the positively charged polyelectrolyte at the negatively charged glass slides, it is important to modify the surface. Therefore, the glass slides were silanised by dipping them into an aminosilane solution prior to the experiment [3]. Additionally, the viscosity of the polymer solution was varied by adding different amounts of glycerol which leads to slower diffusion times and thus lower diffusion coefficients. In a first approach, the films had a thickness of 50 μm. Using FCS, it was shown that the polyelectrolytes were equally distributed over the entire film thickness.

The addition of 10 % glycerol has almost no impact on the diffusion coefficient, D, whereas adding 50 % glycerol to water results in a significant decrease from $D = 1.05 \times 10^{-9}$ m^2/s in pure water to $D = 0.36 \times 10^{-9}$ m^2/s in the 50 % mixture (Fig. 6.9). The comparison of the bulk measurements to the results of the measurements in confined geometry shows that a thickness of 50 μm is too large to have an effect on the diffusion coefficient. Furthermore, there is no difference between the diffusion in the film center and the one close to the film/glass interfaces. In the future, we will focus on modifying the FCS method in such a way that thinner films are accessible.

The project is funded by DFG within the priority program "Polymer-Solid Contacts: Interfaces and Interphases".

[1] D. H. Rapoport, D. F. Anghel, G. Hedicke, H. Möhwald, R. v. Klitzing, J. Phys. Chem. C **111**, 5726 (2007)

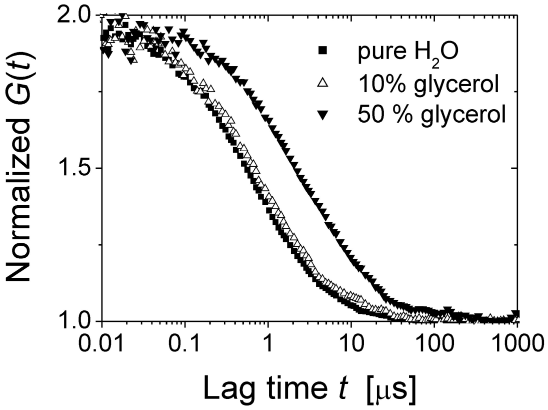

Figure 6.9:
Normalized FCS autocorrelation functions of fluorescence-labeled PAH in water/glycerol mixtures.

[2] A. Serghei, F. Kremer, Rev. Sci. Instrum. **77**, 116108 (2006)

[3] E. Metwalli, D. Haines, O. Becker, S. Conzone, C. G. Pantano, J. Colloid Interface Sci. **298**, 825 (2006)

7 Methodological and instrumental developments

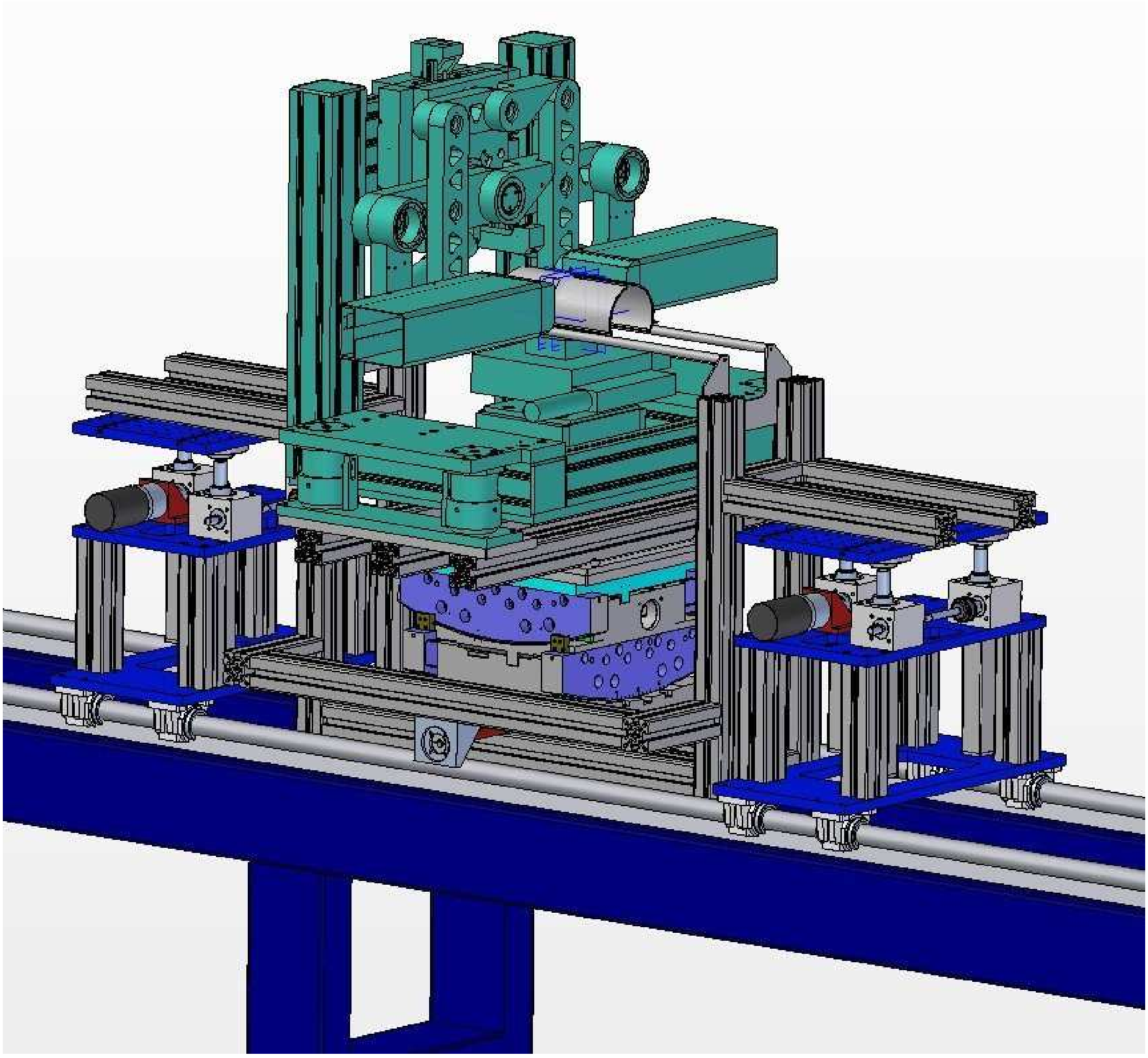

7.1 Flow behavior of a simple liquid: Small droplets on an inclined solid support

D. Magerl, V. Körstgens, P. Müller-Buschbaum

The shape and the flow behavior of small droplets of a simple liquid vary with the contact angle. On a support with a large contact angle the droplet of a simple liquid almost remains in its circular shape while flowing down as shown in figure 7.1a for a droplet of toluene on polydimethylsiloxane (PDMS) grains deposited on a Si-support. By contrast a droplet of approximately the same volume gets a very long tail when the contact angle is very low and the droplet wets the surface as shown in figure 7.1b+c for an acid cleaned Si-wafer. The tail is evaporating rather than flowing down the incline.
Within the present work we focus on the volume dependence of the velocity of small droplets (below 5 μl) on an inclined support. In order to get the volume of the droplet it turned out not to be sufficient to use the volume measured with the syringe or micro-pipette because there is always a small amount of liquid remaining on the tip rather than being deposited on the support. Therefore both, the volume and the velocity of the droplet, have to be determined after the droplet is deposited on the support. The reproducible preparation of surfaces of the incline turned out to be of crucial importance. Even small impurities caused differences in droplet shape and velocity.

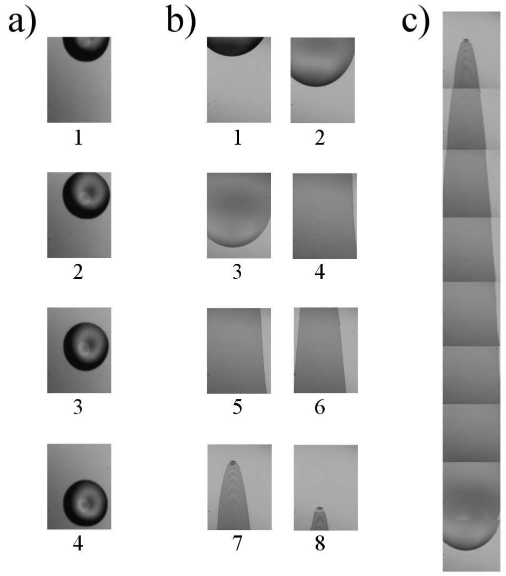

Figure 7.1:
Droplet shapes on a 10° incline: a) moving droplet on PDMS grains deposited on Si-support, time from first to last image: 41 s, b) moving droplet on an acid cleaned support, time from first to last image: 175 s, c) reconstruction of a complete droplet on an acid cleaned support with a pronounced (evaporating) tail.

The setup as it is shown in figure 7.2 consists of a slope where the support is placed and that can be tilted from 0° (horizontal) to 10°. The measurement is realized with two cameras. One camera is mounted perpendicular to the surface when it is horizontal (Fig. 7.2a) to capture the contour and therewith the contact area of the droplet, the other camera is used to measure the velocity of the droplet when the system is tilted (Fig. 7.2b). The investigated droplet volume covers a from 0.3 μl to 5 μl. We used pure toluene as liquid to form the droplets. In order to prevent the toluene droplet from evaporating during the experiment, a saturated toluene atmosphere was installed. This atmosphere is produced by some vials filled with toluene and toluene soaked tissues for an increased surface. The support used is an acid cleaned silicon (Si) substrate.
In the experiment a freshly cleaned Si substrate is put on the slope and the toluene atmosphere around the Si substrate is saturated. Next the system is tilted to the 0° state and a toluene droplet

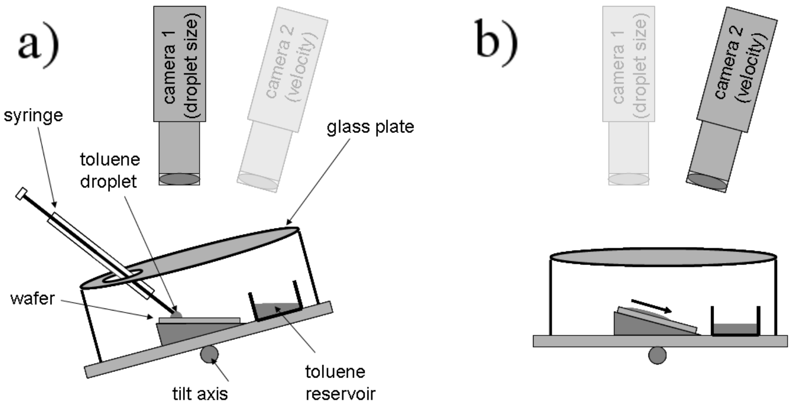

Figure 7.2:
Sketch of the setup a) droplet deposition and measurement of contact area, b) measurement of velocity after the system has being tilted

is deposited in the focus of the first camera with a microliter syringe through a small hole in the glass plate that covers the system. After the deposition the syringe is put out again, the hole is closed and the first camera takes an image of the droplet on the support. From this image the contact area is determined. Then the system is tilted by 10° and the droplet starts moving down. The second camera takes a movie of the flowing droplet on a length of about 4 mm. The observable space is limited to 4 mm because of the used magnification of the microscope. Movies are captured with a frame rate of 117 frames per second. The velocity of the droplet is determined at its front with the time-code of single frames.

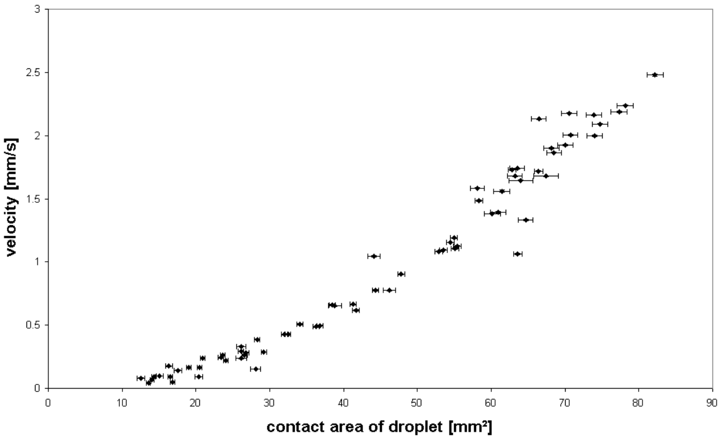

Figure 7.3: Velocity of toluene droplets on an inclined surface of 10°against their contact area.

Experimentally there is a lower limit on the area where the droplet is still moving as shown in figure 7.3. The velocity increases with the area to the power of 1.5, which indicates a linear increase of velocity with volume.
Future work on this topic will include conversion of contact area to droplet volume and analysis of different surfaces. It is of great interest how the experimental data fit to the predictions from simulations [1, 2].

[1] C. Servantie and M. Müller, J. Chem. Phys. 128, 014709 (2008)

[2] J. Servantie and M. Müller, Phys. Rev. Lett. 101, 026101 (2008)

7.2 Flow at interfaces: a new device for x-ray surface scattering investigations

J-.F. Moulin[1], S .V. Roth[2], P. Müller-Buschbaum

[1] GKSS-Forschungszentrum, Geesthacht, Germany

[2] HASYLAB at DESY, Hamburg, Germany

Flow of a liquid upon a solid surface is controlled by interactions on different length scales: the interactions between the constituents of the liquid and the solid substrate on the atomic scale as well as the substrate morphology in terms of corrugation, roughness and topography at large length scales give rise to a rich, system-specific behavior.

Micro-fluidic devices which manipulate micro-quantities of liquid solutions allow for substantial improvement of the efficiency of chemical processes, the exact control of mixing and separation processes during fluid flow in confined geometries is thereby essential for many applications as micro-analytics or high throughput devices and reactors as well as for analytical applications, such as chromatography. Up to now , mostly microscopy based experimental techniques have been employed to investigate the behavior of fluids in channels and confined near surfaces. Although crucial, these techniques should be complemented with others to cover a larger range of characteristic lengths. Moreover,complementary methods should be sensitive to composition fluctuations and provide a direct statistically relevant information via a representative sampling. All these features are clearly within reach of scattering techniques. Grazing incidence small angle x-ray scattering (GISAXS) provides such information on parallel structures.

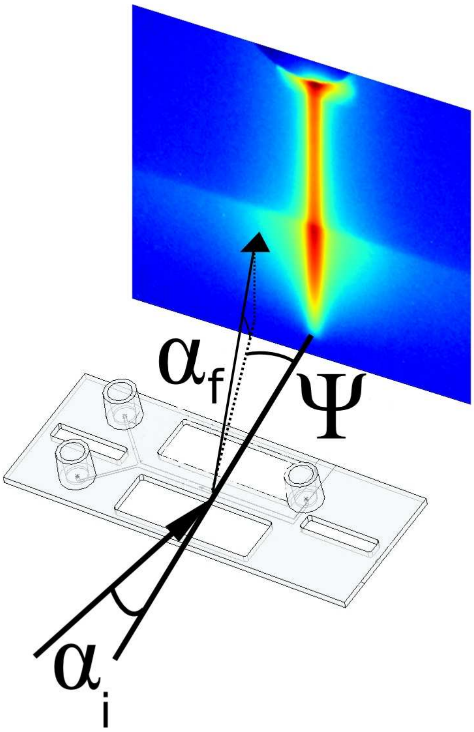

Figure 7.4:
Sketch of the μGISAXS geometry with included design layout of the TOPAS part of the fluidic cell. The asymmetric design with two inlets and one outlet (or vice versa) enables mixing of fluids.

In order to perform a GISAXS experiment on a fluidic system, a setup is required which optimizes the useful signal by minimizing the absorption and parasitic scattering from the cell itself while still ensuring proper sealing in combination with a well defined geometry. Recently, Nickel et al. proposed a special fluidic cell design for specular x-ray reflectivity with 20 keV photon energy [1]. This fluidic cell is based on a modification of a relatively large commercial plastic cell which exhibits a 5 mm wide channel. We chose to use the same material as Nickel et al. [1] for the cell body (top surface with channel system), TOPAS which is a commercially available cyclic olefin based copolymer resistant to polar organic solvents and water [2]. This material can be easily machined and thermally bonded to itself. It has a relatively low absorption in the x-ray range (the attenuation length of TOPAS is 4.9 mm at 10 keV, the photon energy we used for our synchrotron experiment). Moreover it is transparent to visible light which enables optical characterization of the flow via microscopy.

The channel has a Y-shape (see figure 7.4) in such a way that mixing (or demixing) of solutions can be realized. This channel was machined in a 1 mm thick TOPAS foil which was then bonded to a 200 micron thick TOPAS window. The thin channel walls are quite fragile and can easily be twisted during sample preparation, we thus reinforced the structure by leaving two bridges that can be easily cut away once the setup is locked in the clamp (see figure 7.5).

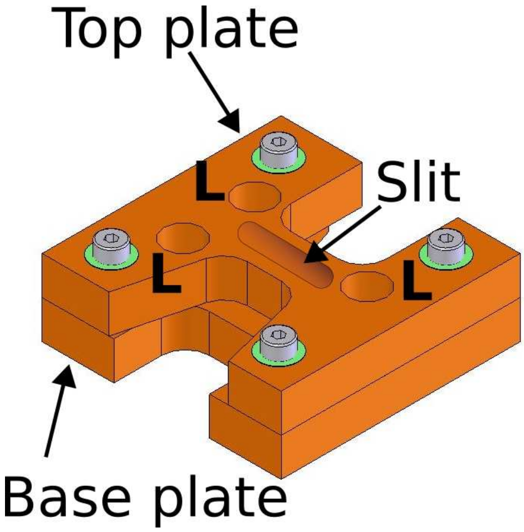

Figure 7.5:
Design layout of the metal clamp which allows for a sealing of the cell body to various substrates without using glue. The opennings for the Luer connectors are shown (L) as well as the slit for optical observation.

The input and output connectors are standard Luer plugs also made of TOPAS and bonded to the top window after drilling of the inlet and outlet holes.

The clamp used to assemble the cell body and the substrate is made of 8 mm thick stainless steel for reasons of rigidity. Holes were drilled to accommodate the Luer connectors. A slit in the top plate was added to enable the optical observation of the flow. On the one hand, the notches on the side of the clamps are intended to limit the shadowing of the x-ray beam and to minimize the risk of parasitic scattering, and on the other hand, to enable optical observation of the cell walls in order to check for leaks.

Mounting and sealing the cell are the critical steps of the fluidic experiments. Within the work presented here, we used 1 mm thick microscope glass slides as a substrate. The glass surfaces were cleaned to remove any contamination which could affect surface properties and sealing quality [3]. The TOPAS channel was then carefully placed on the substrate, taking care to avoid torsion or scratching of the surfaces. In the next step the clamp was closed and slowly tightened while maintaining uniform pressure. The torque applied to each screw, as measured with a dynamometric key, was typically of 6 Nm.

Injection of the filtered solutions was performed using a syringe pump (model PHD 2000 Infuse/Withdraw from Harvard Apparatus). The syringes were connected to the cell via 1.8 mm inner diameter silicone tubes and Luer adapters.

[1] C. Reich, M. Hochrein, B. Krause, B. Nickel,Rev.Sci. Instr. **76**, 095103 (2005).

[2] J.-F. Moulin, S.V. Roth, P. Müller-Buschbaum; Rev. Sci. Instr. **79**, 015109 (2008)

[3] P. Müller-Buschbaum, Euro. Phys. J. E **12**, 443 (2003).

7.3 Characterization of highly porous polymeric materials with pore diameters larger than 100 nm

C.C. Egger[1], C. du Fresne[1], V. I. Raman[1], V. Schädler[1], S.V. Roth[2], P. Müller-Buschbaum

[1] ISIS-BASF, Strasbourg, France
[2] HASYLAB at DESY, Hamburg, Germany

Porous materials require the characterization of both their porous network (volume, pore size and shape) and also their wall surfaces (surface area, functionality). Further, porous materials are a very challenging class of materials owing to both the versatility of their syntheses (which usually vary greatly with pore size), and owing to their characterization involving very different techniques according to the length scale to investigate. Characterization of porous materials was historically carried out by adsorbing and condensing a gas into the porous network and by measuring the resulting volume change [1]. Traditionally nitrogen was used as the adsorbate, although other gases have been used as well. Adsorption of liquids in the porous network can also be carried out, though less frequently, as the resulting surface areas are not always reliable [2].

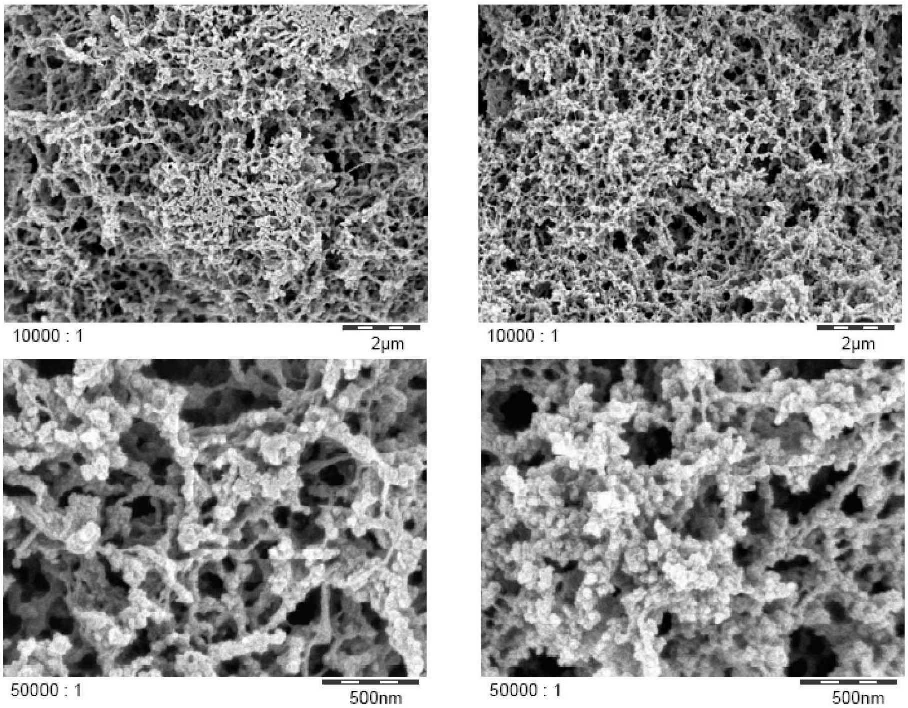

Figure 7.6:
HRSEM at 10k and 50k magnification of two different xerogel samples with different preparation routes showing in both cases a filament-like structure entrapping a large pore volume. The filaments seem to be made of small particles, the size of which is smaller than that of the pores (average particle size <100 nm, average pore size >200 nm).

The highly porous organic specimens such as xerogels and aerogels represent a very challenging class of porous materials. Indeed, generation of high density of pores with dimensions greater than 100 nm, yet submicronic, within an organic matrix requires special synthetic techniques such as supercritical drying methods for instance. However, characterization is a problematic issue to solve owing to (i) their very low compressive strength they are subject to compression when pressurized with mercury and (ii) their rather large pores, pore filling with nitrogen requires long equilibration times preventing capillary condensation to occur at relative pressures close to unity and consequently preventing pore size distribution (PSD) determination. Scanning electron microscopy (SEM or HRSEM) can only access morphological features (e.g. qualitative density and pore size estimation). No quantitative data such as pore volume or PSD can be obtained due to the loss of information through the projection in two dimensions of a three-dimensional structure. So there is an obvious need for another independent technique to access the structural features such as the combination of small angle x-ray scattering (SAXS) and ultra-small angle x-ray scattering (USAXS) [3].

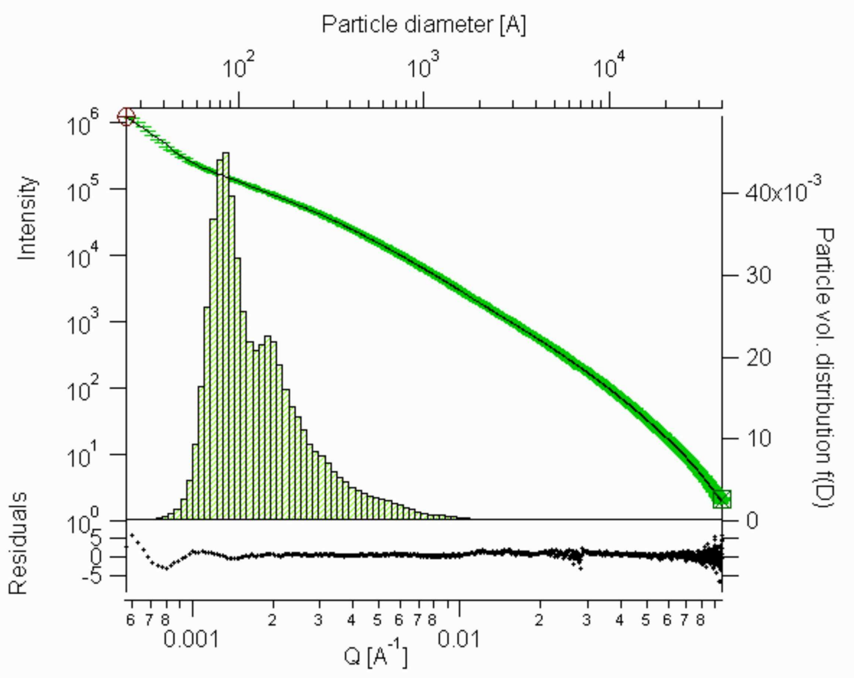

Figure 7.7:
Example of merged USAXS and SAXS data as measured for a selected xerogel sample. The experimental data (crosses) are plotted together with the particle volume distribution (histograms) and the residuals (dots). The data fits based on the model using the free object distribution are plotted with the black solid lines.

Due to the very high porous volume in the samples (average porous volume 87%), with scattering, instead of pores inside a matrix of polymer material, the opposite, polymer filaments made of small particles and entrapping a large pore volume was detected [4]. Thus in such class of samples, Hg/N2 intrusion and scattering access complementary information (pores versus polymer particles). HRSEM and scattering are necessarily combined to unambiguously allow for the understanding of the scattering data. However, due to the much higher statistical relevance of the scattering data, HRSEM measurements alone are not sufficient to give the full structural information. With respect to applications, in which such xerogels might be considered for thermal isolation purpose.

[1] Anderson J. S., Z. Phys. Chem., 1914, 88, 211.

[2] Sing K.S. W., Adv. Colloid Inter. Sci., 1998, 76-77, 3-11.

[3] Pedersen J.S. in ”Neutrons, X-rays and Light: Scattering Methods Applied to Soft Condensed Matter” ed. By Lindner, P. and Zemb, T.Elsevier, Amsterdam (2002)

[4] Egger, C.C.; du Fresne, C.; Raman, V.I.; Schädler, V.; Frechen, T.; Roth, S.V.; Müller-Buschbaum, P.; Langmuir 2008, 24, 5877.

7.4 Development of a new instrument: μGISAXS combined with imaging ellipsometry at the MINAXS beamline of the PETRAIII synchrotron radiation source

V. Körstgens, R. Meier, J. Wiedersich, S. V. Roth[1], P. Müller-Buschbaum

[1] HASYLAB at DESY, Hamburg, Germany

In fall 2009 the MINAXS (micro- and nanofocus x-ray scattering) beamline of the high brilliance synchrotron radiation source PETRAIII at DESY, Hamburg will start its operation. We are developing the GISAXS (grazing incidence small angle x-ray scattering) instrument for the new MINAXS beamline. For the GISAXS instrument the microfocus option will be used with low divergent beams in size of 40 x 20 μm^2 and 10 x 5 μm^2, respectively. The μGISAXS method is well established and very powerful. GISAXS is a non-destructive structural probe giving access to lateral structures at the surface as well as buried structures [1]. Whereas GISAXS averages over macroscopic regions to get information on the nanometerscale with excellent sampling statistics, with the micro-sized beam in μGISAXS the idea is to obtain local structural information [2]. Scanning perpendicular to the direction of the x-ray beam of inhomogeneous samples such as gradient films is possible. Whereas in the common setup available at a few beamlines at synchrotron radiation sources the samples are investigated with μGISAXS and simultaneously with optical microscopy, we develop an advanced method with in-situ imaging ellipsometry replacing the optical microscopy. With imaging ellipsometry not only the region of interest on the sample for the scattering experiment will be chosen. Moreover a comprehensive sample characterization is possible including local film thickness and optical properties.

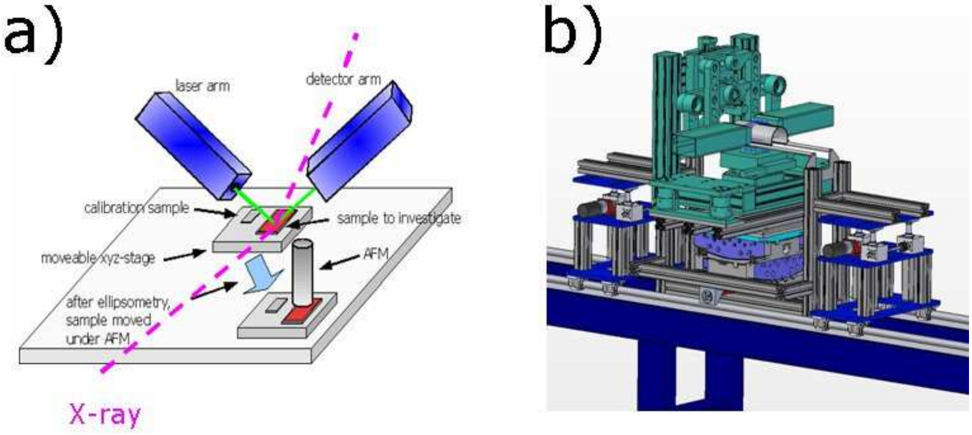

Figure 7.8:
a) Sketch of the basic set-up, detector- and laserarm of imaging ellipsometer are oriented perpendicular to the x-ray beam, sample can be moved out of the beam for additional AFM measurements. b) Set-up with 2-circle goniometer for the positioning of the ellipsometer in the x-ray beam (CAD drawing by Tom Schubert, Hasylab, Hamburg)

The imaging ellipsometer chosen for implementation in the GISAXS instrument is a SPEM (surface probe ellipsometric microscope, Nanofilm GmbH). Figure 7.8a shows a sketch of the basic set-up with detector- and laserarm of the imaging ellipsometer oriented perpendicular to the incoming x-ray beam. The imaging ellipsometer contains a motorized focusing mechanism to collect a series of images with different foci within the field-of-view. With superposition of focused parts the ellipsometer software delivers the final image. The concept of our GISAXS instrument is that the sample is ellipsometrically aligned (and measured) first. Afterwards the sample including the whole ellipsometer set-up is positioned into the x-ray beam. The positioning task is demanding since the required precision of positioning has to be fulfilled with a mass to be moved of nearly 200 kg. Additionally the beam position at the MINAXS beamline restricts the positioning set-up to a limited height. In figure 7.8b the set-up of the ellipsometer with a 2-circle goniometer for setting the incident angle and the tilt is shown which will be used for a test at beamline BW4 in February 2009. This beamtime with the testing of procedures and the modified equipment (e.g. radiation shielding and cable extensions in order to operate the instrument from outside the hutch) will be an important step towards the final installment of the instrument at the MINAXS beamline later in 2009. Our aim for the μGISAXS instrument is to realize a *plug and play mode* with fast and easy installment. The conversions and modifications necessary for the preparation of a particular beamtime should be kept to a minimum. This will save time and effort in the built-up and alignment at the start of a beamtime.

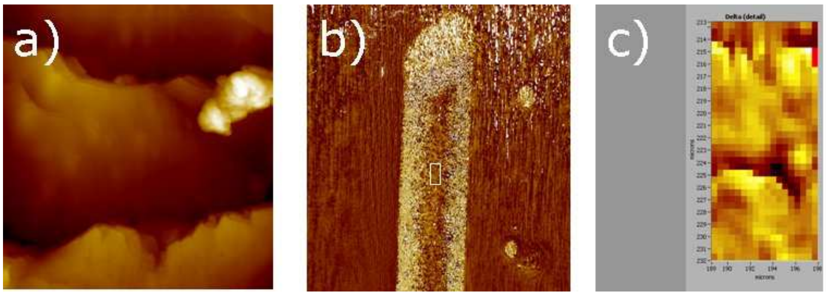

Figure 7.9:
Demonstration of the combination of AFM and ellipsometry: a) topography of human hair measured in non-contact mode, image size 10 x 10 μm^2, b) image of hair taken with ellipsometer before, image size 385 x 393 μm^2 c) detail delta mapping on the center of the hair, image size 10 x 20 μm^2.

The SPEM is equipped with an AFM (atomic force microscope) as shown in figure 7.8a, which gives the opportunity to get additional surface information as demonstrated for a sample of human hair (fig.7.9) sticking to an adhesive covered glass substrate. The topography measured on the center of the hair in non-contact mode (fig.7.9a)) clearly shows the overlapping cuticles of the hair. A calibration procedure for the ellipsometer – AFM combination allows for hitting of the right spot chosen on the ellipsometric image. With a 10× magnification objective ellipsometric images of size 400×400 μm^2 and a lateral resolution of 2 μm are obtained as shown for the hair sample (fig.7.9b)). Already also in use is an objective with 20× magnification which leads to a resolution of 1 μm. The detail mapping of ellipsometric data, as shown for delta (fig.7.9c)) on the center of the hair, also shows the hair structure built out of cuticles.

In summary the μGISAXS instrument at the new MINAXS beamline will provide the possibilities of conventional μGISAXS with local lateral and depth sensitive structural characterization. Furthermore position sensitive determination of the 3d morphology (thickness, roughness, refractive index and extinction) is feasible with the imaging ellipsometer. As a third integral part the AFM delivers high resolution surface topography and mechanic information.

In combination the μGISAXS instrument will allow for complete characterization of structures and morphology. It will be ideal in case of in-situ experiments and sensitive samples.

This project is financially supported by BMBF (grant 05KS7WO1).

[1] P. Müller-Buschbaum, Anal. Bioanal. Chem. **376**, 3 (2003)

[2] P. Müller-Buschbaum, S. V. Roth, M. Burghammer, A. Diethert, P. Panagiotou, C. Riekel, Europhys. Lett. **61**, 639 (2003)

7.5 Absolute d-spacing value determination by Larmor diffraction

J. Repper[1], T. Keller[1,2], M. Hofmann[1], C. Krempaszky[3]

[1] Forschungsneutronenquelle Heinz Maier-Leibnitz (FRM II), TU München, 85747 Garching

[2] Max-Planck-Institut für Festkörperphysik, 70569 Stuttgart

[3] Christian-Doppler-Labor für Werkstoffmechanik von Hochleistungslegierungen, TU München, 85747 Garching

Residual stress analysis using neutron diffraction relies on the comparison of the lattice spacing d of a stressed component with the lattice spacing d_0 from a macroscopic stress free reference sample. In neutron Larmor diffraction the lattice spacing d is encoded in the spin precession of a polarized monochromatic neutron beam scattered at the sample. In contrast to conventional neutron diffraction methods Larmor diffraction is independent of the divergence of the incident beam, the spread of the wavelength and the scattering angle 2θ [1]. Based on this, the Larmor technique is insensitive to alignment errors of the sample, which may cause large shifts in measured 2θ-values in conventional diffractometer techniques [2]. Hence, the method enables the measurement of reference values d_0 with a very high accuracy (in the order of 10^{-5} Å) hitherto not possible using classical diffractometers [3].

Larmor diffraction experiments (an introductin can be found by Rekveldt [1,4]) to determine absolute lattice spacing d for the first time were performed at the thermal neutron triple axis spectrometer TRISP at FRM II [5]. A powder sample of SRM640c silicon was used to verify the results obtained by Larmor diffraction. Two sample sets of cylindrical Inconel 718 samples were measured. Each set consisted of three samples with different radii (1 mm, 5 mm and 10 mm). The samples were cut from two differently treated pancakes (diameter = 240 mm, thickness = 20 mm) at a radius of $r = 80$ mm. Both pancakes were forged at a temperature of 990°C and cooled down to room temperature in different ways: The first disk was water quenched (WQ), whereas the second disk was cooled down in air (AC). In contrast to all other previous Larmor diffraction experiments, in which only relative changes in the d-spacing of a crystal were observed, a reference sample with an exact known lattice spacing is necessary for the determination of an absolute value of the d-spacing. In our case a perfect Germanium single crystal (fcc) with a lattice parameter of $a = 5.65726(7)$ Å [6] was used as reference specimen. An incident wave vector k_i of 3.53 Å^{-1} ($\lambda = 1.78$ Å) was chosen for the Germanium and the IN718 samples. For the measurements on silicon the incident wave vector was changed to k_i of 3.45 Å^{-1} ($\lambda = 1.82$ Å) to keep the scattering angle constant at $2\theta = 110°$. Due to their similar d-spacing, the (333) Bragg reflection of Germanium ($d_{\text{Ge(333),theo}} = 1.08874(7)$ Å) and the (311) Bragg reflection of the IN718 Ni-matrix were chosen for the measurements, while for the Silicon powder the (422) reflection was used. To gain a high neutron intensity on the sample position no collimation and an averaged beam size of approx. 40 x 40 mm^2 were used.

The theoretical d spacing of the Si(422) Bragg reflection can be calculated from the lattice constant $a = 5.4311946(92)$ Å [7] as $d_{\text{Si,theo}} = 1.108638(9)$ Å. The determination of the d-spacing by analyzing the Larmor diffraction data is $d_{\text{Si,Larmor}} = 1.108620(70)$ Å. This gives a difference of $\Delta d = 1.8 \cdot 10^{-5}$ Å (see table 1) which is within error bars. The error bar of the lattice spacing determined by Larmor diffraction is in the same order of magnitude, than the error bar for the Ge$\{333\}$-d-spacing ($7 \cdot 10^{-5}$ Å). This shows the limitation of the accuracy by the quality of the reference specimen. The use of a reference specimen with lattice constants determined one order of magnitude more accurate, reduces the error bars at least by a factor of 7 to $1 \cdot 10^{-5}$ Å.

The d-spacing of the IN718 samples determined by Larmor diffraction was compared to the results achieved by a conventional neutron diffraction experiment (see table 2). A good agreement of the two methods can be found for the samples with radii of 5 and 10 mm (differences in the order of $10^{-5}/10^{-6}$ Å). In case of the 1 mm samples a higher difference in the values of the lattice

Table 1: Lattice spacing d of the Si(422) Bragg reflection, determined with data measured at TRISP compared with the theroretical value calculated from a given lattice constant of Si powder ($a = 5.431195(9)$ Å).

	Lattice spacing [Å]		
	TRISP	Theoretical value	Difference
Si Powder, Si(422)	1.108620(70)	1.108638(9)	$1.8 \cdot 10^{-5}$

Table 2: Lattice spacing d of the Ni(311) Bragg reflection of different samples. The values determined with datat measured at TRISP are compared with values determined by STRESS-SPEC.

Sample		Lattice spacing [Å]		
	Radius [mm]	TRISP	STRESS-SPEC	Difference
AC, Ni(311)	1	1.084978(70)	1.084124(685)	$8.5 \cdot 10^{-4}$
	5	1.084972(70)	1.084944(686)	$2.8 \cdot 10^{-5}$
	10	1.085024(70)	1.084926(686)	$9.8 \cdot 10^{-5}$
WQ, Ni(311)	1	1.085402(70)	1.084530(684)	$8.7 \cdot 10^{-4}$
	5	1.085408(70)	1.085342(685)	$6.6 \cdot 10^{-5}$
	10	1.085437(70)	1.085434(685)	$2.3 \cdot 10^{-6}$

spacing (in the order of $8 \cdot 10^{-4}$ Å) can be observed. This can be explained by the difficulties to align the sample in the center of gravity of the conventional diffractometer. Small shifts in the sample position can cause large shifts in the 2θ values and as a consequence in the lattice spacing d. For the larger samples small misalignment effects are negligible compared to the sample size. As discussed for the Si values, also the errors in the absolute lattice spacing of the IN718 samples are relatively high using the Lamor diffraction method. However, they are much lower than the lattice spacing determined by conventional neutron diffraction. A comparison of the lattice spacing of the different samples of the same sample state shows a relative resolution of $10^{-5}/10^{-6}$, as expected.

[1] M.T. Rekveldt, T. Keller, W.H.Kraan: Europhys. Lett, 54 (2001), 342-346.

[2] S. Spooner, X.-L. Wang: J. Appl. Cryst., 30 (1997), 449-455.

[3] C. Pfleiderer, P. Böni, T. Keller, U.K. Rößler, A. Rosch, Science, 316 (2007), 1871-1874.

[4] M.T. Rekveldt: Mater. Sci. Forum, 321-324 (2000), 258-263.

[5] T. Keller, P. Aynajian, S. Bayrakci, K. Buchner, K. Habicht, H. Klann, M. Ohl, B. Keimer: Neutron News, 18(2) (2007), 16-18.

[6] O. Brümmer, V. Alex, G. Schulze: Ann. Phys., 28 (1972), 118-134.

[7] S.W. Freiman, N.M. Trahey: National Institute of Standards & Technology Certificate, Standard Reference Material® 640c, Gaithersburg, MD 20899, 2000.

8 Teaching and conferences

8.1 Lectures, seminars and lab courses

Spring semester 2008
Prof. Dr. Peter Müller-Buschbaum, *Angewandte Physik: Polymerphysik 2*
Prof. Dr. Peter Müller-Buschbaum, *Experimentalphysik 2 für Maschinenwesen*
Prof. Dr. Peter Müller-Buschbaum, *Seminar über Struktur und Dynamik kondensierter Materie*
Prof. Dr. Peter Müller-Buschbaum, Prof. Dr. Christine Papadakis, *Seminar über spezielle Probleme der weichen Materie*
Prof. Dr. Christine Papadakis, *Angewandte Physik: Experimentalphysik 2 für LB* (EI/BT/MT)
PD Dr. Wolfgang Doster, *Experimentalphysik 2 für LB*
Prof. Dr. Walter Schirmacher, *Theoretische Physik 3 (Quantenmechanik)*

Fall semester 2008/2009
Prof. Dr. Peter Müller-Buschbaum, *Physik 1 für Maschinenwesen*
Prof. Dr. Peter Müller-Buschbaum, *Nanostructured Soft Materials 1*
Prof. Dr. Peter Müller-Buschbaum, *Seminar über Struktur und Dynamik kondensierter Materie*
Prof. Dr. Peter Müller-Buschbaum, Prof. Dr. Christine Papadakis, *Seminar über spezielle Probleme der weichen Materie*
Prof. Dr. Christine Papadakis, *Angewandte Physik: Polymerphysik 1*
Prof. Dr. Christine Papadakis, *Experimentalphysik 1 für LB* (EI/BT/MT)

Lab courses 2008
Statische und dynamische Lichtstreuung (Biophysikalisches Praktikum)
Theoretische und praktische Einführung in AFM (Fortgeschrittenenpraktikum)
Thermische Analyse (Fortgeschrittenenpraktikum)

8.2 Conferences

Biomolecular Dynamics and Protein-Water Interactions
Neutron Scattering Workshop
Sept 24-26 2008 in Munich Feldafing

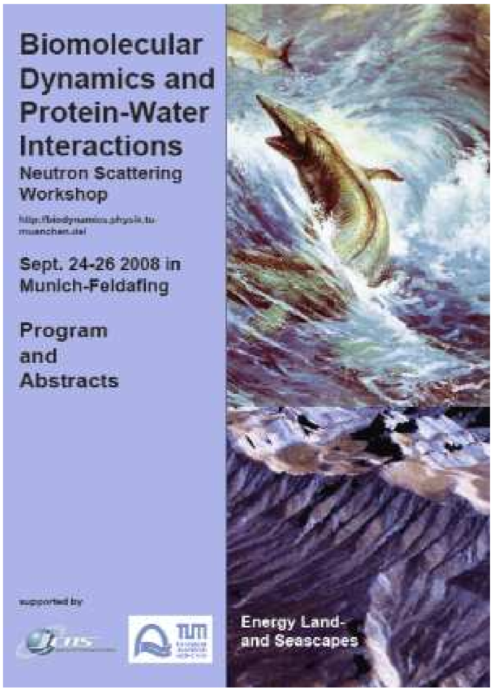

Biomolecular Dynamics and Protein-Water Interactions
Neutron Scattering Workshop

Sept. 24-26 2008 in Munich-Feldafing

Program and Abstracts

Energy Land- and Seascapes

Workshop Program

24. Sept 08

18:00 - Welcome with small buffet at Bildungszentrum Feldafing

25. Sept 08

08:30 - Introduction - Wolfgang Doster, TUM, E13
09:00 - Protein Hydration I (chair A. Sokolov)
11:00 - Protein Hydration II (chair M. Tarek)
13:30 - Protein Dynamics I (chair G. Kneller)
15:30 - Protein Dynamics II (chair J. Curtis)
17:30 - Round Table Discussion on Dynamics of Protein-Water Interactions (chair J. Teixera)
19:00 - Dinner
20:00 - Poster session & beer meeting

26. Sept 08

09:00 - Collective Dynamics I (chair D. Zhong)
11:00 - Collective Dynamics II (chair J. Swenson)
13:30 - New Methods and Systems (chair M. Kataoka)
15:45 - Round Table Discussion Biodynamics, Where to go? (chair W. Doster)
16:30 - Tour of Roseninsel

Lüscher Lectures – Forschung an Großgeräten
Gymnasium Zwiesel

RLFB -Tagungsprogramm

32. EDGAR - LÜSCHER - PHYSIKSEMINAR 2008 AM GYMNASIUM ZWIESEL

Thema: Forschung an Großgeräten

Freitag, 4. April bis Sonntag, 6.April 2008

Veranstalter: Der Ministerialbeauftragte für die Gymnasien in Niederbayern, OStD Klaus Drauschke

Wissenschaftliche Leitung: Prof. Dr. Walter Schirmacher, Prof. Dr. Winfried Petry, TU München

Organisation am Gymnasium Zwiesel: StD Hans-Werner Janda, StD Günther Haller, OStR Wolfgang Achatz

Lüscher Lectures – Magnetismus
Bay. Lehrerfortbildungsakademie in Dillingen (Donau)
15.10.-17.10.2008

Lehrgangsnummer: 75/258
Leitung: StD Werner Ettinger / Prof. Dr. Walter Schirmacher
Schulart: Alle Schularten
Zielgruppe: Lehrkräfte
Lehrgangsort: Dillingen
Anmeldeschluss: 21.09.08
Teilnehmerzahl: 32

In den letzten Jahren sind bei der Erforschung des Magnetismus viele neue Erkenntnisse gewonnen worden. In der Forschung tätige Wissenschaftler vermitteln auf anschaulichem Niveau einen Einblick in ihr Forschungsgebiet und stehen den Teilnehmern auch für Fragen zur Verfügung, wie die Erkenntnisse in den Unterricht integriert werden können.

9 Publications, talks and funding

9.1 Publications

- M. M. Abul Kashem, J. Perlich, L. Schulz, S. V. Roth, P. Müller-Buschbaum
  Correlated Roughness in Polymer Films Containing Maghemite Nanoparticles
  Macromolecules **41**, 2186-2194 (2008)

- K. Böning, W. Petry
  Test Irradiations of Full sized $U_3Si_2 - Al$ *Fuel Plates up to very High Fission Densities*
  Journal of Nuclear Science (2008)

- H. Breitkreutz, F. Wagner, A. Röhrmoser, W. Petry
  Spectral fluence rate of the fast reactor neutron beam MEDAPP at FRM II
  Nuclear Instruments and Methods in Physics Research A 593, 466 - 471 (2008)

- A. Diethert, F. Finster, D. Schiefeneder
  Fermion systems in discrete space-time exemplifying the spontaneous generation of a causal structure
  International Journal of Modern Physics A **23**, 4579-4620 (2008)

- C. C. Egger, C. du Fresne, V. I. Raman, V. Schädler, T. Frechen, S. V. Roth, P. Müller-Buschbaum
  Characterisation of highly porous polymer materials with pore diameters larger than 100 nm by mercury porosimetry and x-ray scattering methods
  Langmuir **24**, 5877-5887 (2008)

- B. Ferse, S. Richter, F. Eckert, A. Kulkarni, C.M. Papadakis, K.-F. Arndt
  Gelation Mechanism of Poly(N-isopropylacrylamide)-Clay Nanocomposite Hydrogels Synthesized by Photopolymerization
  Langmuir **24**, 12627 (2008)

- A. M. Gaspar, M. S. Appavou, S. Busch, T. Unruh, W. Doster
  Dynamics of Well-folded and Natively Disordered Proteins in Solution: A time-of-flight neutron scattering study
  Eur. Biophys. J. **37**, 573-582 (2008)

- R. Gebhardt, M. Burghammer, C. Riekel, S. V. Roth, P. Müller-Buschbaum
  Structural changes of casein micelles in a calcium gradient film
  Macromol. Biosci. **8**, 347-354 (2008)

- F. González Sánchez, F. Jurányi, T. Gimmi, L.V. Loon, T. Unruh, L.W. Diamond
  Translational diffusion of water and its dependence on temperature in charged and uncharged clays: a neutron scattering study
  J. Chem. Phys., **129**, 174706 (2008)

- F. González Sánchez, F. Jurányi, T. Gimmi, L.V. Loon, T. Seydel, T. Unruh
  Dynamics of supercooled water in highly compacted clays studied by neutron scattering
  J. Phys.: Condens. Matter **20**, 415102 (2008)

- E. Gutsmiedl, A. Frei, A.R. Müller, S. Paul, M. Urban, H. Schober, C. Morkel, T. Unruh
  Understanding UCN Production in Solid D_2*: The Generalized Density of States Measured via Inelastic Neutron Scattering*

Proceedings of the international workshop on particle physics with slow neutrons, Grenoble, France, 29 – 31 May 2008,

- D. Holland-Moritz, S. Stüber, H. Hartmann, T. Unruh, T. Hansen, A. Meyer
  Structure and Dynamics of Liquid $Ni_{36}Zr_{64}$ *studied by neutron scattering*
  Phys. Rev. B (submitted)

- D. Holland-Moritz, S. Stüber, H. Hartmann, T. Unruh, A. Meyer
  Ni self-diffusion in Zr-Ni(-Al) melts
  Proceedings of the the 13th International Conference on Rapidly Quenched & Metastable Materials (RQ13), Journal of Physics: Condensed Matter Conference Series (accepted)

- R. Ivanova, T. Komenda, T.B. Bonné, Karin Lüdtke, K. Mortensen, P.K. Pranzas, R. Jordan, C.M. Papadakis
  Micellar structures of hydrophilic/lipophilic and hydrophilic/fluorophilic poly(2-oxazoline) diblock copolymers in water
  Macromol. Chem. Phys. **209**, 2248-2258 (2008)

- G. Kaune, W. Wang, E. Metwalli, M. Ruderer, R. Roßner, S. V. Roth, P. Müller-Buschbaum
  Layered TiO2:PVK nano-composite thin films for photovoltaic applications
  Euro. Phys. J. E **26**, 73-79 (2008)

- I. Köper, S. Comet, W. Petry, M. Bellissent-Funel
  Dynamics of C-Phycocynanin in various deuterated Threhalose/Water Environments by Quasielastic and Elastic Neutron Scattering
  European Biophysical Journal 37, 739-748 (2008)

- V. Körstgens, C.-C. Hsu, D. Paneque, J. Wiedersich, P. Müller-Buschbaum
  Improvement of quantum efficiency of photomultiplier tubes by humidity controlled coatings based on porous polymer structures
  Appl. Phys. Lett. **93**, 041916, (2008)

- A. Leenaers, A. VanDenBerghe, M. Anselmet, J. Noiret, P. Lemoine, A. Röhrmoser, W. Petry
  Irradiation Behavior of Atomized and Ground U(Mo) Dispersion Fuel
  Transactions of RERTR 2008 - 30th International Meeting on Reduced Enrichment for Research and Test Reactors, 5 – 9 Oct 2008.

- T. Mehaddene, J. Neuhaus, W. Petry, K. Hradil, P. Bourges, A. Hiess
  Phonon dispersions in Ni-Al-Mn shape memory alloy
  Materials Characterization Science and Engineering A 481-482, 197-200 (2008)

- T. Mehaddene, J. Neuhaus, W. Petry, K. Hradil, P. Bourges, A. Hiess
  Interplay of stuctural instability and lattice dynamics in Ni_2MnAl
  Phys. Rev. Lett. B. (2008)

- R. Meier, R. C. Word, A. Nadarajah, R. Könenkamp
  Unipolar transport and interface charge transfer in nanostructured CdTe/polymer hybrid films
  Phy. Rev. B, 77, 195314, (2008)

- E. Metwalli, S. Couet, K. Schlag, R. Röhlsberger, V. Körstgens, M. Ruderer, W. Wang, G. Kaune, S. V. Roth, P. Müller-Buschbaum
  In situ GISAXS investigation of gold sputtering onto a polymer template
  Langmuir **24**, 4265-4272 (2008)

- A. Meyer, S. Stüber, D. Holland-Moritz, O. Heinen, T. Unruh
  Determination of self-diffusion coefficients by quasielastic neutron scattering measurements of levitated Ni droplets
  Phys. Rev. B **77**, 092201 (2008)

- A. Meyer, J. Horbach, O. Heinen, D. Holland-Moritz, T. Unruh
  Self Diffusion in Liquid Titanium: Quasielastic Neutron Scattering and Molecular Dynamics Simulation
  Defect and Diffusion Forum (accepted)

- J-.F. Moulin, S. V. Roth, P. Müller-Buschbaum
  Flow at interfaces: a new device for x-ray surface scattering investigations
  Rev.Sci.Instr. **79**, 015109 (2008)

- P. Müller-Buschbaum, L. Schulz, E. Metwalli, J.-F.Moulin, R.Cubitt
  Lateral structures of buried interfaces in A-B-A-type block polymer films
  Langmuir **24**, 7639-7644 (2008)

- P. Müller-Buschbaum
  Structure determination in the thin film geometry using grazing incidence small angle scattering in "Polymer Surfaces and Interfaces: Characterization, Modification and Applications", edt. M. Stamm
  p.17-46 Springer Berlin, ISBN-13: 978-3-540-73864-0 (2008)

- C.M. Papadakis, Z. Di, D. Posselt, D.-M. Smilgies
  Structural Instabilities in Lamellar Diblock Copolymer Thin Films During Solvent Vapor Uptake
  Langmuir (Letter) **24**, 13815 (2008)

- A.I. Pommrich, A. Meyer, D. Holland-Moritz, T. Unruh
  Nickel self-diffusion in Silicon-rich Si-Ni melts
  Appl. Phys. Lett. **92**, 241922 (2008)

- M. Prager, H. Grimm, I. Natkaniec, D. Nowak, T. Unruh
  The dimensionality of ammonium reorientation in $(NH_4)_2S_2O_8$*: the view from neutron spectroscopy*
  J. Phys.: Condens. Matter, **20**,125218, (2008)

- M. Prager, A. Desmedt, T. Unruh, J. Allgaier
  Dynamics and adsorption sites for guest molecules in methyl chloride hydrate
  J. Phys.: Condens. Matter, **20**, 125219, (2008)

- J. Repper, M. Hofmann, C. Krempaszky, W. Petry, E. Werner
  Influence of microstructural parameters on macroscopic residual stress analysis of complex materials by neutron diffraction methods
  Materials Science Forum, **571-572**, 39-44 (2008)

- J. Repper, M. Hofmann, C. Krempasky, R. Wimpory, W. Petry, E. Werner
  Micro stress accumulation in multiphase superalloys
  Proceedings of the ICRS8: The Eighth International Conference on Residual StressesAugust 6- 8, 2008, Marriott Tech Center, Denver, Colorado, USA –, 7

- J. Repper, M. Hofmann, C. Krempasky, Th. Keller, W. Petry, E. Werner
  Investigations of lattice spacing on IN718 via neutron Larmor diffraction

Proceedings of the ICRS8: The Eighth International Conference on Residual Stresses, 6 – 8 Aug, 2008, Marriott Tech Center, Denver, Colorado, USA

- A. Röhrmoser, W. Petry, P. Boulcourt, A. Chabre, S. Dubois, P. Lemoine, Ch. Jarousse, J.L. Falgoux, S. van den Berghe, A. Leenaers
  UMo full plate size irradiation experiment IRIS-TUM - a progress report Transactions of the RRFM 2008
  Hamburg, March (2008)

- F. F. Rossetti, P. Panagiotou, F. Rehfeld, E. Schneck, M. Dommach, S. S. Funari, A. Timmann, P. Müller-Buschbaum, M. Tanaka
  Structures of regenerated cellulose films revealed by grazing incidence small-angle x-ray scattering
  Biointerphases 3, 117-127 (2008)

- W. Schirmacher, H. Sinn
  Collective dynamics of simple liquids: a mode-coupling description
  Condensed Matter Physics **11**, 127 (2008)

- W. Schirmacher, B. Schmid, C. Tomaras, G. Viliani, G. Baldi, G. Ruocco, T. Scopigno
  Vibrational excitations in systems with correlated disorder
  phys. stat. sol. (c) **5**, 862 (2008)

- W. Schmid, R. Jungwirth, W. Petry, P. Böni, L. Beck
  Manufacturing of Thick Monolithic Layers by DC-Magnetron Sputtering
  Transactions of the RRFM 2008, Hamburg, March (2008)

- B. Schmid, W. Schirmacher
  Raman scattering and the low-frequency vibrational spectrum of glasses
  Phys. Rev. Lett. **100**, 137402 (2008)

- A. Schulte, Y. Guo, W. Schirmacher, T. Unruh, T. Cardinal
  Low-frequency vibrational excitations in a niobium-phosphate glass for Raman gain applications
  Vibrat. Spectrosc. **48**, 12 (2008)

- C. Smuda, G. Gemmecker, T. Unruh
  Quasielastic and inelastic neutron scattering study of methyl group rotation in solid and liquid pentafluoroanisole and pentafluorotoluene
  J. Chem. Phys., **128**, 194502, (2008)

- C. Smuda, S. Busch, G. Gemmecker, T. Unruh
  Self-diffusion in molecular liquids: Medium-chain n-alkanes and coenzyme Q_{10} *studied by quasielastic neutron scattering*
  J. Chem. Phys., **129**, 014513, (2008)

- C. Smuda, S. Busch, B. Wagner, T. Unruh
  Methyl group dynamics in glassy, polycrystalline, and liquid coenzyme Q_{10} *studied by quasielastic neutron scattering*
  J. Chem. Phys., **129**, 074507, (2008)

- C. Smuda, S. Busch, R. Schellenberg, T. Unruh
  Methyl group dynamics in polycrystalline and liquid ubiquinone Q_0 *studied by neutron scattering*
  J. Phys. Chem. B, in press

- L. Sobczyk, M. Prager, W.Sawaka-Dobrowolska, G. Bator, A. Pawlukojć, E. Grech, L. van Eijck, A. Iwanow, S. Rols, J. Wuttke, T. Unruh
  The structure and dynamics of methyl groups in diaminodurene (DAD)
  submitted
- A. M. Stadler, J. P. Embs, I. Digel, G. M. Artmann, T. Unruh, G. Büldt, G. Zaccai,
  Cytoplasmic Water and Hydration Layer Dynamics in Human Red Blood Cells
  J. Am. Chem. Soc. (in print)
- W.-D. Stein, F. Tang, A. Schneidewind, T. Unruh, H.-H. Klauss, R. Klingeler, G. Behr, B. Büchner, M. Loewenhaupt
  Inelastic neutron scattering study of $LaO_{0.9}F_{0.1}FeAs$ *and* $PrO_{0.8}F_{0.2}FeAs$
  Proceedings of the 53rd Annual Conference on Magnetism and Magnetic Materials, 10.-14. Nov. 2008, Austin, Texas, USA, J. Appl. Phys. (submitted)
- S.C.M. Teixeira, G. Zaccai, J. Ankner, M.C. Bellissent-Funel, R. Bewley, M.P. Blakeley, P. Callow, L. Coates, R. Dahint, R. Dalgliesh, N.A. Dencher, V.T. Forsyth, G. Fragneto, B. Frick, R. Gilles, T. Gutberlet, M. Haertlein, T. Hauß, W. Häußler, W.T. Heller, K. Herwig, O. Holderer, F. Juranyi, R. Kampmann, R. Knott, S. Krueger, P. Langan, R.E. Lechner, G. Lynn, C. Majkrzak, R.P. May, F. Meilleur, Y. Mo, K. Mortensen, D.A.A. Myles, F. Natali, C. Neylon, N. Niimura, J. Ollivier, A. Ostermann, J. Peters, J. Pieper, A. Rühm, D. Schwahn, K. Shibata, A.K. Soper, Th. Strässle, J. Suzuki, I. Tanaka, M. Tehei, P. Timmins, N. Torikai, T. Unruh, V. Urban, R. Vavrin, K. Weiss
  New Sources and Instrumentation for Neutrons in Biology
  Chem. Phys. **345**, 133-155 (2008)
- K. Troll, A. Kulkarni, W. Wang, C. Darko, A.M. Bivigou Koumba, A. Laschewsky, P. Müller-Buschbaum, C.M. Papadakis
  The collapse transition of poly(styrene-b(N-isopropylacrylamide)) diblock copolymers in aqueous solution and in thin films
  Colloid Polym. Sci. **286**, 1079 (2008)
- T. Unruh, C. Smuda, S. Busch, J. Neuhaus, W. Petry
  Diffusive motions in liquid medium-chain n*-alkanes as seen by quasielastic time-of-flight neutron spectroscopy*
  J. Chem. Phys. **129**, 121106 (2008)
- Th. Voigtmann, A. Meyer, D. Holland-Moritz, S. Stüber, T. Hansen, T. Unruh
  Atomic Diffusion Mechanisms in Zr-Ni Melts
  Europhysics Letters **82**, 66001 (2008)
- F. Wagner, P. Kneschaurek, A. Kastenmüller, B. Loeper-Kabasakal, S. Kampfer, H. Breitkreutz, W. Waschkowski, M. Molls, W. Petry
  The Munic fission Neutron Therapy Facility MEDAPP at FRM II Strahlentherapie und Onkologie
  Urban & Vogel, (2008)
- W. Wang, K. Troll, G. Kaune, E. Metwalli, M. Ruderer, K. Skrabania, A. Laschewsky, S. V. Roth, C. M. Papadakis, P. Müller-Buschbaum
  Thin films of poly(N-isopropylacrylamide) end-capped with n-butyltrithiocarbonate
  Macromolecules **41**, 3209-3218 (2008)
- J. Wiedersich, S. Köhler, A. Skerra, J. Friedrich
  Temperature and pressure dependence of protein stability: The engineered fluorescein-binding

lipocalin FluA shows an elliptic phase diagram
PNAS, **105** 15, 5756-5761, (2008)

9.2 Talks

- M. M. Abul Kashem, P. Müller-Buschbaum
  Iron Oxide Nanoparticles in Supported Block Copolymer Structures
  CompInt Winter School, Antholz, South Tirol, Italy, 1 – 3 March 2008

- Ph. Bourges, K. Hradil, P. Link, T. Mehaddene, J.Neuhaus, W. Petry, R. Schneider
  Lattice dynamics of ferromagnetic shape memory alloys from inelastic neutron scattering
  ICOMAT 2008, Santa Fe, USA, 29 Jun – 5 Jul 2008

- S. Busch, C. Smuda, L. C. Pardo Soto, S. Kurmulis, T. Unruh
  Picosecond-Dynamics of DMPC in Mono- and Bilayers Investigated by Quasielastic Neutron Scattering
  22nd Conference of the European Colloid and Interface Society, Krakau, 01 Sep 2008

- S. Busch, C. Smuda, L. C. Pardo Soto, S. Kurmulis, T. Unruh
  Phospholipids: Their Role in Nature and Biotechnology, Their Picosecond-Dynamics, and Possible Connections
  Seminar of the Grup de Caracterització de Materials, Universitat Politècnica de Catalunya, Barcelona, 10 Oct 2008

- S. Busch, C. Smuda, J. Neuhaus, W. Petry, T. Unruh
  The Time-of-Flight Spectrometer TOFTOF at FRM II: Scientific Highlights and Future Prospects
  JCNS Workshop, Bernried, 17 Oct 2008

- A. Diethert, S. V. Roth, P. Müller-Buschbaum
  Surface enrichment layers in pressure sensitive adhesive films
  XXI Congress and General Assembly of the International Union of Crystallography, Osaka, 27 Aug 2008

- R. Gebhardt, M. Burghammer, C. Riekel, S. V. Roth, P. Müller-Buschbaum
  Structural Changes of Casein Micelles in Calcium and Enzym (Rennet) Gradient Films
  Tagung 'IDF/INRA International Symposium on mineral and dairy products', St. Malo (France), October 2008

- R. Gebhardt, M. Burghammer, C. Riekel, C. Vendrely, S. V. Roth, P. Müller-Buschbaum
  Proteins on Surfaces investigated by microbeam grazing incidence small angle scattering
  Tagung 'MRS Fall Meeting (Symposium OO: Grazing-Incidence Small-Angle X-Ray Scattering)', Boston, December 2008

- R. Jungwirth, W. Petry, W. Schmid, L. Beck, A. Bergmaier
  Progress in Heavy-Ion Bombardement of U-Mo/Al Dispersion Fuel Transactions of the RRFM 2008
  Hamburg (2008)

- A. Kulkarni, K. Troll, C. Darko, C.M. Papadakis, W. Wang, P. Müller-Buschbaum, A. M. Birigou Koumba, A. Laschewsky
  Structure investigations of thermo-sensitive triblock copolymers
  DPG Frühjahrstagung, Berlin, 28 Feb 2008

- M. Memesa, J. S. Gutmann, J. Perlich, G. Kaune, P. Müller-Buschbaum
  An alternative blocking layer for hybrid organic solar cells: preparation, characterization and application
  DFG SPP 1181/2 NANOMAT Arbeitskreistreffen Funktionsmaterialien: Mikrosysteme, Membranen, Katalyse, Mainz, 6 Nov 2008

- E. Metwalli, S. Couet, K. Schlage, R. Röhlsberger, V. Körstgens, M. Ruderer, W. Wang, G. Kaune, S.V. Roth, P. Müller-Buschbaum
  Nanopatterning of gold particles using a polymer template: in situ GISAXS study
  DPG Frühjahrstagung, Berlin, 25 – 29 Feb 2008

- E. Metwalli, J.-F. Moulin, R. Gebhardt, V. Körstgens, R. Cubitt, A. Tolkach, U. Kulozik, P. Müller-Buschbaum
  Water Swelling of Casein Micelles in Thin Films: GISANS Study
  Surfaces & Interfaces in Soft Matter & Biology: the impact and future of neutron reflectivity-A symposium in honor of R.K. Thomas, Grenoble, 21 – 23 May 2008

- P. Müller-Buschbaum
  Nanostrukturierte Polymerfilme – Zusammenhang zwischen Struktur und Funktion
  Kolloquium der Chemie der Universität Halle, March 2008.

- P. Müller-Buschbaum, L. Schulz, E. Metwalli, J.-F. Moulin, R. Cubitt
  Lateral structures of buried interfaces in tri-block copolymer films
  'Symposium rkt2008 – surfaces and interfaces in soft matter' in Grenoble, May 2008

- P. Müller-Buschbaum, A. Diethert
  Probing thin surface layers with specuar x-ray reflection
  Seminar des Instituts für Mechanische Verfahrenstechnik und Mechanik in Karlsruhe, June 2008

- P. Müller-Buschbaum, R. Meier, V. Körstgens, J. Wiedersich
  Development of μGISAXS at the μSAXS/WAXS instrument at PETRA III
  'Treffen der BMBF Verbundforschungsprojekte zu FLASH und PETRA' in Hamburg, July 2008

- P. Müller-Buschbaum
  Exploring large scale structures with high resolution experiments: GIUSAXS / GIUSANS
  'IUCr2008 Satellite meeting on x-ray and neutron techniques for nano-structural research' bei Spring-8 in Hyogo (Japan), August 2008

- P. Müller-Buschbaum
  Recent developments in GISAXS – nano-beams and in-situ kinetic investigations
  'XXI Congress and general assembly of the international Union of crystallography IUCr2008' in Osaka (Japan), August 2008

- P. Müller-Buschbaum, J. S. Gutmann
  Bioinspired structures for application in photovoltaics
  DFG Gutachtertreffen zum SPP1420 'Biomimetic Materials Research: Functionality by Hierarchical Structuring of Mate Materials' in Bonn, December 2008

- J. Neuhaus, W. Petry
  Magnetic, magnetoelastic and dynamical properties of martensitic Heusler alloys: phonon spectra
  Evaluation of SPP 1239, IFW Dresden, 12 – 13 Mar 2008

- C. M. Papadakis, C. Darko, I. Botiz, G. Reiter, D. W. Breiby, J. W. Andreasen, D.-M. Smilgies, S. V. Roth
  Thin films of diblock copolymers having one crystalline block
  DPG Frühjahrstagung, Berlin, 28 Feb 2008

- C. M. Papadakis, K. Troll, A. M. B. Koumba, A. Laschewsky, P. Müller-Buschbaum
  Stimuli-sensitive micellar hydrogels from amphiphilic triblock copolymers
  19th Polymer Networks Group Meeting, Larnaca, Cyprus 23 Jun 2008

- C. M. Papadakis, A. Jain, A. Kulkarni, K. Troll, W. Wang, A. M. Bivigou Koumba, M. Sharp, P. Busch, V. Pipich, A. Laschewsky, P. Müller-Buschbaum
  Micellar solutions and hydrogels from temperature-responsive, amphiphilic block copolymers
  Deutsche Neutronenstreutagung 2008, Garching 15 Sep 2008

- J. Perlich, G. Kaune, M. Memesa, J. S. Gutmann, P. Müller-Buschbaum
  Structural characterization of nano-structured films from self-encapsulating inorganic-organic hybrid materials
  DFG SPP 1181/2 NANOMAT Arbeitskreistreffen Funktionsmaterialien: Mikrosysteme, Membranen, Katalyse, Bayreuth, 16 Jan 2008

- J. Perlich, V. Körstgens, E. Metwalli, L. Schulz, R. Georgii, P. Müller-Buschbaum
  Solvent content in thin spin-coated polymer films
  DPG Frühjahrstagung, Berlin, 28 Feb 2008

- J. Perlich, M. Memesa, J. S. Gutmann, P. Müller-Buschbaum
  Creating nano-structured films from self-encapsulated inorganic-organic hybrid materials
  DPG Frühjahrstagung, Berlin, February 2008

- J. Perlich, G. Kaune, M. Memesa, J. S. Gutmann, P. Müller-Buschbaum
  Structural characterization of nano-structured inorganic-organic hybrid materials for photovoltaic applications
  Tagung ‘Polymerwerkstoffe P200 P2008’, Halle, September 2008

- W. Petry
  Neutronen für Wissenschaft, Industrie und Medizin
  Institutskolloquium Lehrstuhl für Nukleartechnik RWTH Aachen, 15 Jan 2008

- W. Petry
  Neutrons for materials science and Phonons at martensitic phase transitions
  Institutskolloquium MPI für Eisenforschung, Düsseldorf, 17 Jan 2008

- W. Petry
  Neutron Source Heinz Maier-Leibnitz (FRM II)
  Meeting on Investigating Formation of Neutron Research Reactor Coalition, IAEA, Vienna, 11 – 13 Feb 2008

- W. Petry
  Forschung an Großgeräten am Beispiel von Neutronenquellen
  Edgar-Lüscher Lehrerfortbildung in Zwiesel, 4 Apr 2008

- W. Petry
  Neutronen bringen Licht ins Dunkel
  Freitagsvortrag des Heidelberger Life-Science-Lab am DKFZ, Heidelberg, 25 Apr 2008

- W. Petry
  Neutrons are beautiful
  Status Meeting, MaMaSELF at Rigi Kulm, Switzerland, 6 – 9 May 2008

- W. Petry
  Neutronen bringen Licht ins Dunkel
  Institutskolloquium der Fakultät für Physik der Universität Halle Wittenberg, 5 Jun 2008

- W. Petry
  Erfolgreiche Forschung mit Neutronen - aus der Arbeit der Forschungsneutronenquelle Heinz Maier-Leibnitz (FRM II)
  Vortrag im Presseclub München, 26 Jun 2008

- W. Petry
  The Neutron Source Heinz Maier-Leibnitz
  Idaho National Lab, Idaho Falls, USA, 3 Jul 2008

- W. Petry
  50 years after - the Mössbauer effect today and in the future
  Physik-Department der TU München, Garching, 9 Sep 2008

- W. Petry
  Atomkraft - ein Streit ohne Ende
  Teilnahme an der Sendung ”Redezeit” im NDR, 11 Nov 2008

- J. Repper, M. Hofmann, C. Krempaszky, R. Wimpory
  Micro Strain Accumulation in Multiphase Superalloys
  ICRS8, Denver, Co, USA, 6 – 8 Aug 2008

- J. Repper, M. Hofmann, C. Krempaszky, R. Wimpory
  Micro Strain Accumulation in Multiphase Superalloys
  MSE, Nürnberg, 1 – 4 Sep 2008

- J. Repper, M. Hofmann, C. Krempaszky, T. Keller
  Investigations of lattice spacing via neutron Larmor diffraction on IN718
  JCNS Workshop, Bernried, 15 – 17 Oct 2008

- A. Röhrmoser, W. Petry, P. Boulcourt, A. Chabre, S. Dubois, P. Lemoine, Ch. Jarousse, J.L. Falgoux, S. van den Berghe, A. Leenaers
  UMo full plate size irradiation experiment IRIS - TUM - a progress report
  RRFM 2008, Hamburg, Germany, 2 – 5 Mar 2008

- B. Sandow, D. Brossell, O. Bleibaum, W. Schirmacher
  Effect of the magnetic field on the Coulomb gap
  Frühjahrstagung der DPG, Berlin, 26 Mar 2008

- W. Schirmacher
  The boson peak: Anomalous vibrational properties of disordered solids
  Univ. Konstanz 21 Jan 2008

- W. Schirmacher
  Vibrational excitations in systems with correlated disorder
  XI. International Workshop on Complex Systems, Andalo, Italy, 17 Mar 2008

- W. Schirmacher
  Anomale Schwingungseigenschaften ungeordneter Festkörper
  Universität Karlsruhe, 23 Jun 2008
- W. Schirmacher
  Theorie einfacher Flüssigkeiten
  DLR Köln, 11 Mar 2008
- W. Schirmacher
  Anomalous vibrational properties of disordered solids
  Univ. Univ. "La Sapienza", Rom, 19 Sep 2008
- B. Schmid, W. Schirmacher
  Raman scattering in glasses and the boson peak
  Frühjahrstagung der DPG, Berlin, 26 Mar 2008
- T. Unruh, S. Busch, C. Smuda *Dynamics of Phospholipids in the Stabilizer Layer of Dispersed Nanoparticles Investigated by Quasielastic Neutron Spectroscopy*
  DPG Frühjahrstagung, Berlin, 25 – 29 Feb 2008
- T. Unruh
  From Alkanes to Membranes: Research at The Neutron Source Heinz Maier-Leibnitz (FRM II)
  Invited talk at the 38th Danish Crystallography and DanScatt annual meeting, University of Aarhus, 29 – 30 May 2008
- T. Unruh, C. Smuda, S. Busch, G. Gemmecker
  Self-Diffusion in Molecular Liquids: Medium Chain n-Alkanes and Coenzyme Q_{10} *studied by QENS*
  Deutsche Neutronenstreutagung 2008, Garching, 15 – 17 Sep 2008
- T. Unruh, C. Smuda, S. Busch
  Self-Diffusion in Molecular Liquids as seen by Quasielastic Neutron Scattering
  Invited seminar talk, Deutsches Zentrum für Luft- und Raumfahrt (DLR), Institut für Materialphysik im Weltraum, 04 Nov 2008
- T. Unruh, S. Busch, C. Smuda, L.C. Pardo
  Structure and Picosecond-Dynamics of Phospholipids in Colloidal Dispersions
  Invited seminar talk, LMU, CeNS: Lunch Seminar Soft Matter and Biophysics, 11 Nov 2008
- W. Wang, P. Müller-Buschbaum, K. Troll, A. Kulkarni, C. M. Papadakis, A. M. Bivigou Koumba, A. Laschewsky
  Temperature dependent swelling behavior of PNIPAM based block copolymer thin films
  DPG Frühjahrstagung, Berlin, 25 – 29 Feb 2008
- J. Wiedersich, S. Köhler, J. Friedrich, A. Skerra
  Thermodynamics of proteins: pressure and temperature denaturation curves
  DPG Frühjahrstagung, Berlin, 29 Feb 2008
- F. Yang, A. Meyer, T. Unruh, J. Kaplonski
  In-situ study of dynamics in hydrous silicate melts with quasielastic neutron scattering
  DPG Frühjahrstagung, Berlin, 25 – 29 Feb 2008

- F. Yang, A. Meyer, T. Unruh, K.-U. Hess
  Dynamics in hydrous silicates studied by high temperature high pressure quasielastic neutron scattering
  AGU Fall Meeting, San Francisco 15 – 19 Dec 2008

9.3 Posters

- M. M. Abul Kashem, G. Kaune, A. Diethert, W. Wang, K. Schlage, S. Couet, R. Röhlsberger, S. V. Roth, P. Müller-Buschbaum
  Structure formation upon sputtering of iron in diblock copolymer film with and without maghemite nanoparticles - an in situ GISAXS study
  IPF Colloquium, Dresden, 12 – 13 Nov 2008

- M. M. Abul Kashem, G. Kaune, A. Diethert, W. Wang, K. Schlage, S. Couet, R. Röhlsberger, S. V. Roth, P. Müller-Buschbaum
  Structure formation upon sputtering of iron in diblock copolymer film with and without maghemite nanoparticles - an in-situ GISAXS study
  DPG Frühjahrstagung, Berlin, 25 – 29 Feb 2008

- D. F. Anagnostopoulos, P. Patsalas, E. Skuras, C. Stanley, G. L. Borchert, R. Valicu, A. R. Wildes
  X-ray and Neutron reflectivity studies of self-assembled InAs quantum dot stacks on GaAs(100)
  Nanosciences & Nanotechnologies NN08, Thessaloniki, Greece, 14 – 16 Jul 2008

- S. Busch, C. Smuda, T. Unruh
  Investigations on the Structure and Dynamics of DMPC-Monolayers used as Stabilizers in Colloidal Dispersions
  DPG Frühjahrstagung, Berlin, 25 – 29 Feb 2008

- S. Busch, C. Smuda, L. C. Pardo Soto, S. Kurmulis, T. Unruh
  Dynamics of Phospholipids used as Stabilizers in Colloidal Dispersions studied by QENS
  Deutsche Neutronenstreutagung, Garching, 15 – 17 Sep 2008

- S. Busch, J. Wuttke, H. Scheer, M.-S. Appavou, and W. Doster
  Dynamical Transition of Protein Hydration Water: Fragile or Strong?
  Neutron Scattering Workshop on Biomolecular Dynamics and Protein-Water Interactions, Feldafing, 24 – 26 Sep 2008

- C. Darko, I. Botiz, G. Reiter, D. W. Breiby, J. W. Andreasen, D.-M. Smilgies, S. V. Roth, C. M. Papadakis
  Thin films of diblock copolymers with one crystalline block
  HASYLAB User Meeting, Hamburg, 25 Jan 2008

- C. Darko, K. Troll, Z. Di, D.-M. Smilgies, A. Timmann, S. Förster, C. M. Papadakis
  Break-Away Crystallization in Thin Films of PI-b-PEO Diblock Copolymers
  HASYLAB User Meeting, Hamburg, 25 Jan 2008

- C. Darko, K. Troll, Z. Di, D.-M. Smilgies, A. Timmann, S. Förster, C. M. Papadakis
  Break-Away Crystallization in Thin Films of PI-b-PEO Diblock Copolymers
  CHESS User Meeting, Ithaca NY, USA, 10 – 11 Jun 2008

- C. Darko, I. Botiz, G. Reiter, D. W. Breiby, J. W. Andreasen, D.-M. Smilgies, S. V. Roth, C. M. Papadakis
  Thin Films of Crystalline Diblock Copolymers
  CHESS User Meeting, Ithaca NY, USA, 10 –11 Jun 2008

- Z. Di, C. Darko, D. Posselt, D.-M. Smilgies, A. Timmann, M. A. Singh, C. M. Papadakis
  The Effect of Heat Treatment on the Lamellar Structure in Diblock Copolymer Films
  HASYLAB User Meeting, Hamburg, 25 Jan 2008

- Z. Di, C. Darko, A. Timmann, D.-M. Smilgies, D. Posselt, C. M. Papadakis
  Structure of thin block copolymer films and their changes in solvent vapor atmosphere
  HASYLAB User Meeting, Hamburg, 25 Jan 2008

- Z. Di, C. M. Papadakis, C. Darko, D. Posselt, D.-M. Smilgies
  Structural changes in thin block copolymer films during vapor treatment
  DPG Frühjahrstagung, Berlin, 26 Feb 2008

- Z. Di, C. Darko, A. Timmann, D.-M. Smilgies, D. Posselt, C. M. Papadakis
  Structures of thin block copolymer films and their changes in solvent vapor atmosphere
  CHESS User Meeting, 10 – 11 Jun 2008

- Z. Di, C. M. Papadakis, C. Darko, D. Posselt, D.-M. Smilgies
  Structures of thin block copolymer films and their changes in solvent vapor atmosphere
  1st Joint Nano Workshop, Garching, 10 Jun 2008

- Z. Di, L. Willner, R. Kampmann, M. Haese-Seiller, C. M. Papadakis
  Buried structures in thin block cpolymer films - time-of-flight neutron reflectometry
  Deutsche Neutronenstreutagung, Garching 15 Sep 2008

- A. Diethert, E. Metwalli, J. Perlich, W. Wang, R. Gehrke, S. V. Roth, A. Timmann, P. Müller-Buschbaum
  GISAXS study of surface enrichment layers in statistical copolymer films
  HASYLAB User Meeting, Hamburg, 25 Jan 2008

- A. Diethert, E. Metwalli, P. Müller-Buschbaum
  Surface enrichment in statistical copolymer films
  DPG Frühjahrstagung, Berlin, 25 – 29 Feb 2008

- A. Golosova, R. Jordan, C. M. Papadakis
  Functional Nanocomposites by Directed Assembly of Carbon Nanotubes in Block Copolymer Matrix
  1st Joint Nano Workshop, Garching, 10 Jun 2008

- A. Golosova, R. Jordan, C. M. Papadakis
  Functional Nanocomposites by Directed Assembly of Carbon Nanotubes in Block Copolymer Matrix
  IGSSE Forum 2008, Raitenhaslach, 27 –28 Jun 2008

- R. Ivanova, T. Bonné, K. Mortensen, P. K. Pranzas, T. Komenda, K. Lüdtke, R. Jordan, C. M. Papadakis
  Self-assembly and multi-compartment micellar hydrogel formation of amphiphilic di- and triblock copolymers containing fluorophilic blocks
  DPG Frühjahrstagung, Berlin, 27 Feb 2008

- R. Ivanova, T.B. Bonné, T. Komenda, K. Lüdtke, P. Štěpánek, R. Jordan, C. M. Papadakis
  Micellar Multicompartment Hydrogels from Poly¡(2-Oxazoline)s Containing Fluorophilic, Hydrophylic and Lipophylic Blocks
  Polymer Colloids, Prag, 21 Jul 2008

- D. Jehnichen, D. Pospiech, S. Ptacek, K. Eckstein, P. Friedel, A. Janke, A. Korwitz, C. M. Papadakis, A. Timmann, S. S. Funari
  Investigation of nanostructured PPMA-PMMA diblock copolymer films
  HASYLAB User Meeting, Hamburg, 25 Jan 2008

- D. Jehnichen, D. Pospiech, S. Ptacek, K. Eckstein, P. Friedel, A. Janke, C.M. Papadakis
  Nanophase-separated poly(pentylmethacrylate-b-methylmethacrylate) diblock copolymers: Structure investigations using X-ray scattering methods, EPDIC-11
  European Powder Diffraction Conference, Warszaw, Poland, 18 – 22 Sep 2008

- G. Kaune, W. Wang, E. Metwalli, M. Ruderer, K. Schlage, S. Couet, R. Röhlsberger, S. V. Roth, P. Müller-Buschbaum
  Structure of gold films as contact material in organic photovoltaic devices
  HASYLAB User Meeting, Hamburg, 25 Januar 2008

- G. Kaune, W. Wang, E. Metwalli, M. Ruderer, K. Schlage, S. Couet, R. Röhlsberger, S. V. Roth, P. Müller-Buschbaum
  Structure of gold films as contact material in organic photovoltaic devices
  DPG Frühjahrstagung, Berlin, 25 – 29 Feb 2008

- G. Kaune, E. Metwalli, U. van Bürck, J. -F. Moulin, P. Müller-Buschbaum
  GISANS study of layered TiO2:polymer films for photovoltaic applications
  Deutsche Neutronenstreutagung, Garching, 15 – 17 Sep 2008

- A. Kulkarni, K. Troll, W. Wang, S. S. Funari, A. M. Bivigou Koumba, A. Laschewsky, P. Müller-Buschbaum, C. M. Papadakis
  Stimuli-sensitive self-organized polymer micelles
  HASYLAB User Meeting, Hamburg, 25 Jan 2008

- A. Kulkarni, H. Greve, U. Schürmann, V. Zaporojtchenko, E. Quandt, F. Faupel
  Soft magnetic nanocomposite film for high frequency applications
  DPG Frühjahrstagung, Berlin, 27 Feb 2008

- A. Kulkarni, A. Jain, W. Wang, A. M. Bivigou Koumba, P. Busch, M. Sharp, A. Laschewsky, P. Müller-Buschbaum, C. M. Papadakis
  Responsive Hydrogels from Amphiphilic Block Copolymers with a Responsive Hydrophilic BLock
  Polymer Colloids, Prag, 21 Jul 2008

- R. Meier, M. Ruderer, J. Perlich, G. Kaune, R. Georgji, P. Müller-Buschbaum
  Neutron Reflectivity Measurements on Conducting Polymer Films
  Deutsche Neutronenstreutagung 2008, München, 15 – 17 Sep 2008

- A. Meier-Koll, J. Wiedersich, P. Müller-Buschbaum, W. Schirmacher
  Brillouin spectrsocopy of disordered systems
  DPG Frühjahrstagung, Berlin, 25 – 29 Feb 2008

- A. Meier-Koll, A. Golosova, A. Jain, A.M. Bivigou Koumba, A. Laschewsky, P. Busch, V. Pipich, J. Wiedersich, P. Müller-Buschbaum, C.M. Papadakis

Deswelling kinetics of micellar solutions and hydrogels from temperature-sensitive amphiphilic block copolymers
Deutsche Neutronenstreutagung, München, 14 – 17 Sep 2008

- M. Memesa, M. Lechmann, Y. Cheng, J. Perlich, P. Müller-Buschbaum, J. S. Gutmann
Structured TiO2 nanoparticle preparation for solar cells
International Symposium towards organic photovoltaics ORGANETPV, Linz, Februar 2008

- E. Metwalli, S. Couet, K. Schlage, R. Röhlsberger, V. Körstgens, M. Ruderer, W. Wang, G. Kaune, S.V. Roth, P. Müller-Buschbaum
In situ GISAXS study of gold sputtering onto a polymer template
HASYLAB User Meeting, Hamburg, 25 Jan 2008

- E. Metwalli, J.-F. Moulin, P. Müller-Buschbaum
Structural investigation on thin block copolymer films using time-of-flight grazing incidence small-angle neutron scattering
Int. conf. surface X-ray and neutron scattering, Paris, 2 – 5 Jul 2008

- E. Metwalli, M.-S. Appavou, R. Gebhardt, J.-F. Moulin, V. Körstgens, R. Cubitt, A. Tolkach, U. Kulozik, W. Doster, P. Müller-Buschbaum
Hydration behavior of casein micelles in thin film: GISANS study
Deutsche Neutronenstreutagung, Garching, 14 – 17 Sep 2008

- E. Metwalli, J.-F. Moulin, U. van Brueck, G. Kaune, M. Ruderer, P. Müller-Buschbaum
Probing polymer interfaces using time-of-flight grazing incidence small-angle neutron scattering
Deutsche Neutronenstreutagung, Garching, 14 – 17 Sep 2008

- E. Metwalli, M.-S. Appavou, R. Gebhardt, J.-F. Moulin, V. Körstgens, R. Cubitt, A. Tolkach, U. Kulozik, W. Doster, P. Müller-Buschbaum
Water hydration of casein micelles in thin films: GISANS study
Biomolecular Dynamics Protein-Water Interaction -Neutron Scattering Workshop München-Feldafing, 24 – 26 Sep 2008

- P. Müller-Buschbaum, L. Schulz, E. Metwalli, J.-F. Moulin, R. Cubitt
Lateral structures of buried interfaces in tri-block copolymer films
Deutschen Neutronenstreutagung, Garching, 14 – 17 Sept 2008

- C. M. Papadakis, C. Darko, D. Posselt, D.-M. Smilgies, A. Timmann, M. A. Singh
The effect of heat treatment on the internal structure of thin, lamellar diblock copolymer films
CHESS User Meeting, Ithaca NY, USA, 10 – 11 Jun 2008

- C. M. Papadakis, R. Ivanova, T. B. Bonné, T. Komenda, K. Lütke, K. Mortensen, P. K. Pranzas, R. Jordan
Self-assembly and multi-compartment micellar hydrogel formation of amphiphilic di- and triblock copolymers containing fluorophilic blocks
Deutsche Neutronenstreutagung, Garching 15 Sep 2008

- J. Perlich, M. Memesa, Y. Cheng, J. S. Gutmann, S.V. Roth, P. Müller-Buschbaum
μGISAXS investigation of the morphological modification of TiO_2 nanocomposite films
HASYLAB User Meeting, Hamburg, 25 Jan 2008

- J. Perlich, G. Kaune, M. Ruderer, R. Meier, M. Memesa, J. S. Gutmann, P. Müller-Buschbaum

Structural investigation of thin polymer nanocomposite and blend films for photovoltaic applications
International Symposium towards organic photovoltaics ORGANETPV, Linz, Februar 2008

- J. Perlich, V. Körstgens, E. Metwalli, L. Schulz, R. Georgii, P. Müller-Buschbaum
  Solvent content in thin spin-coated polystyrene homopolymer films
  Deutsche Neutronenstreutagung, Garching, 15 – 17 Sep 2008

- J. Repper, M. Hofmann, C. Krempaszky, T. Keller, E. Werner, W. Petry
  The new neutron Larmor diffraction method to determine absolute values of lattice spacing
  ICRS8, Denver, Co, USA, 6 - 8 Aug 2008

- J. Repper, M. Hofmann, C. Krempaszky, T. Keller, E. Werner, W. Petry
  The new neutron Larmor diffraction method to determine absolute values of lattice spacing
  Deutsche Neutronenstreutagung, Garching, 15 - 17 Sep 2008

- J. Rebelo Kornmeier, M. Hofmann, U. Garbe, A. Ostermann, C. Randau, J. Repper, W. Tekouo, G.A. Seidl, R.C. Wimpory, R. Schneider, H.-G. Brokmeier
  New Developments at Materials Science Diffractometer STRESS-SPEC at FRM II
  ICRS8, Denver, Co, USA, 6 - 8 Aug 2008

- B. Sandow, D. Brossell, W. Schirmacher
  Different transport mechanisms across semiconductor junctions
  DPG Frühjahrstagung, Berlin, 28 Feb 2008

- W. Schirmacher, L. Schulz, S. Vallopilly, P. Böni, W. Petry, P. Müller-Buschbaum
  Magnetic properties of nanoparticles imbedded in a diblock-copolymer matrix
  Int. workshop on topics in solid state science, Klosters, Switzerland, 20 Feb 2008

- W. Schirmacher, B. Schmid, C. Tomaras, G. Viliani, G. Baldi, G. Ruocco, T. Scopigno
  Vibrational excitations in systems with correlated disorder
  DPG Frühjahrstagung, Berlin, 28 Feb 2008

- C. Smuda, G. Gemmecker, S. Busch, T. Unruh
  Diffusion of medium-chain molecules studied by QENS and PFG-NMR
  DPG Frühjahrstagung, Berlin, 25 – 29 Feb 2008

- C. Smuda, S. Busch, G. Gemmecker, T. Unruh
  Dynamics of coenzyme Q_{10} *inside nanodroplets studied by QENS*
  22nd Conference of the European Colloid and Interface Society, Cracow, Poland, 31 Aug – 5 Sep 2008

- C. Smuda, S. Busch, B. Wagner, T. Unruh
  Methyl group dynamics in glassy, polycrystalline, and liquid coenzyme Q_{10} *studied by QENS*
  Deutsche Neutronenstreutagung, Garching, 15 – 17 Sep 2008

- K. Troll, A. Kulkarni, C. M. Papdakis, W. Wang, P. Müller-Buschbaum, A. M. Bivigou Koumba, A. Laschewsky
  Stimuli- sensitive micelles from amphiphilic diblock copolymers
  DPG Frühjahrstagung, Berlin, 27 Feb 2008

- R. Valicu, R. Iannuci, G. Borchert
  Development of higher m supermirors
  Deutsche Neutronenstreutagung, München, 14 – 17 Sep 2008

- R. Valicu, P. Boni
  Monte Carlo simulations for focussing elliptical guides
  Deutsche Neutronenstreutagung, München, 14 – 17 Sep 2008

- W. Wang, K. Troll, G. Kaune, E. Metwalli, M. Ruderer, K. Skrabania, A. Laschewsky, S. V. Roth, C. M. Papadakis, P. Müller-Buschbaum
  Thin films of poly(N-isopropylacrylamide) end-capped with n-butyltrithiocarbonate
  HASYLAB User Meeting, Hamburg, 24 Jan 2008

- W. Wang, J. -F. Moulin, J. Perlich, M. M. Abul Kashum, S. V. Roth, A. Laschewsky, C. M. Papadakis, P. Müller-Buschbaum
  Response of thin hydrogel films to water flow investigated with in-situ grazing incidence small-angle x-ray scattering
  The 10th International Conference on Surface X-ray and Neutron Scattering, Paris, 2 – 5 Jul 2008

- W. Wang, E. Metwalli, J. Perlich, K. Troll, C. M. Papadakis, R. Cubitt, P. Müeller-Buschbaum
  Water storage in novel undeformable hydrogel thin films as probed with in-situ neutron reflectivity
  Deutsche Neutronenstreutagung, Garching 16 Sep 2008

- E. Wischerhoff, A. Bivigou Koumba, A. Laschewsky, J.-F. Lutz, A. Lankenau, K. Uhlig, C.M. Papadakis, P. Müller-Buschbaum
  Smart Polymeric Hydrogels in Bulk Phase and in Thin Films
  Freiburger Makromolekulares Kolloquium, Freiburg 26 – 28 Feb 2009

- F. Yang, A. Meyer, T. Unruh
  Dynamics in hydrous silicates studied by high temperature high pressure quasielastic neutron scattering
  Deutsche Neutronenstreutagung, Garching, 15 – 17 Sep 2008

9.4 Invited talks at E13

- Wolfgang Brütting, Universität Augsburg
  Organic semiconductor blends: charge transport electric structure and implications for device applications
  22.01.2008

- Prof. Thomas Bein, Chemiedepartment der LMU
  Tuning functionality and morphology of periodic nanoporous materials
  29.01.2008

- Prof. Dr. Lukas Schmidt-Mende, LMU
  Nanostructures for photovoltaic applications
  05.03.2008

- Monika Iwanowska, MaMaSelf und Kyoto University
  SrCoO (2.5+x) thin films - characterization of the structures and magnetic properties
  14.05.2008

- Prof. Robert Magerle, Chemische Physik, TU Chemnitz
  Mesoskalige Dynamik in Blockcopolymerfilmen
  27.05.2008
- Eicke Tilo Hoppe, Fraunhofer-Institut Würzburg
  Nanostrukturierung mit PS-b-PEO
  28.05.2008
- Prof. Dr. Alfons Schulte, University of Central Florida
  Light and neutron spectroscopy of glasses for Raman gain applications
  26.06.2008
- Dr. Detlef-M. Smilgies, Cornell High-Energy Synchrotron Source, Ithaca NY
  Structure and Kinetics of Organic Thin Films
  07.07.2008
- Evalyn Alayon Mae, MaMaSelf und ETH Zürich
  Unveiling the Active Sites of Supported Platinum Catalysts for Carbon Monoxide Oxidation
  18.07.2008
- Joseph Adelsberger, Universität Regensburg
  Untersuchung elektrolytischer Lösungen an flüssig/fest Grenzflächen mit Hilfe der Monte-Carlo-Methode
  23.07.2008
- Dr. Maria Mayorova, IFF, FZ Jülich
  Dynamics of glass-forming liquid in soft and hard confinements
  09.10.2008
- Qi Zhong, Universität Kiel
  Analysis of pore formation on (100) n-type Ge with and without back side illumination using FFT impedance spectroscopy
  20.10.2008
- Fabio Balloni, Technische Universität Darmstadt
  SAXS to estimate aggregation of polymers
  20.10.2008
- Katharina Rolfs, HMI Berlin
  Co-Doping: Tuning Ni-Mn-Ga for Acuator Application
  21.10.2008
- Martha Brennich, LMU
  Infrared spectroscopy on the aggregation of hairpin model peptides
  29.10.2008
- Ning-Yu Wu, National Tsing-Hua University (NTHU), Taiwan
  Visualisation of carbon nanotubes
  05.12.2008
- Hackeem Owusu, Universität Kiel
  Porous bi-layers for solar application
  08.12.2008

- Prof. Martin Müller, GKSS Geesthacht
  Structure and dynamics of biological materials investigated using scattering techniques
  09.12.2008

- Dr. Melissa Sharp, GKSS Geesthacht
  Using SANS to study the solubilisation of modul adjuvants by Pluronic block copolymers
  16.12.2008

9.5 Funding

- **Deutsche Forschungsgemeinschaft:**

- Im Rahmen des DFG priority program SPP 1164:
  Non-equilibrium flow at gradient surface: multi-component fluids
  Förderkennzeichen: MU 1487/2-2
  Leiter: Prof. Peter Müller-Buschbaum

- Im Rahmen des DFG priority program SPP 1164:
  Non-equilibrium flow at gradient surfaces: Fluid kinetics of droplets and particle motion
  Förderkennezeichen: MU 1487/2-3
  Leiter: Prof. Peter Müller-Buschbaum

- *Quellverhalten von dünnen Polymerfilmen: Struktur, Kinetik und Dynamik*
  Förderkennzeichen: MU 1487/4-2
  Leiter: Prof. Peter Müller-Buschbaum

- Im Rahmen des DFG Schwerpunktprogramm SPP 1181:
  Nanostrukturierte Filme aus selbstkapselnden anorganisch-organischen Hybridmaterialien
  Förderkennzeichen: MU 1487/5-1
  Leiter: Prof. Peter Müller-Buschbaum

- Im Rahmen des DFG Schwerpunktprogramm SPP 1181:
  Hierarchisch strukturierte Filme aus selbstkapselnden anorganisch-organischen Hybridmaterialien
  Förderkennzeichen: MU 1487/5-2
  Leiter: Prof. Peter Müller-Buschbaum

- *Einfluss von Grenzflächeneffekten auf die Adhäsion weicher Polymere*
  Förderkennezeichen: MU 1487/6-1
  Leiter: Prof. Peter Müller-Buschbaum

- Im Rahmen des DFG priority program SPP 1259:
  Struktur und Kinetik stimuli-rexponsiver, dünner Hydrogelfilme aus amphiphilen Blockcopolymern
  Förderkennzeichen: MU 1487/8-1, Folgeprojekt MU 1487/8-2
  Leiter: Prof. Peter Müller-Buschbaum

- *Magnetic, magnetoelastic and dynamical properties of martensitic Heusler alloys- Teilprojekt Neuhaus*
  Förderkennzeichen: NE 1405/1-1
  Leiter: Dr. Jürgen Neuhaus

- *Änderung von Mikrostruktur und Form fester Werkstoffe durch äußere Magnetfelder*
  Förderkennzeichen: NE 1405/1-2
  Leiter: Dr. Jürgen Neuhaus

- *Steigerung der Berechnungsgenauigkeit der Eigenspannungsverteilung im Aluminiumformguss mittels Neutronendiffraktometrie*
  Förderkennzeichen: PE 580/6-2
  Leiter: Dr. Michael Hofmann

- *Rolle der Mikrospannungen bei der Eigenspannungsanalyse mittels Neutronenbeugung in mehrphasigen Hochleistungslegierungen*
  Förderkennzeichen: PE 580/7-1
  Leiter: Prof. Winfried Petry

- *Inelastische Neutronenstreuung bei hohen Temperaturen und Drücken zur Aufklärung der Lösungs- und Transportmechanismen von Wasser in wasserhaltigen Silikatschmelzen*
  Förderkennzeichen: PE 580/8-3
  Leiter: Prof. Winfried Petry

- *Untersuchung des Einflusses der atomaren Dynamik auf Materietransport, Segregation und Erstarrung mehrkomponentiger Schmelzen*
  Förderkennzeichen: ME 1958/2-2, Folgeprojekt ME 1958/2-3
  Leiter: Prof. Winfried Petry

- *Inelastische Neutronenstreuung bei hohen Temperaturen und Drücken zur Aufklärung der Lösungs- und Transportmechanismen von Wasser in wasserhaltigen Silikatschmelzen*
  Förderkennzeichen: ME 1958/8-2
  Leiter: Prof. Winfried Petry

- Im Rahmen des SFB 533:
  Lichtinduzierte Dynamik von Biopolymeren
  Teilprojekt B11 "Proteindynamik unter Hochdruck"
  Leiter: Dr. Wolfgang Doster

- *Thin Films of Crystalline Diblock Copolymers: Crystalline and Mesoscopic Structures and their Macroscopic Alignment*
  Förderkennzeichen: PA 771/3-1, Folgeprojekt PA 771/3-2
  Leiter: Prof. Christine Papadakis

- In the DFG Priority Program: SPP 1259 'Intelligente Hydrogele':
  Struktur und Kinetik stimuli-responsiver, dünner Hydrogelfilme aus amphiphilen Blockcopolymeren
  Förderkennzeichen: PA 771/4-1, Folgeprojekt PA 771/4-2
  Leiter: Prof. Christine Papadakis

- *Multicompartment systems based on poly (2-oxazoline)s*
  Förderkennzeichen: PA 771/6-2
  Leiter: Prof. Christine Papadakis

- *Lokale Viskosität und Dichte in der Grenzphase von Polymeren an einer festen Grenzfläche - Fluoreszenz-Korrelationsspektroskopie und Neutronenreflektrometrie*
  Förderkennzeichen: PA 771/7-1

Leiter: Prof. Christine Papadakis

- **Bundesministerium für Bildung und Forschung:**

- *Entwicklung und Aufbau von muSISAXS am muSAXS/WAXS Instrument am Synchroton PETRA III*
  Förderkennzeichen: 05KS7WO1
  Leiter: Prof. Peter Müller-Buschbaum

- **Others:**

- Im Rahmen des Internationalen Graduiertenkollegs:
  Material Science of Complex Interfaces
  Magnetic particles in supported polymer structures
  Leiter: Prof. Peter Müller-Buschbaum
- Im Rahmen des Internationalen Graduiertenkollegs:
  Material Science of Complex Interfaces
  Strukturelle Änderungen in nanostrukturierten Blockcopolymerfilmen - Zeitaufgelöste in-situ-Untersuchungen mit Röntgenkleinwinkelstreuung unter streifendem Einfall
  Leiter: Prof. Christine Papadakis
- *Copenhagen Munich Center of Soft, Nanostuctured Material (CMC-SNN)*
  Incentive Fund for Research Collaborations between Technische Universität München and the Danish Technical University
  Leiter: Prof. Christine Papadakis, PD Dr. Rainer Jordan (Department Chemie, Technische Universität München), Prof. Martin E. Vigild (Department of Chemical Engineering, Danish Technical University)
- *Crystalline, mesoscopic and long-range order in thin films of crystalline block copolymers*
  Incentive Fund for Research Collaborations between Technische Universität München and the Danish Technical University
  Leiter: Prof. Christine Papadakis, Dr. Jens Wenzel Andreasen (Risø National Laboratory, Danish Technical University)
- *Preparation and characterization of functional nanocomposites by directed assembly of modified carbon nanotubes in block copolymer matrices*
  Im Rahmen der International Graduate School of Science and Engineering (IGSSE)
  Leiter: Prof. Christine Papadakis, PD Dr. Rainer Jordan (Department Chemie, Technische Universität München)

10 The chair

10.1 Graduations

- **Accomplished diploma thesis**

  Kordelia Troll
  Thermoresponsive Mizellen aus amphiphilen Diblockcopolymeren

  Stefan Guldin
  Nanostructuring inorganic material by copolymer-assisted self-assembly

- **Accomplished master thesis**

  Abhinav Jain
  Responsive hydrogels from amphiphilic block copolymers

- **Accomplished bachelor thesis**

  Stephan Salzinger
  Floureszenzmarkierung schaltbarer Poly(2-oxazolin)e

- **Accomplished PhD thesis**

  Charles Darko
  Thin films of crystalline diblock copolymers: Crystallization under different confinements

10.2 Staff

Chair: Univ.-Prof. Dr. Winfried Petry

Head: Univ.-Prof. Dr. Peter Müller-Buschbaum

Fellows
Dr. Ezzeldin Metwalli Ali
PD Dr. Wolfgang Doster
Dr. Ana Gaspar
Dr. Rusha Ivanova
Dr. Volker Körstgens
Dr. Amit Kulkarni
Dr. Peter Link
Dr. Jürgen Neuhaus (FRM II)
Prof. Dr. Christine Papadakis
Prof. Dr. Walter Schirmacher
Dr. Tobias Unruh
Dr. Uwe van Bürck
Dr. Johannes Wiedersich

PhD students
Mottakin Abul Kashem
Joseph Adelsberger
Sebastian Busch
Charles Darko
Zhenyu Di

Alexander Diethert
Anastasia Golosova
Christian Hesse
Tilo Hoppe
Gunar Kaune
Tarik Mehaddene
Robert Meier
Andreas Meier-Koll
Jan Perlich
Julia Repper
Matthias Ruderer
Christoph Smuda
Sebastian Stüber
Weinan Wang
Fan Yang
Qi Zhong

Diploma students
Christoph Geissinger
Stefan Guldin
Oleksandr Khegai
Stefan Prams
Bernhard Schmid
Kordelia Troll

Master students
Mekonnen Besira
Abhinav Jain

Bachelor students
Stephan Salzinger

Students assistants
Christian Böttner
Isabell Franck
David Magerl
Martin Müller
Alexandra Münzer
Steven Nyabero
Gunther Reithmaier
Constantin Tomaras

Technical/administrative staff
Monika Antoniak
Philipp Bork
Petra Douglas
Reinhold Funer
Lukas Hein
Raffael Jahrstorfer

Josef Kaplonski
Dieter Müller
Jandal Ringe

10.3 Guests

- Dr. Mahmoud Al-Hussein, University of Jordan, Amman, Jordan
  Februar – August 2008
- Prof. Dr. Alfons Schulte, University of Central Florida
  26 June 2008
- Nora Kristen, Technische Universität Berlin
  04.-06.02.2008
- Dr. Detlef M. Smilgies, Cornell University, Ithaca NY, USA
  06.-12.07.2008
- Prof. Dorthe Posselt, Roskilde University, Dänemark
  11.-14.08.2008
- Nora Kristen, Technische Universität Berlin
  01.-05.12.2008